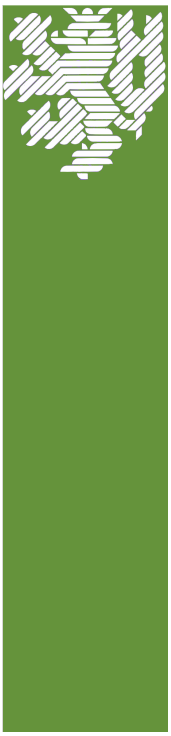

Analysis of Super-Preshowers at the Pierre Auger Observatory

Analyse von Super-Preshowern am Pierre Auger Observatorium

Master-Thesis zum Erlangen des Grades

Master of Science

Bergische Universität Wuppertal

Fakultät Mathematik und Naturwissenschaften

Fachgruppe Physik

vorgelegt von

Alex Kääpä

26.02.2016

Betreuender Professor: Prof. Dr. Karl-Heinz Kampert

Zweitkorrektor: Prof. Dr. Zoltán Fodor

Acknowledgements

There are many people who have greatly assisted me during my work on this thesis, to whom I owe my greatest gratitude. I would like to start with Professor *Karl-Heinz Kampert* and Professor *Zoltàn Fodor*, whom I thank for agreeing to be my supervisors for this thesis. Next, I want to thank *Raymond Stoneham*, *Alice Harding*, *Tanguy Pierog*, Professor Fodor and *Sandor D. Katz*, who have taken the time to respond to questions and give feedback on individual aspects of my research. I would also like to thank Professor Kampert for contacting the aforementioned people and for providing prospects for my future scientific career.

The *Auger* group at the *BUW* have provided helpful feedback in the weekly group meetings, for which I am very grateful. In addition, I have to thank *Julian Rautenberg* and *Tobias Winchen*, from whom I received valuable input for both my research and my writing. Many thanks go also to *Stepan Nassyr*, who has been of great assistance whenever I had issues with respect to programming.

I want to express my sincerest gratitude to *Piotr Homola* who accompanied me during my work on this thesis and who has proved to be indispensable for bringing it to its final form. His regular and helpful feedback, motivating persona and continuous endorsement have been of invaluable encouragement. I couldn't have hoped for a better assistant with this thesis.

I owe a lot to my parents *Pia* and *Olli* who have always given me moral support and pushed me forwards, particularly in the past year, and to my brother *Niko* for being the best of friends and helping me to take my mind off this work whenever it appeared overwhelming. Thank you for being part of my life.

Lastly, I want thank my partner *Lisa*, not only for proofreading this thesis. I cannot express the gratitude I feel for your patience, dependability, bounty and love. You have changed me and my life for the better.

Abstract

This thesis explores an alternative cosmic ray composition scenario with a significant fraction of photons that undergo a so-called *super-preshower* before entering into Earth's atmosphere. Super-preshowers are an analogous phenomenon to the already considered preshower, but contain different processes that might occur at altitudes at least an order of magnitude higher, possibly even much higher, depending on the process. Candidate processes, i.e. *photon splitting in the (geo-)magnetic field* and *pair production via interaction with solar photons* are analysed. The effect of super-preshowers initiated near Earth (i.e. around 10000 km a.s.l.) on air shower observables, such as longitudinal development and muon production, that are relevant for mass composition studies at the Pierre Auger Observatory, are investigated with the use of simulations with *Conex*. While interactions with solar photons are shown to be too rare to significantly contribute to a super-preshower, conclusions on photon splitting for the entire phase space of the photon energy and the strength of the (geo-)magnetic field could not be drawn due to a lack of convergence of the performed calculations with the available literature. Within the low-frequency limit, however, I found that photon splitting is a negligible process for a possible super-preshower, although its applicability to Auger conditions is dubious. Simulations show that photon initiated air showers undergoing super-preshowers can mimic hadronic showers in terms of energy deposit, but there are distinct differences with respect to muon production pertaining to the number of produced muons and the energy dependence of muon production. Such differences could be due to an underestimation of the photonuclear cross-section and an under-reconstruction of the primary energy for super-preshowers, as well as on unaccounted phenomena, like energy losses in radiation belts. Altogether, super-preshowers cannot be ruled out and are worthy of further, more detailed studies.

Zusammenfassung

Diese Thesis untersucht ein alternatives Kompositionsszenario kosmischer Strahlung mit einem signifikantem Anteil an Photonen, die vor Eintritt in die Erdatmosphäre einen sogenannten *Super-Preshower* auslösen. Super-Preshower sind ein zum bereits berücksichtigten Preshower analoges Phänomen, beinhalten jedoch andere Prozesse, die in mindestens zehnmal höheren Lagen stattfinden könnten, möglicherweise noch wesentlich höher, abhängig vom Prozess. Mögliche Prozesse, nämlich *Photon Splitting im (Erd-)Magnetfeld* und *Paarproduktion durch Wechselwirkung mit solaren Photonen* werden analysiert. Der Einfluss von Super-Preshowern auf Luftschauerobservablen, wie Energieverlust und Myonproduktion, die relevant für Kompositionsstudien am the Pierre Auger Observatorium sind, werden anhand Simulationen mit *Conex* erforscht. Obwohl gezeigt wird, dass Wechselwirkungen mit solaren Photonen zu selten auftreten, um maßgeblich zu einem Super-Preshower beizutragen, ist es, aufgrund mangelnder Übereinstimmung zwischen Berechnungen und vorhanderener Literatur, nicht möglich, Aussagen über Photon Splitting für den gesamten Phasenraum von Photonenergie und (Erd-)Magnetfeldstärke zu treffen. Im Niederfrequenz-Limes stellt sich heraus, dass Photon Splitting als möglicher Super-Preshower-Prozess vernachlässigbar ist, obwohl die Gültigkeit dieses Limes für Auger-Bedingungen fragwürdig ist. Die Simulationen zeigten, dass photoninduzierte Luftschauer bzgl. des Energieverlusts hadronische Luftschauer nachahmen können, jedoch deutliche Unterschiede in der Myonproduktion aufweisen in Bezug auf die Myonenzahl und die Energieabhängigkeit der Myonenproduktion. Diese Unterschiede könnten jedoch auf eine Unterschätzung des photonuklearen Wirkungsquerschnitts oder der Energierekonstruktion von Super-Preshowern, aber auch auf bisher unberücksichtigte Prozesse, wie der Energieverlust im Strahlungsgürtel, zurückzuführen sein. Insgesamt können Super-Preshower nicht ausgeschlossen werden und sind weiterer, detaillierter Untersuchungen würdig.

Contents

Chapter 1

Introduction

Over a century after their discovery, there are still many mysteries surrounding cosmic rays. While their flux and composition over vast energy ranges have been probed, with which many of their properties could be unravelled, the origin, propagation processes and composition of cosmic rays, in particular at highest energies (so-called ultra-high energy cosmic rays, above 10^{18} eV) is still largely not known, mainly due strong limitations by the statistics at these energies. The measurement of such cosmic rays is essential for shedding light on this conundrum as their deflection in galactic and inter-galactic magnetic fields is weaker with increasing energy. They are so rare, however, that they can only be measured with ground-based detectors, i.e. only indirectly via the measurement of particles cascades, called extensive air showers, that cosmic rays initiate as they enter Earth's atmosphere. Measuring the energy and nature with sufficient statistics requires a sophisticated detection method and large detector areas. The Pierre Auger Observatory, using a hybrid detection method, i.e. a surface detector array in concordance with optical telescopes, spanning an area of 3000 km^2, allows the study of spectral, anisotropy and composition properties of cosmic rays at highest energies with unprecedented precision (see section 2.1).

Ultra-high energy photons, once observed, are of particular value in this regard. On the one hand, they are especially useful for identifying the (high-energy) sources of cosmic rays as their arrival direction points directly to their origins due to a lack of deflection in magnetic fields. On the other hand, the fraction of photons in the cosmic ray flux gives information on

different classes of production mechanisms of cosmic rays. High photon fractions are indicatory of exotic or top-down production models, which could have far-reaching consequences not only for cosmic ray, but also for fundamental physics, such as Lorentz invariance and unobserved physics, including dark matter and dark energy (see sections 2.2).

Identifying photon showers at highest energies is not trivial, however, as interactions with the geomagnetic field that produce so-called preshowers before entering the atmosphere make the subsequent air shower increasingly resemble those initiated by heavy hadronic primaries; this effect increases with energy and the strength of the transverse component of the magnetic field (see section 2.2.1).

Latest results from the the Pierre Auger Observatory, that take all known processes into account, do not show any evidence of photons, neither from point sources, nor of diffuse origin, given current model predictions; from these findings, a predominantly hadronic composition is concluded and exotic acceleration mechanisms strongly constrained (see sections 2.2 and 2.3.1). Mass composition measurements show a rising fraction of intermediate mass atomic nuclei, in contrast to results from Telescope Array, who argue for a composition dominated by protons; in addition, the measurements reveal significant inconsistencies to hadronic interaction model predictions, in particular a measured excess of muons (see section 2.3.2). The Auger data appears at odds with results from it closest northern hemisphere counterpart, the Telescope Array. The Telescope Array measures a proton-dominated composition, which can accounted for due to different acceptances, and analysis techniques between the two detectors; however, evidence for an energy-dependent shift in the relative difference of the energy scales of the two experiments, still leave the question open, whether the differences in the energy spectra stem from experimental differences from anisotropies between the northern and southern hemispheres. Moreover, as demonstrated in [55], discrepancies are observed in energy reconstruction of air showers that could be due to the influence of the geomagnetic field and depend on the energy of the cosmic rays (see section 2.3.4).

In this thesis, I propose and study an alternative scenario with cosmic ray compositions containing a significant photon fraction; this could be achieved if photon initiated showers undergo previously unconsidered processes before entering Earth's atmosphere. The mechanism I wish to study is the so-called *super-preshower*, in which a photon produces a preshower-like cascade, but at vastly higher altitudes (at least one order of magnitude); preliminary results

show that such an effect is not inconsistent with the aforementioned mass composition data, as well as the observed inconsistencies and discrepancies. Such a scenario, if indeed successful at explaining observed phenomena, could bring back to life a whole class of the exotic models, and open the door to the study of new physics.

I will structure the thesis as follows: In chapter 2, I will give a brief introduction to the properties of cosmic rays and extensive air showers, and to the Pierre Auger Observatory (see section 2.1) for the sake of providing a more detailed overview of the objectives of cosmic ray physics; this chapter will also include a discussion of photon initiated airshowers, in particular preshowers (see section 2.2), a summary of the relevant current Auger data on the search for photons and mass composition measurements, and the aforementioned observed energy calibration discrepancies (see section 2.3), as well as a rough definition of and results of preliminary analyses on super-preshowers (see section 2.4). In chapter 3, I wish to examine two possible processes which could lead to the development of super-preshowers, namely *photon splitting* in the (geo-)magnetic field (see section 3.1) and *pair-production via interaction with solar photons* (see section 3.2), and, in chapter 4, I will re-analyse the properties of the photon initiated air showers that underwent super-preshowering with the help of simulations with *Conex* and try to verify the aforementioned preliminary results. The findings of my research will, finally, be summarised and an outlook on further research on super-preshowers will be given in chapter 5.

Chapter 2

Photons at the Pierre Auger Observatory

In the following chapter, I will give an overview of the current understanding of cosmic rays and air showers, the Pierre Auger Observatory and photon initiated air showers, as well as current insights from Auger data, with a special focus on photons searches and mass composition measurements. This outline serves to provide the necessary framework and motivation for the topic of my thesis, namely super-preshowers, which will be discussed at the end of the chapter.

2.1 Cosmic rays, air showers and the Pierre Auger Observatory

Before I discuss the current data from the Pierre Auger Observatory and how it ties to my research, it is reasonable to provide some background information on cosmic rays and the Pierre Auger Observatory to assess said research.

2.1.1 Historical background

The events leading to the discovery of cosmic rays date to the turn of the last century with the discovery of X rays (1895 by *Röntgen*), radioactivity (1896 by *Bequerel*) and the electron (1897 by *Thomson*) that had sparked new interest in the newly found particles and radiation, and their ionising potential, respectively. In the early 1900s, research in the rest conductivity of air (1900 by *Wilson*, and *Elster and Geitel* and 1903 by *Rutherford*) indicated that shielding an electroscope reduced said conductivity, which led to the conclusion that there must be some flux of ionising radiation that originates from an external source. It was thought that this radiation stems from Earth's crust where certain ores were shown to be radioactive. This assumption seemed to be confirmed by the measurement of a decreased deflection of an electrometer at the top of the Eiffel tower (1910 by *Wulf*), i.e. with increasing altitude; in 1912, however, *Victor Hess* observed in his famous *balloon experiments* (see figure 2.1) that the measured flux of the ionising radiation increases with a further rise in the altitude, indicating an extraterrestrial component, which was later confirmed by *Kohlhörster* in 1914; aptly, he named this radiation *Höhenstrahlung* (engl: altitude radiation), which marks the birth of cosmic ray physics [27].

Figure 2.1: Victor Hess before a balloon experiment to measure cosmic radiation [46].

By the late 1920s, physicists were able to show that cosmic rays predominantly consist of charged particles through the so-called *latitude effect*, where the cosmic ray intensity increases

for higher latitudes due to a weaker deflection in the geomagnetic field (1927 by *Clay*), as well as through coincidence measurements at sea level (1929 by *Bothe and Kohlhörster*). In addition, the so-called *east-west effect*, where cosmic rays arriving in the northern hemisphere have a higher intensity when originating from the west than from the east, showed that these particles have positive charge [27]. By 1949, it was clear that cosmic rays consist primarily of protons, but also of heavier nuclei, as well as of electrons; in this time, *Fermi* also considered acceleration mechanisms in magnetic fields of the interstellar medium (ISM), so-called *Fermi accelerations*, and in 1950, physicists first considered supernovas as the origin of cosmic radiation. In 1955, physicists found that antimatter was also present in cosmic radiation, though it is assumed that it originates from secondary interactions rather than antimatter sources [27].

Since the 1950s, with the development of new observational and experimental techniques, in particular accelerators and satellites (or satellite telescopes), the far reaches of the universe were probed and new elementary particles were discovered. Consequently, physicists developed the *Standard Model of Particle Physics*, as well as fundamental astrophysical and cosmological models that are united in *Big Bang Cosmology* [27]. These two theories lay the foundation of astroparticle physics, and cosmic ray physics in particular. Cosmic ray physics investigates the properties and the origins of cosmic radiation, which, in turn, help us study high energy processes within and outside our galaxy [27].

2.1.2 Cosmic ray propagation, composition and energy spectrum

Particles which originate from galactic high energy sources, usually called *primordial* cosmic rays, propagate through a column density of about $6\ \frac{\mathrm{g}}{\mathrm{cm}^2}$ through the ISM as they traverse towards Earth. It is realistic that most sources, in addition to producing the cosmic ray particles, accelerate them to energies up to the order of several EeV $= 10^{18}$ eV, by far larger than any human-made accelerator is capable of (a comparison of how these energy scales fair with those of human-made accelerators, some the energy range of some prominent accelerators are depicted in figure 2.2); these *ultra-high energy cosmic rays* (UHECRs) carry the largest energies measured in nature and are the main research focus of the Pierre Auger Observatory.

The sources of cosmic rays predominantly accelerate charged particles, which is why primary cosmic rays mainly consist of protons ($\approx 85\,\%$), heavier atomic nuclei ($\approx 12\,\%$ He nuclei and $\approx$

3 % for the remaining elements) and electrons (≈ 1 % of proton abundance); these particles can, however, create secondary particles during acceleration within the sources, many of which are unstable and ultimately decay, in part, into chargeless particles, such as photons and neutrinos [27]. The secondary particles produced in the sources, as well as their decay products, are considered *primary* particles in the context of measurement at Earth, while *secondary* particles refer mainly to the products of their interaction with the solar wind, the geomagnetic field, the radiation belt (also named *Van Allen belt*), or Earth's atmosphere [27].

As photons are the focus of this thesis, the exact composition of the charged component of primary cosmic rays is not of particular interest. As protons, in particular, do make up the overwhelming majority of the measured cosmic ray flux, however, it is worth looking into said flux via the *energy spectrum* up to in the EeV scale (see figure 2.2). In general, the flux decreases according to a power law (see equation 2.1):

$$\frac{dN}{dE} \propto E^{-\gamma}. \tag{2.1}$$

The exponent γ changes slightly at several points in the spectrum: Until about 10^{15} eV, we have $\gamma \approx 2.7$; it is believed, that cosmic rays with energies up to this order of magnitude stem primarily from our galaxy. Beyond this energy, the spectrum steepens to $\gamma \approx 3.0$; we call this the *knee* of the spectrum. At about $5 \cdot 10^{18}$ eV, the so-called *ankle*, the spectrum flattens again with $\gamma \approx 2.5$; this is believed to be due to a cross-over of the steep galactic spectrum to a hard extragalactic spectrum [27]. In some literature on the cosmic ray spectrum, there is the mention of a second knee at $\sim 10^{17}$ eV; it is controversial, however, whether this knee actually exists due to its lack of prominence, and due to the fact that the few experiments that have measured this feature in the spectrum usually are at their lowest or highest energy limits and, thus, not very sensitive [39].

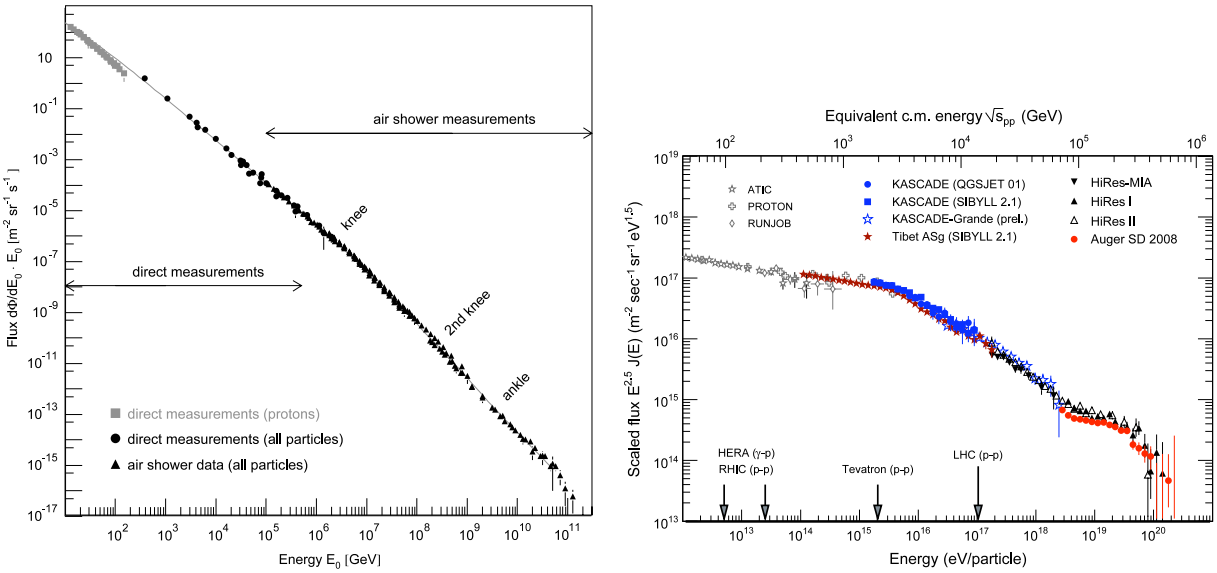

Figure 2.2: Left: energy spectrum of all particles of primary cosmic rays, also indicating the applicable range of detection via direct measurements and (indirect) air shower measurements; right: energy spectrum of all particles of primary cosmic rays multiplied by a factor of $E^{2.5}$ in order to visualise the *knee* and *ankle*, and, in addition, showing the energy produced at selected human-made accelerators on the energy axis for comparison with cosmic ray energies [17]; note that the existence of a second knee is controversial [39].

In addition, there appears to be a suppression of the flux for energies higher than about $5 \cdot 10^{19}$ eV which is expected due to the so-called *Greisen-Zatsepin-Kuzmin* (GZK) cut-off, where protons interact with the *cosmic microwave background radiation* (CMBR) and produce pions (see equation 2.2 [27]), resulting in a loss of energy of the protons in the order of up to 20 % per interaction [26].

$$\gamma + p \longrightarrow p + \pi^0, \quad \gamma + p \longrightarrow n + \pi^+ \tag{2.2}$$

Historically, there was a need of an experiment to resolve the apparent *GZK paradox* resulting from measurements by the *Akeno Giant Air Shower Array* (AGASA) [63] who oberved an apparent lack of a GZK cut-off; other experiments, such as *High Resolution Fly's Eye* (HiRes) [36] and *Yakutsk EAS Array* (Yakutsk) [65], did show the expected suppression above around $5 \cdot 10^{19}$ eV (see figure 2.3) [12]. Resolving this disagreement in data was one of the driving factors for installing the Pierre Auger Observatory.

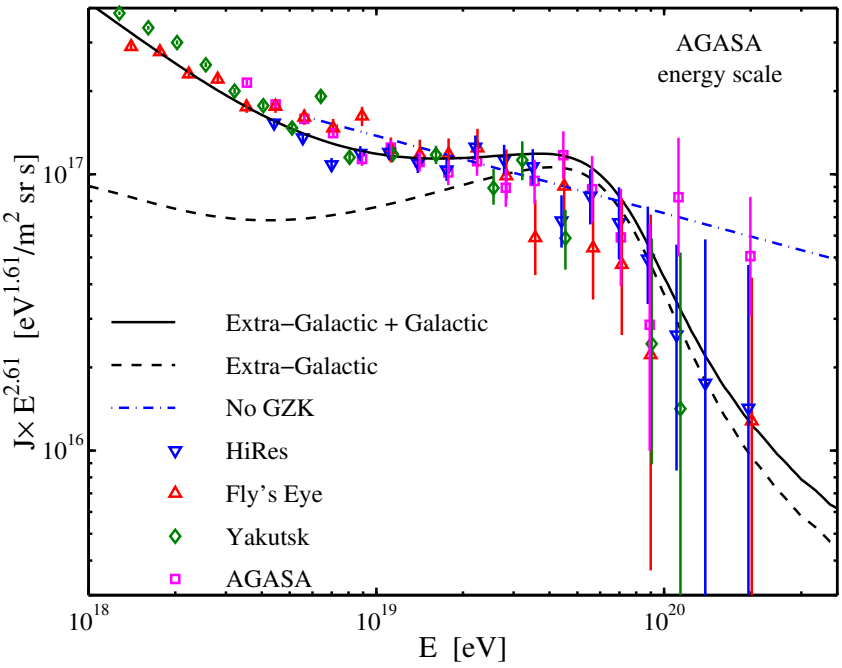

Figure 2.3: Differential energy flux from data by AGASA (pink squares), Yakutsk (green rhombus), Fly's Eye (red triangle) and HiRes (blue triangle), as well as three fits from models with cosmic rays of only extra-galactic origin (solid black line), of both galactic and extra-galactic origin (dashed black line), and no GZK cut-off (blue dashed line; extrapolation of trend $E^{-2.75}$ from energy range $6 \cdot 10^{18}$ eV to $4 \cdot 10^{19}$ eV) [12].

Due to the power law of the cosmic ray energy spectrum, the intensity drops significantly from about one particle per square meter and second at $\approx 10^{11}$ eV to the order of 1 cosmic ray per square kilometer and year at 10^{19} eV (more than 22 orders of magnitude in 8 orders of magnitude for the energy). Given the rarity of such particles with increasing energy, a measurement of the cosmic rays above the atmosphere with satellites, although offering a direct and, thus, substantially easier way of studying the primary particles, is not a viable option for the study of UHECRs. Only ground-based detectors covering large areas can provide sufficient statistics for such measurements, and, indeed, all experiments designed for this purpose, including the Pierre Auger Observatory, are ground-based. This requires a detailed understanding of the processes taking place as the cosmic rays propagate through the atmosphere that lead to so-called *extensive air showers*, which will be discussed before introducing the Pierre Auger Observatory.

2.1.3 Extensive air showers

Extensive air showers were discovered in 1938 by *Pierre Auger* and collaborators. In the following six decades, our understanding of these energetic events has significantly developed, which has also given insight into particle and astrophysics at highest energies. As cosmic ray primaries enter Earth's atmosphere, they are involved in a series of interactions with atmospheric molecules (predominantly N_2, O_2 and Ar), and produce a large number of secondaries that propagate along the trajectory of the primary particles. The secondary particles acquire transverse momenta due to scattering processes, and, as a consequence, also spread out laterally. If the primary particle is sufficiently energetic, as is the case for UHECRs, the cascade reaches sea level, where it is mainly made up of a mixture of muons and neutrinos (from hadronic interactions), and photons, electrons and positrons (from electromagnetic decay channels of hadrons, or from electromagnetic interactions, such as pair production and bremsstrahlung, of already existing leptons). In addition, *air Cherenkov*, *air fluorescence* and *radio emission* take place as the shower cascade passes through the atmosphere [26]. As an illustration, figure 2.4 depicts a simplified schematic of a proton-induced air shower.

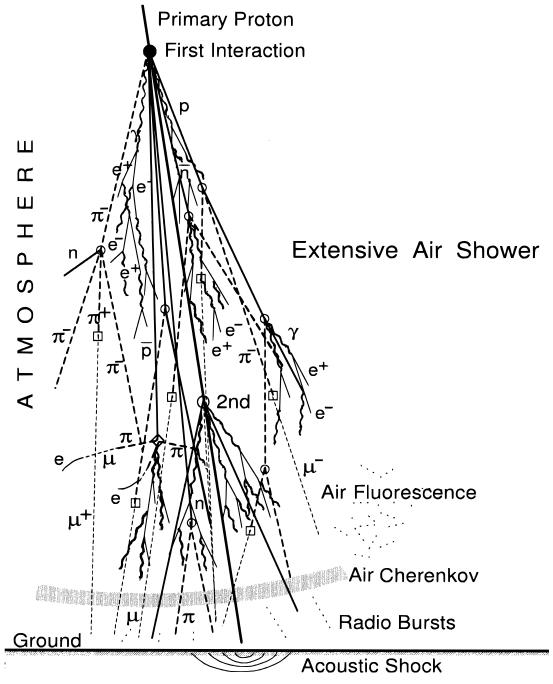

Figure 2.4: Simplified schematic of the development of an extensive air shower in the atmosphere, including common components for detection (without neutrinos) [26].

The composition as well as the lateral and longitudinal distribution of the air showers depend on the type and energy of the primary particle. We differentiate between hadronic (i.e. showers initiated by protons and heavier atomic nuclei) and electromagnetic (i.e. photon or electron induced) showers due to the main underlying interactions taking place in the shower development. Measuring the differences that arise in the air showers depending on the particle type require sophisticated detection methods because simple, and commonly used, air shower arrays can hardly distinguish between hadronic and electromagnetic showers [26]. Hybrid methods, where the same cosmic ray particle, or air shower, is being measured simultaneously by two independent, but complementary detection techniques, is one such method; it enables the simultaneous measurement of the longitudinal profile of the air showers, and of the particle density at ground level, thus significantly improving the accuracy in shower reconstruction. The Pierre Auger Observatory, which employs a hybrid detection method, has been designed to be sensitive to particles type and energy; it will be presented in the following.

2.1.4 The Pierre Auger Observatory

The *Pierre Auger (Cosmic Ray) Observatory* (PAO) is the largest ground-based detector for measuring UHECRs and inferring the origin and characteristics thereof. It is situated in the high plains of *Pampa Amarilla*, in *Mendoza Province*, Argentina. As previously mentioned, one of its key features is that it uses a hybrid detection method, namely an array 1660 water Cherenkov detectors, the *surface detector* (SD), arranged in a triangular grid with 1500 m spacing between nearest neighbours, spanning an area of 3000 km^2 which are surrounded by 24 fluorescence telescopes the *fluorescence detector* (FD); in addition, for the measurement of lower-energy cosmic rays (down to ~ 0.1 EeV, the PAO also contains 3 high elevation fluorescence telescopes overseeing 61 detectors with 750 m spacing that cover an area of 23.5 km^2. As a result, the PAO posseses an unprecedented ability to distinguish between different types of primary particles [62] (see figure 2.5).

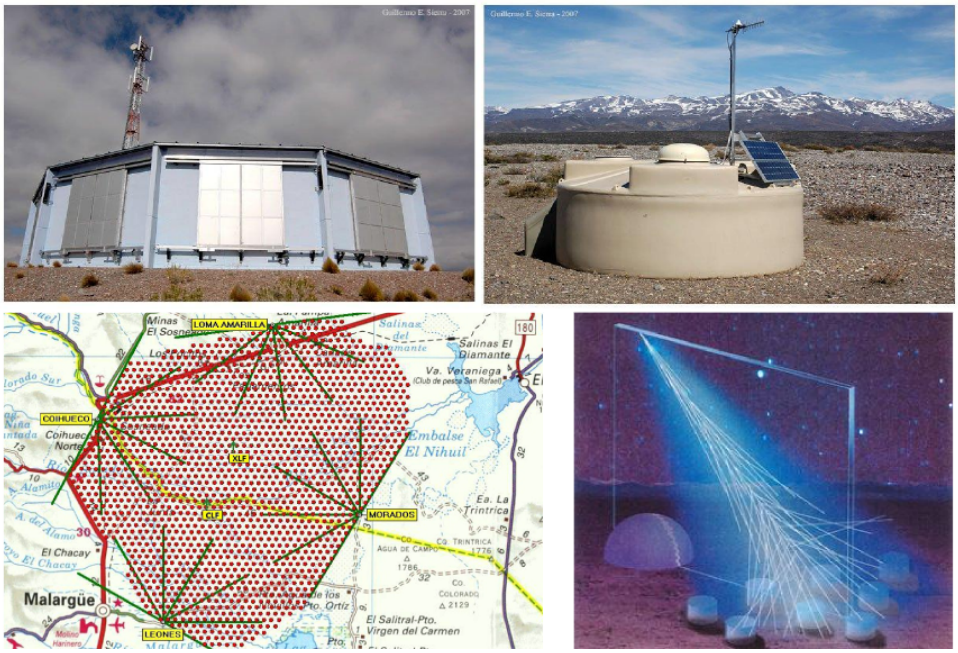

Figure 2.5: Top left: photograph of a fluorescence detector station [61]; right: photograph of a surface detector station [61]; bottom left: bird's eye view of the site of the Pierre Auger Observatory (red dots indicate the position of the SD stations, and the intersections of the green radially spread lines show the position of the FD stations) [62]; bottom right: illustration of the hybrid detection technique at the Pierre Auger Observatory [37].

The PAO was first conceived in 1991 by Jim Cronin and Alan Watson during the International Cosmic Ray Conference (ICRC) in Dublin, and construction began in 2002 after the successful installation of prototype detectors in 2001. It was completed in 2008 and has regularly been developed ever since. These updates include developments in complementary detection techniques to Cherenkov radiation and fluorescence, such as radio emission of air showers (with the *Auger Engineering Radio Array* (AERA) that will consist of 160 self-triggered antennas covering an area of 20 km^2 [8]; see figure 2.6) and microwave radiation from *molecular bremsstrahlung* (MBR) that might expand the detection ability of air showers [62].

Figure 2.6: Panoramic photograph of several radio antennas from the AERA project at Pierre Auger Observatory; a surface detector station can also be discerned in the background [61].

In addition to these developments, the PAO is experiencing a general instrumental upgrade, referred to as *AugerPrime*, which mainly consists of the installation of a plastic scintillator on top of each existing SD station, that will, henceforth, be called *surface scintillator detector stations* (SSD; see figure 2.7) [61].

Figure 2.7: Photograph of a prototype of a surface scintillator detector station for the PAO upgrade AugerPrime [61].

As of 2016, the PAO will have been operational for 8 years, but has been gathering data for almost 12 years; in this time, it has made important contributions to searches for dipolar-type anisotropies in different energy ranges, the investigation of correlations between arrival directions of cosmic rays and positions of *active galactic nuclei* (AGN), the measurement of the proton-air cross-section, and, most importantly in the scope of this thesis, the composition of cosmic rays at highest energies. This brief introduction to the PAO suffices for the pupose of this thesis; further details can, however, be found in the latest article by The Pierre Auger Collaboration [62]. Before the current Auger data is presented, photon-induced showers are discussed, since understanding their underlying processes forms the basis of my research topic.

2.2 Photon-induced air showers

Photons are in many ways of particular interest to cosmic ray physicists. On the one hand, photons are, unlike charged particles, not deflected in the magnetic fields through which they traverse before reaching Earth and, thereby, give us information on the direction in space of their sources; these sources may also be potential sources of hadronic cosmic rays [26]. On the other hand, photons have the potential to provide key insights into the production mechanisms of cosmic rays as different production models strongly influence the expected fraction of photons in the measured cosmic ray flux [53]. Substantial photon fractions are mainly predicted by *exotic* or *top-down* models, such as decays of metastable superheavy particles [14], topological defects [30] or the Z-burst model [64].

In conventional *bottom-up* models, UHECR photons are produced by either pure electromagnetic processes (mainly from electron bremsstrahlung) or by hadronic particles (predominantly by the decay of pions from the GZK effect (see section 2.1)); it is generally believed that such photons stem from hadronic rather than electromagnetic processes, as more massive hadrons can be accelerated to higher energies more efficiently and lose less energy due to synchrotron radiation, compared to electrons [26].

The propagation of photons through space is not completely undisturbed as they can be subject to interactions and scattering processes. These include electron and muon pair production in a strong Coulomb field of charged particles (in the ISM), photonuclear interactions with nucleons and nuclei of the ISM, electron pair production in magnetic fields (this will be covered in more detail in section 2.2.1), as well as interactions with photons of the CMBR (which essentially renders space opaque to light for energies between 10^{14} eV and above 10^{18} eV), but also with photons from starlight, radio waves and so on [26].

Photon initiated air showers appear similar to hadron initiated showers in many respects, but there are some key differences: Photon showers are more compact, i.e. particles move more in forward direction and closer to the shower axis than hadronic showers because the electromagnetic cascade products, on average, do not acquire a large transverse momentum; the particles in the showers are strongly bunched in thin disks of a thickness of little more than one meter that produce fast rising, narrow, and short pulses in an SD without a tail of late hadrons and muons; they have no high energy hadronic core and a negligible hadron content;

they do not have a strongly fluctuating development typical for hadronic air showers. Figure 2.8 depicts a simulation of a photon, proton and iron induced air shower which illustrates the aforementioned differences.

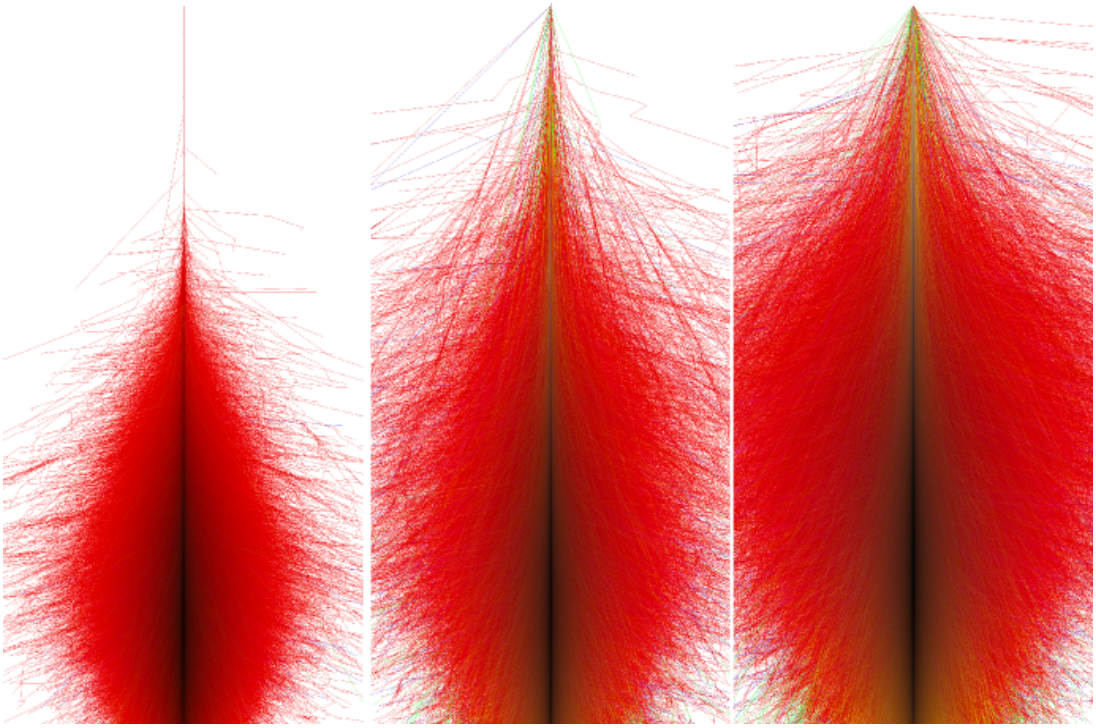

Figure 2.8: Shower images simulated with CORSIKA for different cosmic ray primaries with energies of 10^{15} eV and a zenith angle of 0° (left: photon, centre: proton, right: iron); the electromagnetic component is shown in red, hadrons are black and muons green [56].

Moreover, photon induced showers are expected to have a very low muon content, only about a percent of that found in hadron induced showers as muons are the result of either photo-nuclear reactions, in particular photo-pion production [26] and direct muon-antimuon pair production. However, the photonuclear cross section used in predictions, as for all hadronic interactions, is extrapolated from lower energies, which introduces uncertainties to the actual muon content of photon initiated showers; these uncertainties are expected to be in the order of 15 % for photon initiated showers [53]. Figure 2.9 shows different extrapolations of the photonuclear cross-section based on different models.

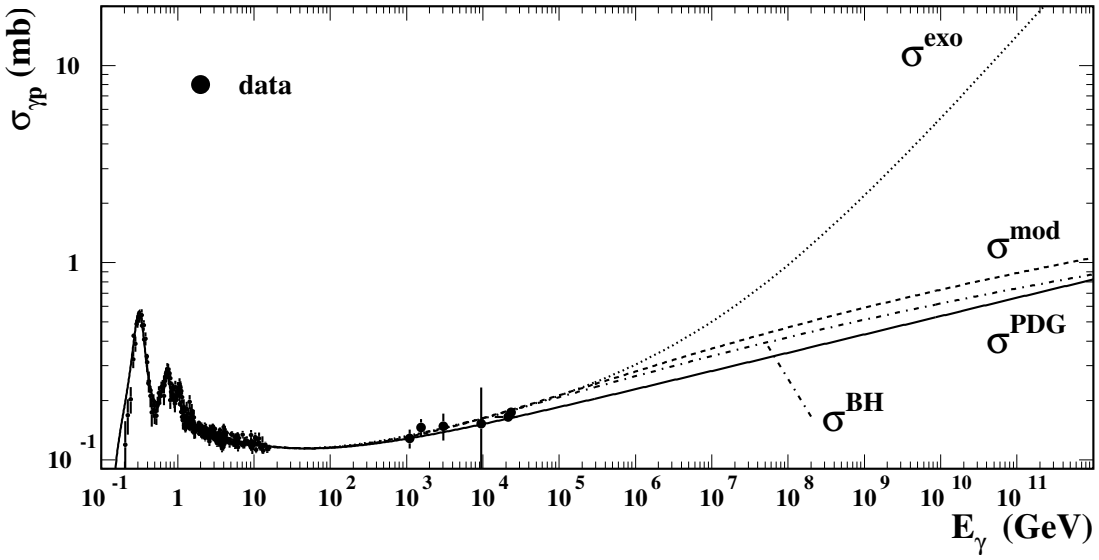

Figure 2.9: Different extrapolations of the photonuclear cross-section $\sigma_{\gamma p}$ from data, which is also shown; σ^{PDG} refers to extrapolations from the Particle Data Group (PDG) [53].

In addition, photon-induced air showers develop deeper into the atmosphere compared to hadronic showers of similar energies: This can be used to discriminate between a hadron or photon primary [1]; a raised photonuclear cross-section would, however, also impact the depth of the air shower but only by an atmospheric depth of around $10\ \mathrm{g\,cm^{-2}}$ [53].

Being able to distinguish these subtle differences in photon and hadronic air showers requires very sophisticated detection methods, which the PAO possesses with its hybrid detection method, giving it an unequalled sensitivity to photons at energies above 10^{18} eV. The status quo on the search of photon primaries will be discussed in section 2.3. First, we will discuss two important effects relevant for photon initiated showers that become particularly important for ultra-high energies, namely *preshowering* and the *LPM effect*.

2.2.1 Preshowers

As mentioned above, one of the ways (primary) photons can interact before being detected is via electron pair production in magnetic fields, which differs from pair production in Coulomb fields in that the magnetic field strength is weak. This process only occurs for photons of very high energies (above 10^{19} eV [35]), though, and has become relevant within the scope of the

phenomenon of *preshowering*, which occurs when an ultra-high energy photon approaching Earth interacts with the geomagnetic field far above the top of the atmosphere and creates an electron-positron pair. The newly created electrons (or positrons), then, undergo magnetic bremsstrahlung. This process can repeat itself several times before the particles enter the atmosphere, which results in a small, highly collimated and very energetic shower. The subsequently initiated airshower, as the particles enter the atmosphere, can resemble that of single heavy primaries, such as iron, which complicates the determination of the primary mass at these energies − of course, only, if photons of such energies exist [26]. For this reason, the key characteristics of photon initiated air showers containing preshowers must be studied to enable the discrimination between such showers and those initiated by hadrons.

The conversion probability depends on the primary photon energy, as well as the magnetic field component transverse to the propagation direction of the photon B_{T}; for a traversed distance R, the probability amounts to (see equation 2.3 [33]):

$$P_{\mathrm{conv}} = 1 - \exp\left[-\int_0^R \alpha\left(\chi(r)\right)\right] dr, \tag{2.3}$$

where $\alpha = \frac{\alpha_{\mathrm{em}}\, m_{\mathrm{e}}\, c}{2\hbar}\frac{B_{\mathrm{T}}}{B_{\mathrm{cr}}} \cdot T(\chi)$, $\alpha_{\mathrm{em}} \approx 1/137$ is the electromagnetic coupling constant, m_{e} is the electron rest mass, c is the speed of light, $\hbar = h/2\pi$ is the reduced Planck constant, $B_{\mathrm{cr}} = 4.414 \cdot 10^{13}$ Gs quantum critical field (which will be explored in more detail in chapter 3), $\chi = \frac{h\,\nu}{m_{\mathrm{e}}\, c^2}\frac{B_{\mathrm{T}}}{B_{\mathrm{cr}}}$ and $T(\chi)$ is the magnetic pair production function, which can be approximated as $0.60\,\chi^{-1/3}$ for $\chi \gg 1$ (which is mostly the case for UHE photons). In figure 2.10, the conversion probability is plotted as a function of energy for weak and strong magnetic fields, and the directional dependence of the conversion probability is shown in figure 2.11 for different primary energies.

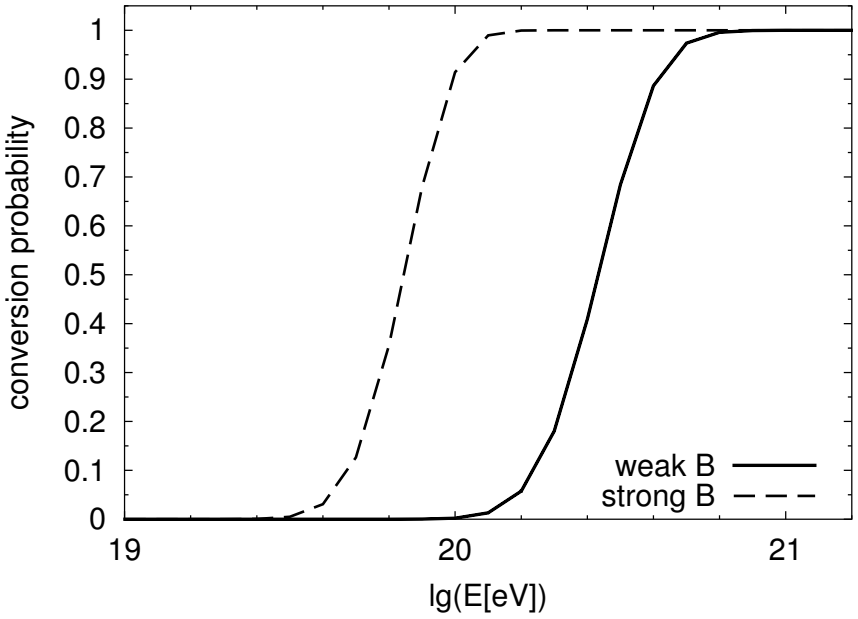

Figure 2.10: Probability of the conversion of a photon into an electron-positron pair as a function of energy for weak (solid line) and strong magnetic fields (dashed line); in this scope of the analyses, "weak" fields are characterised by arrival the direction $\theta = 70^\circ$ (zenith) and $\phi = 0^\circ$ (azimuth) and "strong" ones by $\theta = 60^\circ$ and $\phi = 177^\circ$ [33].

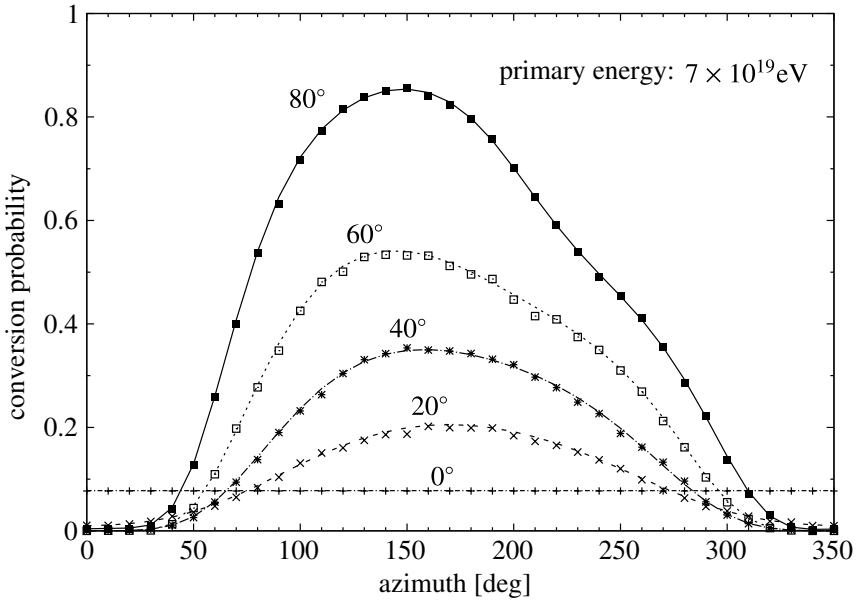

Figure 2.11: Probability of the conversion of a photon into an electron-positron pair as a function of the azimuth angle for different zenith angles θ (indicated in the plot) and an energy of $7 \cdot 10^{19}$ eV; the azimuth increases in the counter-clockwise direction and $\phi = 0$ refers to showers arriving from the geographical north [34].

We see that the probability approaches 1 for energies above 10^{20} eV for arrival directions with large transverse magnetic field components B_{T} and even for arrival directions with small B_{T} for photon energies above 10^{21} eV. For photons of energies between $5 \cdot 10^{19}$ eV and $5 \cdot 10^{20}$ eV the conversion probability depends strongly on the arrival direction of the photon, which may serve as a characteristic fingerprint of photons as the primary particles [33]. The probability generally increases with the zenith angle (except for azimuth angles around 0°), and is largest for azimuth angles of $150^{\circ} - 180^{\circ}$ depending on the zenith angle, i.e. showers that arrive from directions towards the magnetic south pole and that reach lower altitudes and, thereby, stronger magnetic fields, when viewed from the PAO [33].

In addition to the dependence on the arrival direction, which becomes less pronounced for higher energies, another key feature of photons undergoing preshowers is a negative elongation rate (defined in section 2.3.2) for weak field directions as secondary photons produced via bremsstrahlung have lower energies and are less likely to convert into an electron-positron pair, and thereby have a deeper X_{max} (also defined in section 2.3.2) [33]. In particular for conversions at lower altitudes, the development of the initiated shower can fluctuate significantly [51], which is why the root mean square of X_{max} is larger for weak magnetic field directions [33].

Finally, it is useful to summarise typical features of a preshower: Starting with a 10^{20} eV photon primary, the first conversion is at an altitude of $\sim$ 1000 km a.s.l.[1]; by the time the preshower has reached the atmosphere (~100 km a.s.l.) it will contain one or a few $e^{\pm}$ pairs (energy 10^{18} eV) and around 500 photons (energies ranging several orders of magnitude, some 10^{19} eV) [52].

2.2.2 Landau-Pomeranchuk-Migdal effect

The *Landau-Pomeranchuk-Migdal* (LPM) effect is a process that, like preshowering, becomes relevant at very high energies, where, due to quantum mechanical interference of different scattering centres, both the pair production and bremsstrahlung cross sections are suppressed. This leads to a slower initial development of the electromagnetic cascade which is stretched and eventually penetrates deeper into the atmosphere [26].

[1] a.s.l. stands for "above sea level"

This effect can be attributed to the fact that bremsstrahlung and pair production take place over an extended region and have an effective average collision distance with nuclei. It can be shown that the effect becomes relevant in the case of bremsstrahlung for electron energies E and resulting photon energies E' of (see equation 2.4 [26])

$$\frac{E\,(E-E')}{E'} > 4 \cdot 10^{12}\,\chi_0\ \mathrm{eV\,cm^{-1}}, \tag{2.4}$$

where χ_0 is the radiation length of electrons in a certain medium. It is important to note that the retardation of the shower can lead to the misinterpretation of the primary energy [26].

Given this overview, current data from the PAO, in particular on searches for cosmic ray photons and on the mass composition, can be discussed.

2.3 Current data

Before we turn to the current Auger data, it is important to mention how measured air shower data is compared to actual predictions. As briefly mentioned in section 2.1, the PAO is a ground-based experiment that measures cosmic rays *indirectly*, i.e. through the reconstruction of extensive air showers. Inferring the characteristics of the primary cosmic ray particle from the air shower requires a detailed understanding of how they affect its development. This is done at the PAO via simulations of air showers containing our best understanding of particle physics, cosmic ray physics and astrophysics, that govern the underlying processes of air shower development. Simulation and reconstruction are compared via *observables* that are sensitive to the type and energy of the primary particle. This comparison is not very straightforward, however, as the hadronic part of the shower cascade is largely phenomenological due to there not being a general theory of hadronic interactions. As a result, the comparison is carried out by routinely modifying the parameters and (mainly hadronic) models to find the best agreement with the accelerator data [26].

In the discussion of the data, I will focus mainly on the UHECR photon searches (see section 2.3.1) and on mass composition measurements (see section 2.3.2), as they are directly related to my research topic. An additional aspect, namely discrepancies in reconstruction using hybrid and stereo measurements (see section 2.3.4), is also relevant in that it provides further motivation for said topic. When mentioning the relevant observables and how one can infer something on the composition from them, I will, when suitable, include how they can be detected at the PAO.

2.3.1 Search for UHECR photons

As pointed out in section 2.2, photons offer a unique opportunity to identify the sources for UHECRs due to their lack of deflection in the galactic and extra-galactic magnetic fields. The photon flux depends on the composition and maximum energy of cosmic rays at the sources and the emissivity, distribution and cosmological evolution of the accelerators [16]. We can, therefore, set constraints on the properties of these sources with the help of photons if they are created near the source. I also mentioned that the fraction of photons in the cosmic ray

flux is indicatory of their production mechanisms. While low fractions in the order of 0.1 % are expected from bottom-up models, where photons stem from the GZK-effect via the decay of pions, fractions up to 50 % are predicted from exotic, top-down models.

In trying to detect photons, often *multivariate analyses* (MVA) using *boosted decision trees* (BDT) are utilised which combine several photon-hadron discriminating observables. They include:

- the depth of the shower maximum X_{max} in terms of energy deposit (see section 2.3.2 for more details);
- the use of the so-called *Greisen function*, which was originally introduced to describe the longitudinal profile of purely electromagnetic showers and should, thus, fit better to photon-induced showers compared to hadronic ones; the observables are the goodness-of-fit χ^2/ndf, as well as the ratio between the primary energy from a Greisen fit and from the conventially used *Geiser-Hillas* fit $\frac{E_{\text{Gr}}}{E_{\text{GH}}}$;
- the lateral distribution of the signal measured by SD (photon-induced showers have a steeper lateral distribution, as they, essentially, lack a muon component);
- differences in the arrival time at the ground stations (for a fixed distance from the shower core, shower particles which develop closer to ground level, such as those initiated by photons, are expected to have a larger spread in their arrival times) [1].

If detected, photons can be used as a complementary method of calibrating the absolute energy scales of UHECRs with similar or even superior accuracy to conventional methods, depending on the statistics [32].

The Pierre Auger Collaboration [1] undertook analyses for the energy range from $10^{17.3}$ eV to $10^{18.5}$ eV (to have higher statistics and to avoid processes, such as preshowering, which lead to showers that more resemble hadronic ones), using several cuts to the data to ensure a high-quality selection. However, no point sources for photons could be found; moreover, upper limits to the photon flux of 0.035 photons $\text{km}^{-2}\,\text{yr}^{-1}$ on average, with a maximum of 0.14 photons $\text{km}^{-2}\,\text{yr}^{-1}$ were set with a confidence level of 95 % (see figure 2.12).

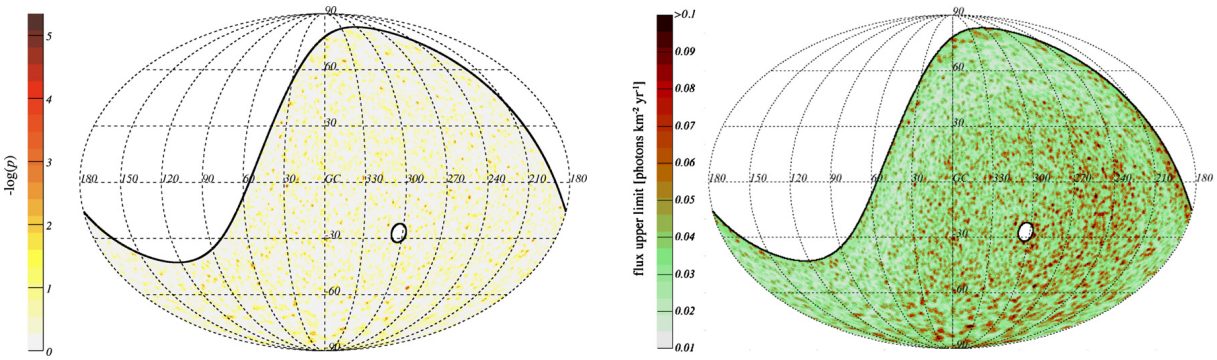

Figure 2.12: Celestial maps in Galactic coordinates; left: $-\ln p$ values (p indicates the probability of a uniform distribution; $p = 4.5 \cdot 10^{-6}$ (the minimum value) stands for a probability of chance occurrence of 36 %), right: photon flux upper limits [1].

In the study of the diffuse flux of photons, the additional condition that the showers arrive from a zenith angle range of $30^\circ < \theta < 60^\circ$ to a larger observation depth was included, which ensures that photon-induced showers are fully developed; in addition, the energy range of choice was $E_\gamma > 10$ EeV, for which preshowering and the LPM effect need to be taken into account [16]. Applying all the selection criteria to the data, 4 events survived the cuts. Assuming a differential flux of (see equation 2.5):

$$dN(E) \propto E^{-2}, \tag{2.5}$$

limits were set to the photon flux constraining the most optimistic predictions of cosmogenic photon fluxes that assume a pure proton composition at the sources, and strongly disfavouring any top-down models that entail different exotic local processes as sources of UHECR photons [16, 22] (see figure 2.13).

Given the current data and assuming the validity of the interaction models used, evidence for EeV photon sources is lacking, and a significant fraction of cosmic ray photons (mainly from top-down models) seems to be ruled out. Based on this, composition measurements that are discussed in the following are carried out with the assumption that the bulk of the UHECR flux is hadronic.

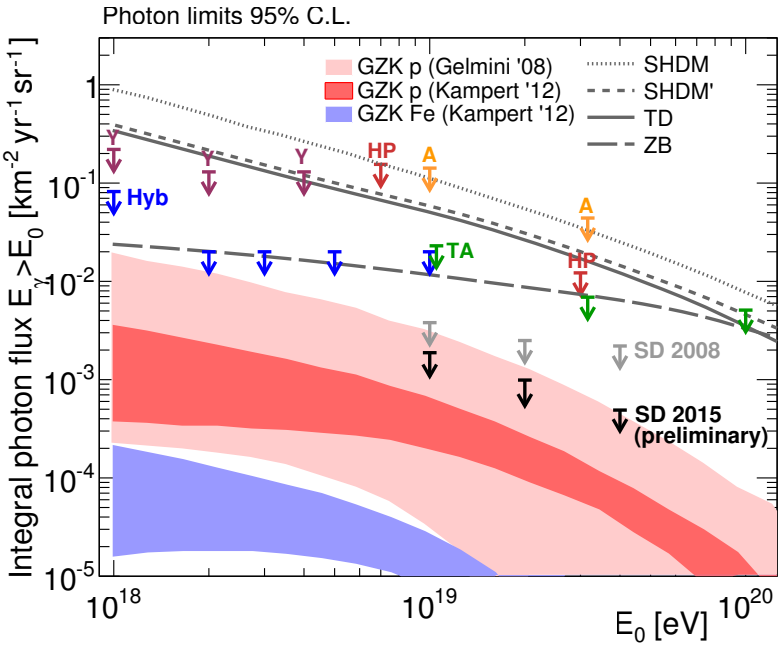

Figure 2.13: Upper limits at 95 % confidence level to the diffuse flux of UHE photons (black arrows, SD 2015), as well as previous results from the PAO (grey, SD 2008, and blue arrows, Hyb), Telescope Array (green arrows, TA), Yakutsk (dark red arrows, Y), Haverah Park (red arrows, HP), AGASA (orange arrows, A) and predictions from several top-down (dashed lines) and cosmogenic photon models (red and blue bands) [16].

2.3.2 Composition of cosmic rays at ultra-high energies

As the energy spectrum of cosmic rays from the ankle onwards appears to indicate a higher fraction of cosmic rays of extragalactic origin [27], it is natural to assume that the composition of cosmic rays could be affected by this. For example, a larger fraction of heavier atomic nuclei at higher energies is expected for acceleration mechanisms involving magnetic fields due to their higher charges (e.g. [45]).

Several observables can be used to measure the composition of cosmic rays. The ones discussed in this thesis are the depth of the maximum energy deposit, the number of muons and the rise time. A definition, if necessary, and the dependence on the composition of each of these observables will be discussed in detail in the relevant sections.

Composition inferences from the depth of maximum energy deposit $X_{\max}$

One observable with which the PAO infers about the mass composition of the cosmic ray flux is the (longitudinal) energy deposit of the air shower as a function of the atmospheric slant depth X, $\frac{dE}{dX}$; it can directly be measured with the FD. An important parameter that can be inferred from $\frac{dE}{dX}$ is the depth at which it reaches its maximum $X_{\max}$. Given that heavier nuclei primaries have larger cross-sections and number of nucleons (the latter fact meaning less energy per nucleon) the showers they induce are expected to be higher, faster and fluctuating less from shower to shower. In addition, $X_{\max}$ is related to the nuclear mass A of the primary particle, or rather its logarithm, $\ln A$ [2, 42].

The properties of the first few hadronic interactions in the shower cascade do fluctuate to such an extent, however, that the primary mass can only be inferred statistically from several air showers via superposition of each $X_{\max}$. Assuming that the set of showers involved in the statistical analysis are produced by different nuclei of mass A_{i} that can be treated as a superposition of A_{i} nucleons with energy $E' = \frac{E}{A_{\mathrm{i}}}$, where E is the energy of the nucleus, the global distribution of the measured $X_{\max}$ can be expressed as follows (see equation 2.6 [2, 42]):

$$f(X_{\max}) = \sum_i p_{\mathrm{i}} \cdot f_{\mathrm{i}}(X_{\max}), \tag{2.6}$$

where p_{i} refers to the fraction of the primary particle of type i. With this distribution, one can make inferences about the mass composition from $X_{\max}$ by analysing its first two moments (see figure 2.14), but also by converting them to the first two moments of the distribution of $\ln A$ with the help of hadronic interaction models (see figure 2.15) [2, 9]. In addition, a binned maximum likelihood fit to the measured $X_{\max}$ distribution [3] is used to find the best combination of nuclei (using different scenarios with protons, iron, nitrogen and/or helium; see figure 2.16) [42].

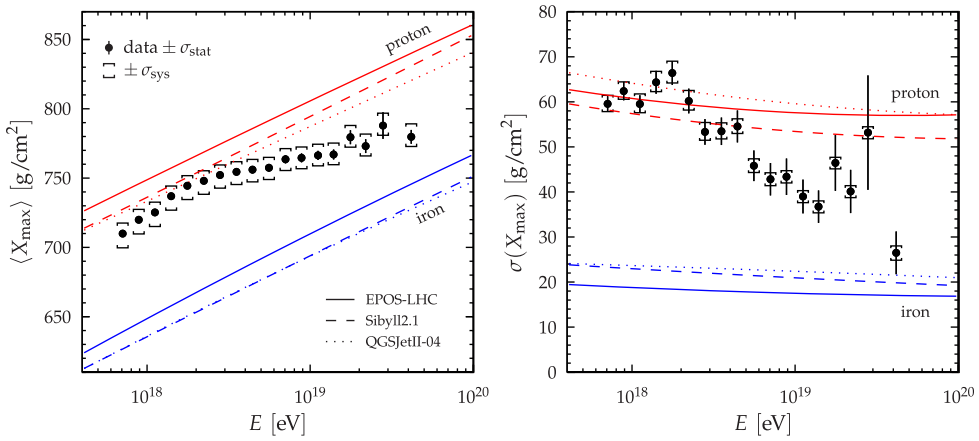

Figure 2.14: Energy evolution of the first two central moments of the $X_{\max}$ distribution compared to air-shower simulations for proton and iron primaries [2, 42].

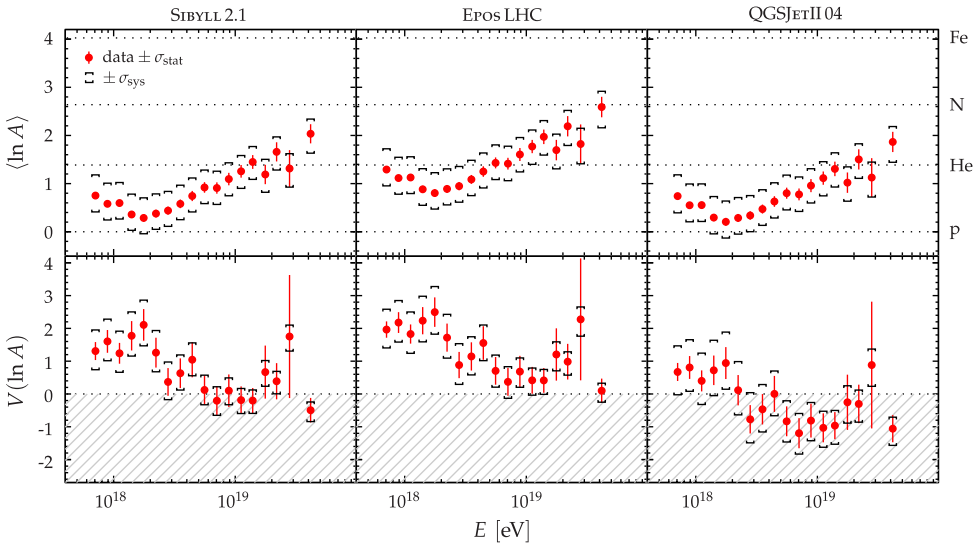

Figure 2.15: Average of the logarithmic mass and its variance estimated from data using different interaction models; the non-physical region of negative variance is indicated as the gray dashed region [2, 42].

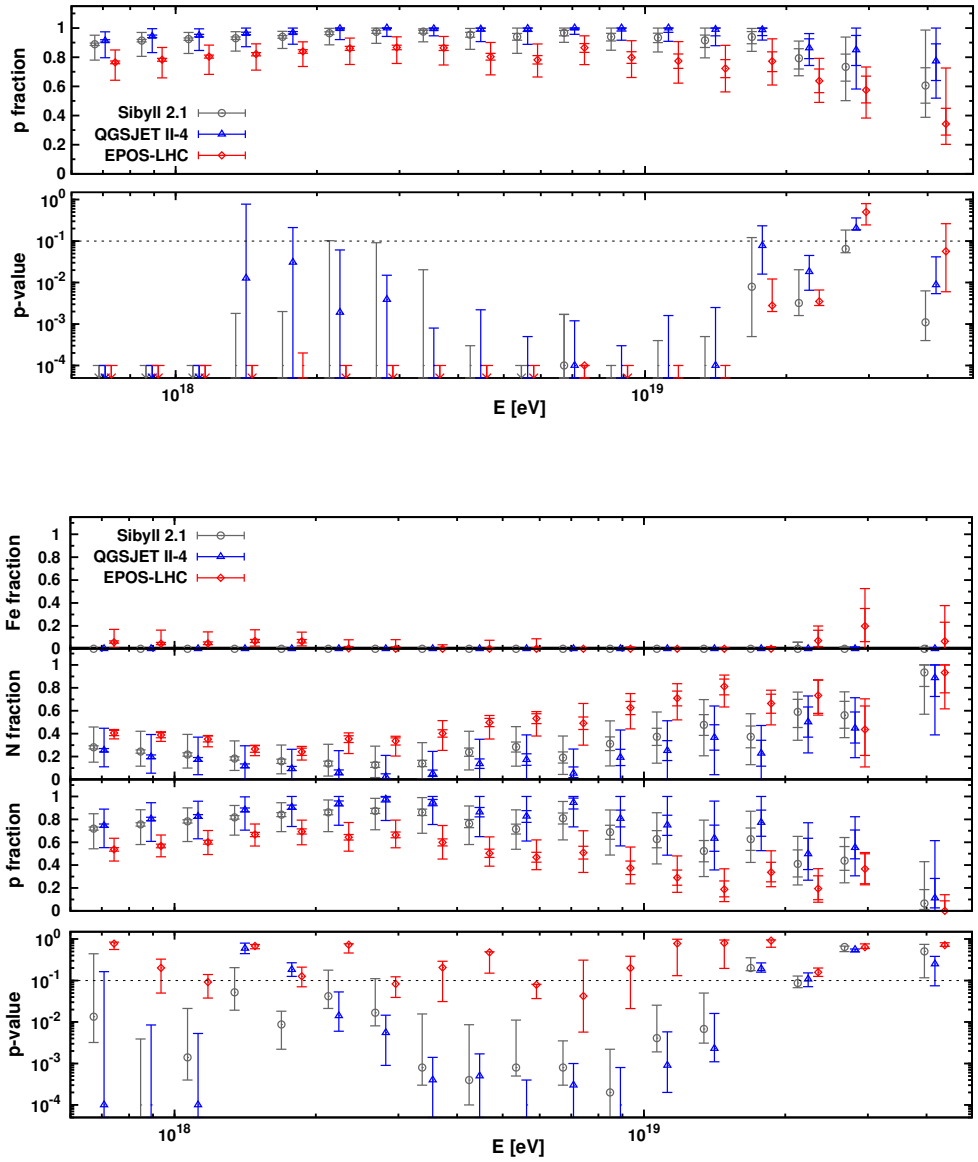

Figure 2.16: Fitted fraction and quality for different scenarios of particle composition; top: protons and iron nuclei only, bottom: complex mixture of protons, helium nuclei, nitrogen nuclei, and iron nuclei; lowest panel of each plot shows the p-values; the results from the various hadronic interaction models are slightly shifted in energy for better viewing (Sibyll 2.1 to the left, Epos-LHC to the right) [3, 42].

It is worth reiterating that the interpretation of the data is dependent on the model predictions; at these energies, they rely heavily on extrapolations of data from the *Large Hadron Collider* (LHC) [42]. As a result, it is entirely possible that any observed trends in the composition are, in fact, due to deviations from these extrapolations instead of being indicatory of a true mass

composition trend [3].

To further analyse the X_{max} data, the PAO uses a parameter called the *elongation rate* $D_{10} = \frac{d\langle X_{\text{max}}\rangle}{\lg E}$, which is expected to be constant with the energy for pure showers, i.e. those initiated by only one type of primary particle. The data is not consistent with a constant slope, however, and corresponds best with a break point in the linear fit at approximately $E = 10^{18.3}$ eV. Assuming that we can rely on our current models, the X_{max} data indicated a transition from light to heavier nuclei from this energy up to approximately $E = 10^{19.6}$ eV [42].

The conversion of X_{max} to $\ln A$ is model-dependent [2, 9]; using three different hadronic interaction models, *Sibyll2.1* [11], *Epos-LHC* [47], and *QGSJet-II-04* [44], the different values of $\ln A$ that can be seen in the aforementioned order from left to right in figure 2.15. The data is consistent with the results from figure 2.14.

Good description of the X_{max} data can be reached assuming varying mixtures four elements; it is inconsistent with a composition dominated by protons, as well as with a large contribution from iron nuclei [3, 42]. Depending on the interaction model used, the fraction of the intermediate masses differ substantially; for Epos-LHC, the mixture is dominated by nitrogen nuclei, the QGSJet II-04 simulation favours helium nuclei, and Sibyll 2.1 leads to a mixture of the two [3]. All three models considered yield similar results for the energy evolution of the proton fraction.

Composition inferences from muons

Another tracer that can be used for mass composition studies is the number of muons; this is due to the fact that heavier nuclei are expected to produce more muons than lighter ones [42]. The detection of muons is done with the SD tanks via the amount and size of the Cherenkov pulses they emit in the water; electromagnetic particles (electrons, positrons, and photons) are more numerous than muons, whereas their mean energy at ground level is about two orders of magnitude smaller (some 10 MeV versus a few GeV), leading to a large number of relatively small pulses from the electromagnetic particles and small number of large pulses from the muons [40]. The discrimination power is, thus, rather limited, which is why it is useful to focus on (strongly) inclined showers, i.e. those at large zenith angles, as the electromagnetic component is mostly absorbed by the atmosphere due to a larger traversed atmospheric depth

[4, 42].

The muon number for each shower is derived by fitting a simulated reference profile of the lateral muon density distribution at the ground to the measurement to get an unbiased and (almost) model-independent estimator [4]. Using hybrid events, the muon number estimator, R_μ, can be correlated with the energy of each shower estimated with the FD. The *muonic elongation rate*, the evolution of the average muon content $\langle R_\mu \rangle$ with energy, $\frac{\langle R_\mu \rangle}{(E/10^{19}\ \mathrm{eV})}$, is useful for comparison with hadronic models predictions as the scaling due to the energy is diminished and the effect of A on the muon number becomes apparent [4]; in addition, one can compare the values of $X_{\max}$ from the muon measurements and compare them with simulations of different hadronic primaries to retrieve information on the mass composition (see figure 2.17).

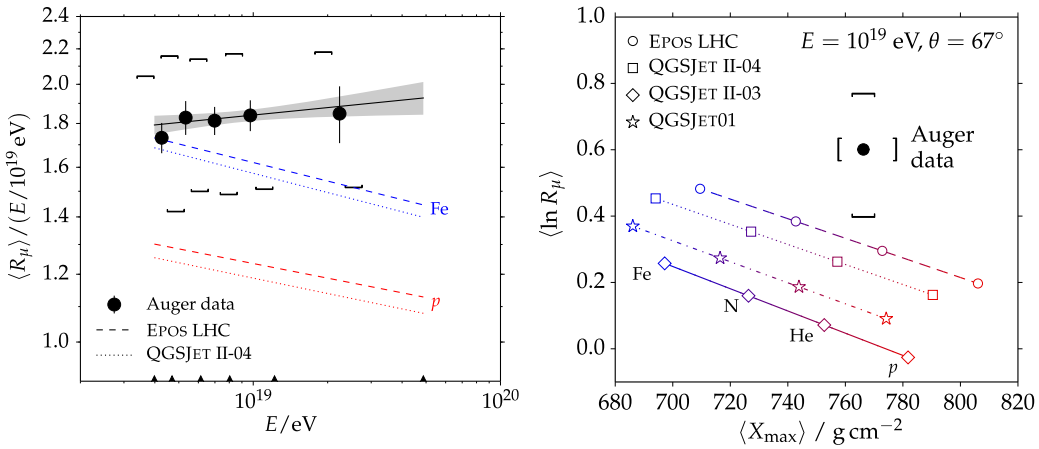

Figure 2.17: Left: average muon content $\langle R_\mu \rangle$ per shower energy E as a function of the shower energy compared to simulations; right: the average logarithmic muon content $\ln R_\mu$ as a function of $X_{\max}$ at 10^{19} eV compared to simulations; square brackets indicate the systematic uncertainty of the measurement, and the grey band in the top plot represents the statistical uncertainty of the fit [4, 42].

In both cases, model predictions are not consistent with the data; there appears to be a measured excess of muons. The models do not describe the longitudinal development of the shower correctly.

Another important quantity that can be used to obtain information about the mass composition is the *muon production depth* (MPD), or its maximum $X^{\mu}_{\max}$ (similarly to $X_{\max}$); it can be inferred from SD data by analysing the temporal and lateral distribution via measurement of

the particles' arrival times [42]. The average maximum MPD $\langle X^{\mu}_{\max} \rangle$ can, then, be compared with model predictions (see figure 2.18); $\langle X^{\mu}_{\max} \rangle$ can be converted into $\langle \ln A \rangle$, just as for $\langle X_{\max} \rangle$ (see figure 2.19).

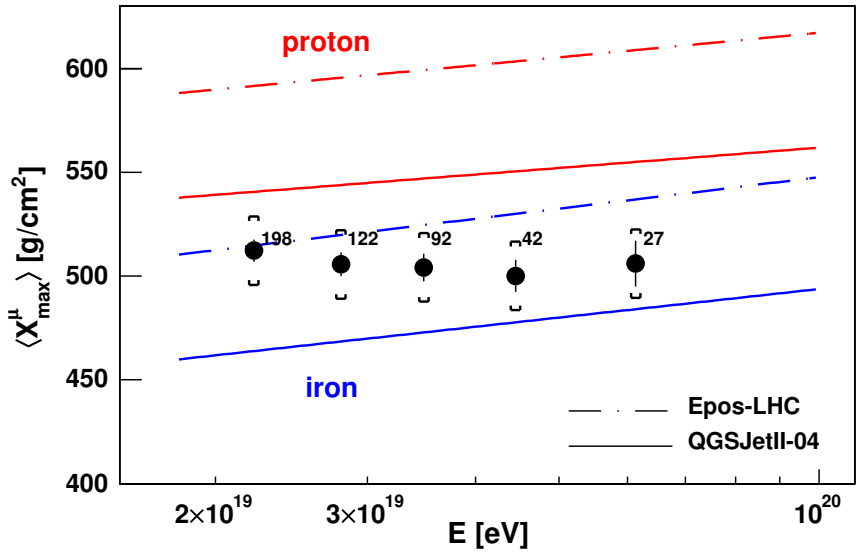

Figure 2.18: $\langle X^{\mu}_{\max} \rangle$ as a function of energy, as well as the predictions based on different hadronic models for protons and iron; numbers indicate the number of events in each energy bin, and brackets represent the systematic uncertainty [5, 42].

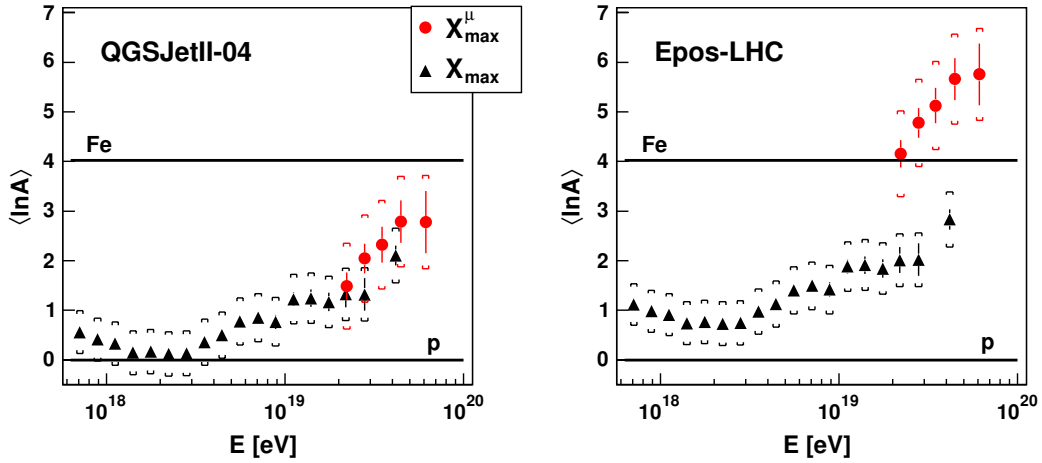

Figure 2.19: $\langle \ln A \rangle$ converted from $\langle X^{\mu}_{\max} \rangle$ (red circles) and $\langle X_{\max} \rangle$ (black triangles) as a function of energy using different hadronic interaction models (left: QGSJet II-04, right:Epos-LHC); brackets correspond to the systematic uncertainties [5, 42].

The models yield different predictions for $\langle X^{\mu}_{\max} \rangle$, as well as for $\langle \ln A \rangle$; both observables trans-

form into consistent mass values for QGSJet-II-04, whereas for Epos-LHC, the data indicates heavier nuclei than iron [4, 42].

The aforementioned data demonstrate very well the power of the hybrid detection capabilities of the PAO at highest cosmic ray energies, in particular with respect to muon measurements, but also the potential of the individual detectors, as seen for the X_{max} measurements. With respect to information on the mass composition, we see that, for measurements involving X_{max}, there is a transition from light to intermediate mass nuclei with the energy, whereas for muon measurements, the hadronic interaction model predictions are not consistent with data; on the one hand, we see a muon excess in the data (which indicates the dominance of heavier nuclei than iron in the cosmic ray flux and vice versa), and on the other hand, the trend of the parameters derived from muon measurements with the energy do not fit with the measured trends. Consequently, these results show the limitations of hadronic interaction models at larger than LHC energies [42].

Composition inferences from rise time measurements

Another way to infer on the mass composition of the cosmic ray flux is to use the *rise time* of a signal arriving at an SD station [57]. Using the average deviation of the mean rise time in an event, one can correlate this parameter to calibrate X_{max} with a small number of hybrid events and carry out mass composition measurements with SDs only by comparing the rise time behaviour as a function of shower core distance for data and simulations [18].

Latest results show that the data lies between proton and iron simulation, consistent with the results from X_{max} measurements; however, a possible dependence of the composition on the zenith angle was also observed [18].

2.3.3 Tension between Auger and Telescope Array data

Next to the PAO, the *Telescope Array* (TA) is the largest UHECR experiment. Therefore, comparing data between the two experiments is of vital importance in assessing their significance. The TA is situated near the city of Delta in Millard County in western Utah and is the largest

UHECR detector in the northern hemisphere; like the PAO it is a hybrid detector consisting of three FD stations and a ground array of 507 scintillator SDs that are on a square grid with 1200-meter spacing [10].

The TA has measured a different cosmic ray composition than the PAO, namely an $X_{\max}$ development with energy consistent with a purely protonic composition (see figure 2.20) [7]. Preliminary detailed comparisons, which take into account the different acceptances, and analysis techniques between the two detectors, do indicate that the results are in good agreement, though [6].

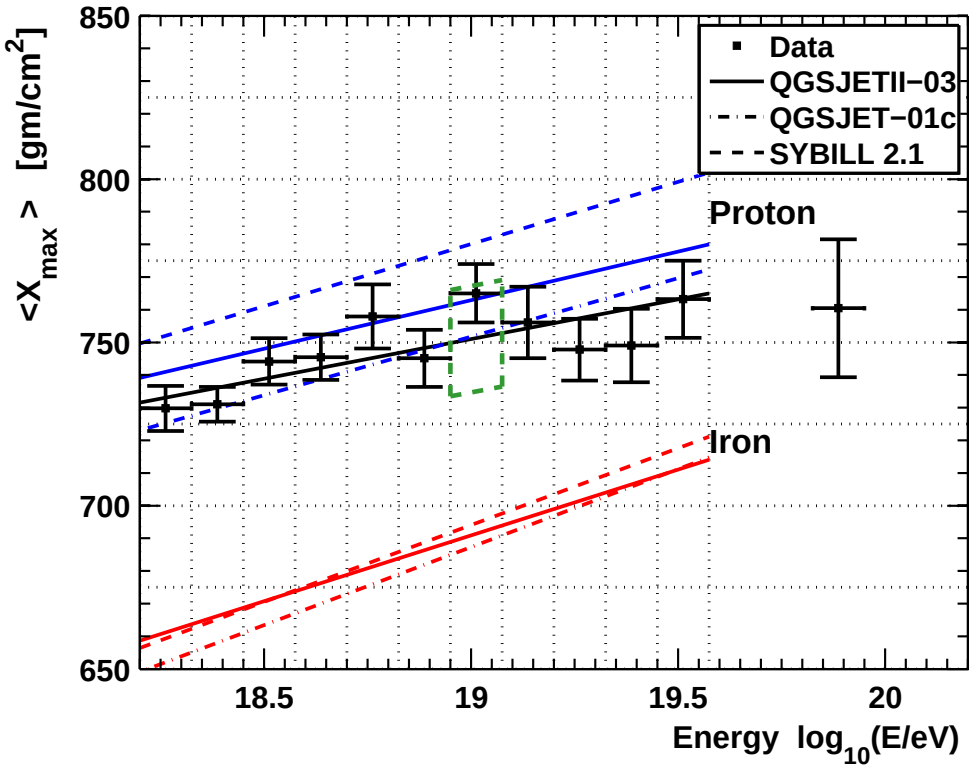

Figure 2.20: Energy evolution of the first two central moments of the $X_{\max}$ distribution from TA data compared to air-shower simulations for proton and iron primaries [7].

However, measurements of the flux in the common field of view of the experiments with which a systematic shift in the energy scale between both experiments can be derived, Deligny et al. [21] found evidence for an energy-dependent shift in the relative difference of the energy scales of the experiments. Therefore, it is still not clear whether the differences in the energy spectra

stem from differences between the experiments or from anisotropies between the northern and southern hemispheres [21].

2.3.4 Tension stereo and hybrid energy reconstruction

As can be seen in section 2.3.2, the measurements favour a mixed composition of cosmic rays at ultra-high energies, although inferences from muon measurements reveal clear inconsistencies between model predictions and data, in particular a muon excess. As is described in detail in section 2.2, photons are disfavoured from the measurements and a predominantly hadronic composition is assumed, mainly based on arguments from the depth of maximum energy deposit X_{max}; given the aforementioned discrepancies with respect to the muon numbers, it might be worthwhile revisiting alternative, exotic model predictions for the cosmic ray composition. In addition, analyses of hybrid (combination of SD and FD) and stereo (combination of two separate FDs) data expose further tension between data and simulations that could be solved by alternative composition scenarios.

Systematic discrepancies within and between hybrid and stereo reconstruction of the primary energy have already been documented by Novotny et al. [43] and Porcelli [49]; the origin of this discrepancy has been further analysed by Schauer [55] by investigating a possible miscalibration of individual FD stations, differences in the reconstruction of Cherenkov light between data and simulations, as well as the dependence of the discrepancy on the energy, on the orientation of the shower with respect to the magnetic field (or, rather, the magnitude of the transverse magnetic field component B_{T}), and on the angle between the projections of the magnetic field vector and the viewing vector onto the shower plane perpendicular to the shower axis ϕ (see figure 2.21).

The results are that a miscalibration cannot fully account for the energy difference and that Cherenkov light is underreconstructed; moreover, the discrepancy shifts with the energy (see figure 2.24), and it is strongly dependent on ϕ (see figures 2.22 and 2.23) and its prominence is largest for weak transverse magnetic field components B_{T} (see figure 2.24), which might suggest dependence on the magnetic field.

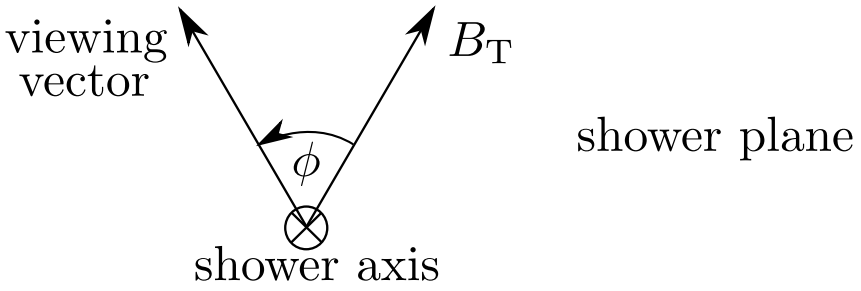

Figure 2.21: Definition of the angle between the projections of the magnetic field vector and the viewing vector onto the shower plane perpendicular to the shower axis ϕ [55].

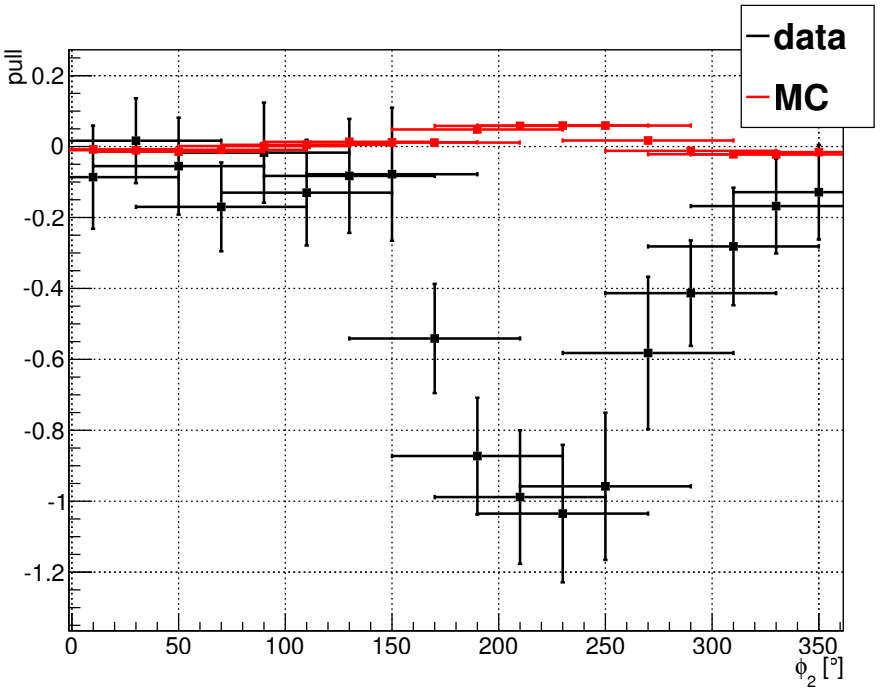

Figure 2.22: Running average of the pull $\frac{E_1-E_2}{\sqrt{\sigma^2_{E_1}+\sigma^2_{E_2}}}$ as a function of the angle ϕ for stereo events; the pull is used as the measure of the discrepancy between FD 1 and FD 2, where FD 1 is the station which measures the smaller Cherenkov fraction, to express it in units of standard deviations [55].

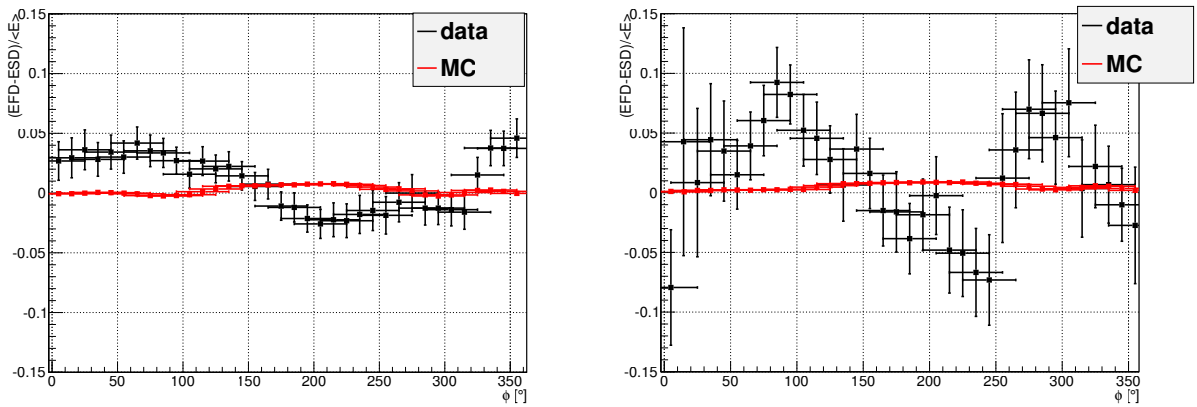

Figure 2.23: Running average of the relative energy difference $\frac{E_{\mathrm{FD}}-E_{\mathrm{SD}}}{\langle E\rangle}$ as a function of the angle ϕ from hybrid events, including predictions from Monte Carlo (MC) simulations; left: with so-called "golden" cuts, right: with an additional cut-off for energies below $10^{19.2}$ eV to show the more pronounced effect for large energies [55].

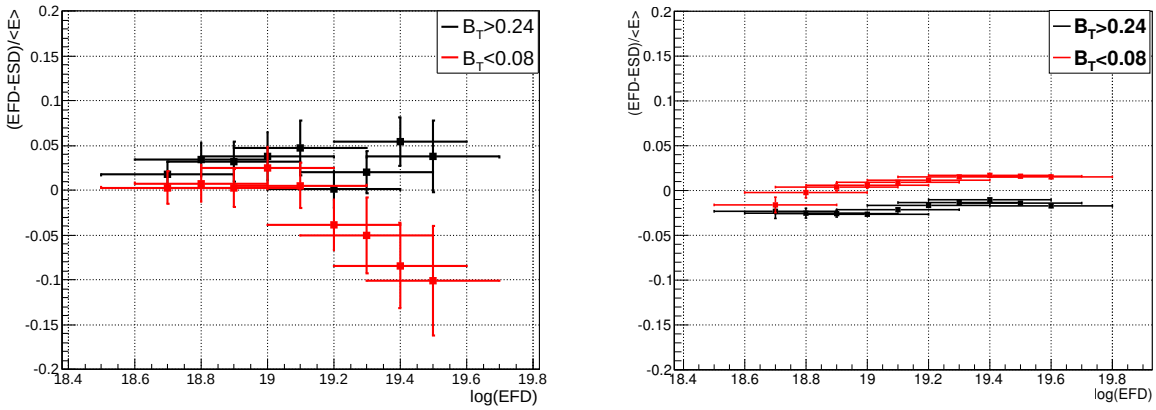

Figure 2.24: Running average of the relative energy difference $\frac{E_{\mathrm{FD}}-E_{\mathrm{SD}}}{\langle E\rangle}$ as a function the energy of the FD E_{FD} for different orientations with respect to the geomagnetic field (red: $B_{\mathrm{T}} < 0.08$, black: $B_{\mathrm{T}} > 0.24$); left: hybrid events, right: predictions from Monte Carlo (MC) simulations [55].

2.4 Super-preshowers

Given the observed muon excess in data compared to model predictions, and an apparent general trend of the composition of cosmic rays towards heavier nuclei, a possible solution of this composition puzzle could be to re-consider a substantial photon flux, and take new processes into account which might take place at highest energies but have not been considered in photon simulations so far. The decreasing X_{max} as well as $\sigma(X_{\mathrm{max}})$ for higher energies, as observed in figure 2.14, could also be explained by a substantial fraction of photons that undergo a preshower-like process as they approach Earth's atmosphere. On the one hand, photon initiated showers have small shower-to-shower fluctuations compared to hadronic showers, consistent with the data, and, on the other hand, we already saw in section 2.2.1 that the preshower causes a negative elongation rate for higher energy photons; however, the reduction of X_{max} for preshowers is not sufficient to reach the range of around $700 - 800$ g cm^{-2} observed in data. To achieve this reduction, the conversion of photons must take place at much higher altitudes, at least an order of magnitude higher, than typical preshowers. Such showers will, henceforth, be referred to as *super-preshowers*.

It is worth reiterating that a significant photon flux implies the validity of exotic production models, opening the door to the study of new physics with UHECRs. It should also be pointed out that top-down models diminish the need of point sources for photons, putting the lack of such sources into perspective.

Preliminary results from simulations by Homola [31] have shown that super-preshowers created at altitudes of $\sim$ 10000 km a.s.l. can mimic heavy or mixed hadronic compositions. When entering the atmosphere, the super-preshower will contain more than 1000 particles (see section 4.1.3) and have a substantially shallower shower maximum in the range of hadronic showers (see section 4.1.2).

In addition, the possible dependence on the magnetic field and energy of the energy reconstruction discrepancies as well as the dependence of the mass composition measurements using the rise time on the zenith angle is consistent with super-preshowers. Furthermore, differences in the energy spectra between the PAO and the TA are also expected for super-preshowers due different magnetic field conditions of the two experiments. The observed muon excess could be explained by a possible underestimation of the energies of air showers

induced by super-preshowers due to the fact that the showers develop well outside the visible range of the FDs and can undergo energy losses in this time that are not accounted for. In addition, the possibility of a higher photonuclear cross-section can also impact the muon production of super-preshowers. The extent to which the muon content is affected is worth studying of further.

However, the next course of action is to examine the possible processes which could be responsible for super-preshowers (see chapter 3, and to verify and to extend on the aforementioned preliminary results via simulations (see chapter 4).

Chapter 3

Super-preshower processes

This chapter will focus on possible processes that could lead to the development of super-preshowers. The important property of these processes is that they have to take place at significantly higher altitudes than the regular preshower, which is in the order of 1000 km a.s.l.. Three processes that come to mind are *photon splitting* in the geomagnetic field, *pair production* via interaction with solar photons, and interactions in the *radiation belts*. In this thesis, the first two processes have been prioritised and studied; they will be further motivated and investigated in the following.

3.1 Photon splitting

Photon splitting is a process, where a photon splits into two photons or more in the presence of a magnetic field, making it concurrent to pair production. It has historically mainly been studied in the context of pulsars which produce ultra-high magnetic fields in the order of the quantum critical field $B_{\text{cr}} = \frac{m^2 c^2}{e^2 \hbar} = 4.414 \cdot 10^{13}$ Gs and for low photon energies, often below the pair production threshold (low-frequency non-dispersive (strong-field) case), and has been shown to play a considerable role in this case [28]. However, for the scope of the PAO and of this thesis, the reverse scenario, i.e. high photon energies in the order of EeV and magnetic fields in the order of $\lesssim 1$ Gs are of interest, which has not been studied to any large extent, mainly due to the fact that photon splitting is a third order QED process, which is naively

thought to be dominated by pair production above the pair-production threshold (and weaker fields). Whether this holds true for ultra-high energy photons is not clear and is worth looking into.

Due to photon splitting being closely tied to photon dispersion (see section 3.1.1) [58], the expressions of splitting rates are immensely hard to evaluate; workable expressions only come up in the non-dispersive limit, although they, too, contain triple integrals and very long formulae (also, see section 3.1.1, as well as section 3.1.2). Simple expressions can only be found in the low-frequency limit, which is also a reason why this case has been studied in more detail in the past (also, see 3.1.1, as well as section 3.1.2). Nonetheless, the goal is to compute the probability of photon splitting for Auger conditions in order to estimate its contribution to possible super-preshowers, which requires the evaluation of more general cases. Given the extensiveness of the study of the low-frequency limit, its results serve well as a cross-check with which the calculations from the general cases can be verified. Therefore, it is prudent to set up the analysis of photon splitting the following way: First, a brief introduction to the theory of photon splitting will be given 3.1.1, firstly, to show the underlying mathematics behind photon splitting and the representations, methods and formalisms used to calculate its probability, and secondly, to derive said probability. Next, the non-dispersive, low-frequency case will be studied to verify existing results and to develop necessary tools for further analyses 3.1.2. Lastly, I will turn to more general cases, in particular the non-dispersive case with the photon energy below the pair-production threshold, and attempt to calculate the probability for photon splitting.

3.1.1 The theory of photon splitting

Photon splitting is a process which happens only in the presence of a magnetic field B. While it is kinematically possible for $B = 0$, it is forbidden due to *Furry's theorem*, a charge conjugation symmetry which states that Feynman diagrams containing a closed electron loop with an odd number of photon vertices are zero [25, 28]. As a result, this requires interactions with an external field; more precisely, only Feynman diagrams with an odd number of interactions (i.e. with an even number of vertices) contribute. In addition, photon splitting into more than two photons is strongly suppressed because the available phase space and scattering amplitude are vanishingly small [28, 58].

However, the method of calculating will not contain the approach of adding interactions with an external field; instead, the method used by Stoneham [58] will be employed, where the field-free electron propagator is replaced by the one in the ambient field, a representation of which was derived by Géhéniau [23] and Géhéniau and Demeur [24]. This replacement has the added benefit of taking photon dispersion into account [58]. The electron propagator in question is the "triangle" diagram (see figure 3.1), which corresponds to the quadratic vacuum polarisation tensor [58].

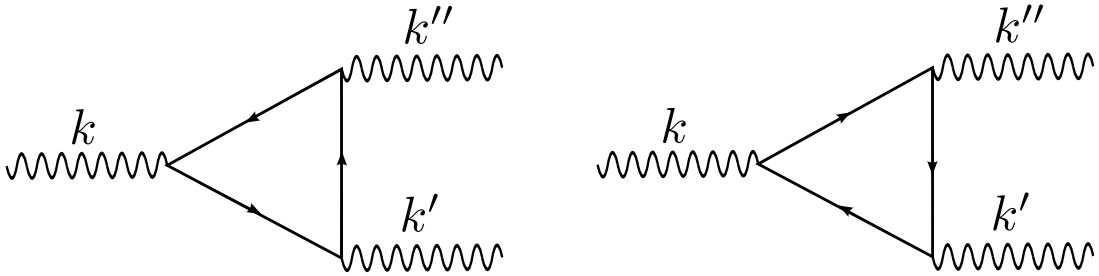

Figure 3.1: Feynman diagrams for a photon splitting into two photons in the lowest order in the fine structure constant α, but exact in the ambient field.

The formalism of relativistic quantum plasma physics is used to derive the probability of photon splitting which is exact in the frequency ω of the photon, its wavenumber k, and the magnetic field B; radiative corrections in the vacuum polarisation tensor are assumed to be negligible, which is justified for our purposes where the magnetic fields are (well) below the so-called *electrodynamic* or *quantum critical field* (see equation 3.1):

$$B_{\text{cr}} = \frac{m_{\text{e}}^2 c^2}{e \hbar} = 4.414 \cdot 10^{13} \text{ Gs}, \tag{3.1}$$

where m_{e} is the electron rest mass, c the speed of light in the vacuum, e is the elementary charge and $\hbar = \frac{h}{2\pi}$ is the reduced Planck constant. In the derivation, the following notations and units are used:

- Four-vectors will be represented as follows: $a^\mu = (a^0, \vec{a}) = (a^0, a^1, a^2, a^3)$, where $\vec{a}$ refers to the spatial three-vector and the metric tensor is $g^{\mu\nu} = \text{diag}(1, -1, -1, -1)$;
- $\perp$ and $\parallel$ refer to the perpendicular and parallel components of a four-vector, which can

be obtained through contraction with $g_{\perp}^{\mu\nu} = \text{diag}(0, -1, -1, 0)$ and $g_{\parallel}^{\mu\nu} = \text{diag}(1, 0, 0, -1)$, respectively;

- the electric charge of the electron is $-e$;
- unrationalised (i.e. Gaussian, where $e \to \sqrt{\alpha}$, with $\alpha = \frac{1}{4\pi\, c\, \epsilon_0}\, \frac{e^2}{\hbar} \approx \frac{1}{137}$ being the fine structure constant) natural ($\hbar = c = 1$) units will be used.

It is also worth showing how the unit Gs transforms into natural units (see equation 3.2):

$$\begin{aligned} 1\ \text{Gs} &= 1\ \sqrt{\frac{\text{g}}{\text{cm} \cdot \text{s}^2}} = 1\ \sqrt{\frac{5.60958616 \cdot 10^{32} \text{eV c}^{-2}}{5.06772886 \cdot 10^{4} \hbar\ \text{c eV}^{-1} \cdot (1.51926689 \cdot 10^{15} \hbar\ \text{eV}^{-1})^2}} \\ &= 6.925077738 \cdot 10^{-2}\ \text{eV}^2 (\text{c}\hbar)^{-3/2} \\ &= 6.925077738 \cdot 10^{-2}\ \text{eV}^2 \end{aligned} \tag{3.2}$$

As a result, the quantum critical field expressed in natural units is $B_{\text{cr}} = 3.0567 \cdot 10^{12}$ eV.

The one-dimensional integral representation of the electron propagator in a constant magnetic field $\vec{B}$ derived by Géhéniau [23] and Géhéniau and Demeur [24] from the space-time coordinate x^{μ} to x'^{μ} for $\vec{B}$ along the z- or 3-axis can be expressed as follows (see equations 3.3 to 3.5 [58]):

$$G(x, x') = \varphi(x, x')\, \Delta(x, x'), \tag{3.3}$$

with

$$\varphi(x, x') = \exp\left(-i\, e \int_{x}^{x'} dx_{\mu}\, A^{\mu} \right), \tag{3.4}$$

and

$$\Delta(x,x') = -\frac{e\,B}{16\,\pi^2}\int_0^\infty ds\,\frac{\exp(-i\,m_e^2\,s)}{s\cdot\sin(eBs)}\cdot\exp\left(-\frac{ieB\,(x^2)_\perp}{4\tan(eBs)}-\frac{i\,(x^2)_\parallel}{4s}\right) \times\left(\left[m_e+\frac{1}{2s}(\gamma\,x)_\parallel\right]\exp(-i\,\Sigma\,eBs)+\frac{eB}{2\sin(eBs)}(\gamma x)_\perp\right), \tag{3.5}$$

where A^μ is the four-potential of the ambient field, γ^μ refers to the Dirac γ-matrices and $\Sigma := i\gamma^1\,\gamma^2 = \mathrm{diag}(1,-1,1,-1)$. Note that the integration variable s is of dimension M^{-2} (M stands for mass, which is conventionally used as the dimension in natural units), as can easily be seen in the trigonometric and exponential functions. The (unsymmetrised) quadratic polarisation tensor in the presence of the ambient field results in (see equation 3.6):

$$\alpha_1^{\mu\,\nu\,\rho}(x,x',x'') = i\,e^3\,\mathrm{Tr}\left[\gamma^\mu\,G(x,x')\,\gamma^\nu\,G(x',x'')\,\gamma^\rho\,G(x'',x)\,\right]; \tag{3.6}$$

its Fourier transform is (see equation 3.7):

$$\alpha_1^{\mu\,\nu\,\rho}(k,k',k'') = \int d^4x\int d^4x'\ \exp(ikx-ik'x')\,\alpha_1^{\mu\,\nu\,\rho}(x,x',x''), \tag{3.7}$$

where $k_\mu = k'_\mu + k''_\mu$. The symmetrised vacuum polarisation tensor is (see equation 3.8):

$$\alpha^{\mu\,\nu\,\rho}(k,k',k'') = \frac{1}{2}\left[\alpha_1^{\mu\,\nu\,\rho}(k,k',k'')+\alpha_1^{\mu\,\rho\,\nu}(k,k'',k')\right]. \tag{3.8}$$

The scattering amplitude $\mathcal{M}$ for a photon in the mode σ to split into two photons of mode σ' and σ'' can be obtained via a relativistic quantum theory for processes in collisionless plasmas derived by Melrose [41], and amounts to (see equation 3.9 [58]):

$$\mathcal{M}(\sigma\to\sigma'+\sigma'') = 2\,(4\pi)^{3/2}\,e_\mu^\sigma(\vec{k})\,e_\nu^{\sigma''*}(\vec{k'})\,e_\rho^{\sigma''*}(\vec{k''})\;\alpha^{\mu\,\nu\,\rho}(k,k',k''), \tag{3.9}$$

where $e_\mu^\sigma(\vec{k})$ is the polarisation 4-vector of a photon in mode σ, which is either perpendicular or parallel to the plane formed by its wave vector $\vec{k}$ and the magnetic field $\vec{B}$, and * refers to

complex conjugation. Having the expression for the scattering amplitude, we can write down the probability w of photon splitting with the modes $\sigma \to \sigma' + \sigma''$, where the final photons are in the ranges $d^3k'/(2\pi)^3$ and $d^3k''/(2\pi)^3$ (see equation 3.10):

$$w_\sigma^{\sigma'\sigma''}(\vec{k},\vec{k'},\vec{k''}) = \frac{R_{\mathrm{E}}^{\sigma}(\vec{k})\, R_{\mathrm{E}}^{\sigma'}(\vec{k'})\, R_{\mathrm{E}}^{\sigma''}(\vec{k''})}{|\omega^{\sigma}(\vec{k})\, \omega^{\sigma'}(\vec{k'})\, \omega^{\sigma''}(\vec{k''})|}\, |\mathcal{M}(\sigma \to \sigma' + \sigma'')|^2\, (2\pi)^4\, \delta^{(4)}(k - k' - k''), \quad (3.10)$$

where $R_{\mathrm{E}}^{\sigma}(\vec{k})$ alludes to the ratio of electric to total photon energy in the mode σ. The absorption coefficient κ is obtained via integration of the probability over all final photon energies (see equation 3.11):

$$\kappa_\sigma^{\sigma'\sigma''}(\vec{k},\vec{k'},\vec{k''}) = \frac{1}{2} \int \frac{d^3k'}{(2\pi)^3} \int \frac{d^3k''}{(2\pi)^3}\, w_\sigma^{\sigma'\sigma''}(\vec{k},\vec{k'},\vec{k''}). \quad (3.11)$$

It is not feasible in the scope of this thesis to evaluate the general forms of the scattering amplitude, probability, and absorption coefficient of photon splitting in equations 3.9 to 3.11 as this requires large amounts of tedious calculations, though there are more explicit − yet not necessarily simpler − expressions to be found in Stoneham [58]. Not only for this reason, but also due to the fact that photon dispersion is small in weak magnetic fields [13], is it useful to turn to the non-dispersive case, for which equations 3.10 and 3.11 can be simplified significantly (see equations 3.12 and 3.13 [58]):

$$w_\sigma^{\sigma'\sigma''}(\vec{k},\vec{k'},\vec{k''}) = \frac{|\mathcal{M}(\sigma \to \sigma' + \sigma'')|^2}{8\omega\omega'\omega''}\, (2\pi)^4\, \delta^{(4)}(k - k' - k''), \quad (3.12)$$

$$\kappa_\sigma^{\sigma'\sigma''}(\vec{k},\vec{k'},\vec{k''}) = \frac{1}{32\pi\omega^2} \int_0^\omega d\omega' \int_0^\omega d\omega''\, \delta(\omega - \omega' - \omega'')\, |\mathcal{M}(\sigma \to \sigma' + \sigma'')|^2. \quad (3.13)$$

The scattering amplitude $\mathcal{M}$ (see equation 3.9) reduces to the following expression (see equations 3.14 to 3.17 [58]):

$$
\begin{aligned}
\mathcal{M} &= \frac{ie^4B}{\pi^{1/2}} \int_0^\infty ds \int_0^s dt \int_0^t du\, \tilde{M}(s,t(s),u(t(s))) \\
\tilde{M} &= f(s)\cdot D^\dagger(\sigma \to \sigma' + \sigma'')\cdot \exp\{g(s,t,u)\}, \quad f(s) = \frac{e^{-m^2 s}}{s^3 \sinh^4(eBs)}, \\
g(s,t,u) &= \left(\frac{u(s-t)}{s} - \frac{\sinh(eBu)\sinh(eB(s\text{-}t))\cosh(eB(t\text{-}u))}{eB\sinh(eBs)}\right)\omega^2 \\
&+ \left(\frac{u(t\text{-}u)}{s} - \frac{\sinh(eBu)\sinh(eB(t\text{-}u))\cosh(eB(s\text{-}t))}{eB\sinh(eBs)}\right)\omega'^2 \\
&+ \left(\frac{(t\text{-}u)(s\text{-}t)}{s} - \frac{\sinh(eB(t\text{-}u))\sinh(eB(s\text{-}t))\cosh(eBu)}{eB\sinh(eBs)}\right)\omega''^2,
\end{aligned}
\tag{3.14}
$$

with

$$
\begin{aligned}
D^\dagger((\perp) \to (\parallel)' + (\parallel)'') &= D_1^\dagger(\omega,\omega',\omega'';s,t,u) \\
D^\dagger((\parallel) \to (\perp)' + (\parallel)'') &= D_1^\dagger(-\omega',\omega'',-\omega;s,s\text{-}u,t\text{-}u) \\
D^\dagger((\parallel) \to (\parallel)' + (\parallel)'') &= D_1^\dagger(-\omega'',-\omega,\omega';s,s\text{-}t+u,s\text{-}t) \\
D^\dagger((\perp) \to (\perp)' + (\perp)'') &= D_2^\dagger(\omega,\omega',\omega'';s,t,u) \\
D^\dagger(\sigma \to \sigma' + \sigma'') &= 0, \text{ otherwise},
\end{aligned}
\tag{3.15}
$$

and

$$
\begin{aligned}
&D_1^{\dagger}(\omega,\omega',\omega'';s,t,u) = \\
&\quad 4m_{\mathrm{e}}^2 s^2 \mathrm{sh}^2(eBs)\{\omega' \mathrm{sh}^2(eB(s\text{-}u)) + \omega'' \mathrm{sh}^2(eBt)\} \\
&-4s\,\mathrm{sh}^2(eBs)\{\omega' \mathrm{sh}^2(eBu) + \omega'' \mathrm{sh}^2(eB(s\text{-}t))\} \\
&-8eBs^2 \mathrm{sh}(eBs)\{\omega' \mathrm{sh}(eB(s\text{-}u))\,\mathrm{sh}(eBu) + \omega'' \mathrm{sh}(eBt)\,\mathrm{sh}(eB(s\text{-}t))\} \\
&+4\mathrm{sh}^2(eBs)\{-\mathrm{sh}^2(eB(s\text{-}u))(u\omega' - (s\text{-}t)\omega'')(u\omega' + t\omega'')\omega' \\
&\qquad\qquad + \mathrm{sh}^2(eBt)(u\omega' - (s\text{-}t)\omega'')\,((s\text{-}u)\omega' + (s\text{-}t)\omega'')\omega'' \\
&\qquad\qquad - \omega'\omega'' s(\,\mathrm{sh}^2(eBu)\,((s\text{-}u)\omega' - (s\text{-}t)\omega'') + \mathrm{sh}^2(eB(s\text{-}t))\,(u\omega' + t\omega'')\,)\} \\
&+4s^2\{\omega'^3 \mathrm{sh}^2(eB(s\text{-}u))\,\mathrm{sh}^2(eBu) + \omega''^3 \mathrm{sh}^2(eB(s\text{-}t))\,\mathrm{sh}^2(eBt) \\
&\qquad + \omega'^2\omega'' \mathrm{sh}(eB(s\text{-}t))\,\mathrm{sh}(eBu)\,[\,2\mathrm{sh}(eB(s\text{-}t)) + \mathrm{sh}(eB(t+s\text{-}2u))\,] \\
&\qquad + \omega'\omega'' \mathrm{sh}(eBu)\,\mathrm{sh}(eB(s\text{-}t))\,(2\mathrm{sh}(eBu) + \mathrm{sh}(eB(2t\text{-}u))\},
\end{aligned}
\tag{3.16}
$$

$$
\begin{aligned}
&D_2^{\dagger}(\omega,\omega',\omega'';s,t,u) = \\
&-4\mathrm{sh}^2(eBs)\{m_{\mathrm{e}}^2 s^2 + s - (u\omega' - (s\text{-}t)\omega'')(u\omega' + t\omega'')\} \\
&\quad \{\mathrm{sh}(eB(s\text{-}u))\,\mathrm{sh}(eB(2t\text{-}u-s))\omega' \\
&\qquad + \frac{1}{2}[\,\mathrm{ch}(2eB(t\text{-}u)) - \mathrm{ch}^2(eB(2t\text{-}u\text{-}s)) - \mathrm{sh}^2(eB(2t\text{-}u\text{-}s))\,]\omega''\} \\
&-4\mathrm{sh}^2(eBs)\{m^2 s^2 + s + (u\omega' + t\omega'')((s\text{-}u)\omega' + (s\text{-}t)\omega'')\} \\
&\quad \{\frac{1}{2}[\,\mathrm{ch}(2eB(s\text{-}t)) - \mathrm{ch}^2(eB(s\text{-}t\text{-}u)) - \mathrm{sh}^2(eB(s\text{-}t\text{-}u))\,]\omega' \\
&\qquad + \frac{1}{2}[\,\mathrm{ch}(2eBu) - \mathrm{ch}^2(eB(s\text{-}t\text{-}u)) - \mathrm{sh}^2(eB(s\text{-}t\text{-}u))\,]\omega''\} \\
&-4\mathrm{sh}^2(eBs)\{m^2 s^2 + s + ((s\text{-}u)\omega' + (s\text{-}t)\omega'')(u\omega' - (s\text{-}t)\omega'')\} \\
&\quad \{\frac{1}{2}[\,\mathrm{ch}(2eB(t\text{-}u)) - \mathrm{ch}^2(eB(t\text{-}2u)) - \mathrm{sh}^2(eB(t\text{-}2u))\,]\omega' + \mathrm{sh}(eBt)\,\mathrm{sh}(eB(t\text{-}2u))\omega''\} \\
&+4s^2\{\mathrm{sh}^2(eBu)\,\mathrm{sh}(eB(s\text{-}u))\mathrm{sh}(eB(2t\text{-}s\text{-}u))\omega'^3 + \mathrm{sh}^2(eB(s\text{-}t))\,\mathrm{sh}(eBt)\,\mathrm{sh}(eB(t\text{-}2u))\omega''^3 \\
&\qquad - [\,\mathrm{sh}^2(eBu)\,\mathrm{sh}^2(eB(s\text{-}t)) + 2\mathrm{sh}(eBu)\,\mathrm{sh}(eB(s\text{-}t))\,\mathrm{sh}(eBt)\,\mathrm{sh}(eB(s\text{-}u))\,]\omega\omega'\omega''\},
\end{aligned}
\tag{3.17}
$$

where sh $\equiv$ sinh and ch $\equiv$ cosh are used as abbreviations to shorten the expressions and make them more overseeable. Equation 3.14 holds for photon energies below the pair production threshold $2m_{\mathrm{e}}$ [58].

In the low-frequency (non-dispersive) limit, which was defined by Harding et al. [28] as follows (see equation 3.18 :

$$\frac{\omega}{m_{\rm e}} \cdot B' \cdot \sin\theta \lesssim 1, \tag{3.18}$$

with $B' = \frac{B}{B_{\rm cr}}$ and θ being the angle between the propagation direction of the photon and $\vec{B}$; it can be set to $\theta = 180°$ for the scope of this thesis as we are, primarily, only interested in order-of-magnitude estimates of the probability. Equation 3.14 simplifies to (see equations 3.19 to 3.20):

$$\begin{aligned}
\mathcal{M}[(\perp) \to (\parallel)' + (\parallel)''] &= \mathcal{M}[(\parallel) \to (\perp)' + (\parallel)'' = \mathcal{M}[(\parallel) \to (\parallel)' + (\perp)''] \\
&= -\frac{4\,i\,\alpha^3\,B^3}{\pi^{1/2}} \frac{\omega\,\omega'\,\omega''}{m_{\rm e}^8}\ \sin^3\theta\, M_1(B), \\
\mathcal{M}[(\perp) \to (\perp)' + (\perp)''] &= -\frac{4\,i\,\alpha^3\,B^3}{\pi^{1/2}} \frac{\omega\,\omega'\,\omega''}{m_{\rm e}^8}\ \sin^3\theta\, M_2(B), \\
\mathcal{M}[(\sigma \to \sigma' + \sigma'')] &= 0, \text{ otherwise},
\end{aligned} \tag{3.19}$$

where

$$\begin{aligned}
\mathcal{M}_1(B) &= \frac{1}{B'^4} \int_0^\infty \frac{ds}{s}\ e^{-s/B'} \left[\left(-\frac{3}{4s} + \frac{s}{6} \right) \coth s + \frac{3+2s^2}{12} \mathrm{csch}^2 s - \frac{s}{2} \coth s\, \mathrm{csch}^2 s \right], \\
\mathcal{M}_2(B) &= \frac{1}{B'^4} \int_0^\infty \frac{ds}{s}\ e^{-s/B'} \left[-\frac{3}{4s} \coth s + \frac{3+4s^2}{4} \mathrm{csch}^2 s - \frac{3s^2}{2} \mathrm{csch}^4 s \right].
\end{aligned} \tag{3.20}$$

The absorption coefficients change accordingly (see equation 3.21):

$$\begin{aligned}
\kappa[(\perp) \to (\parallel)' + (\parallel)''] = \kappa[(\parallel) \to (\perp)' + (\parallel)'' = \kappa[(\parallel) \to (\parallel)' + (\perp)''] \\
= \frac{\alpha^3}{60\pi^2} \cdot (B' \sin\theta)^6 \cdot \left(\frac{\omega}{m_\mathrm{e}}\right)^5 \cdot M_1^2(B), \\
\kappa[(\perp) \to (\perp)' + (\perp)''] = \frac{\alpha^3}{60\pi^2} \cdot (B' \sin\theta)^6 \cdot \left(\frac{\omega}{m_\mathrm{e}}\right)^5 \cdot M_2^2(B), \\
\kappa(\sigma \to \sigma' + \sigma'')] = 0, \text{ otherwise.}
\end{aligned} \tag{3.21}$$

In Harding et al. [28], the attenuation coefficient (averaged over all photon polarisations) is also derived from the above expressions (see equation 3.22):

$$T_{\mathrm{sp}}(\omega) = \frac{\alpha^3}{10\pi^2} \frac{1}{\lambda} \left(\frac{19}{315}\right)^2 \cdot (B' \sin\theta)^6 \cdot \left(\frac{\omega}{m_\mathrm{e}}\right)^5 \cdot \mathcal{C}(B), \tag{3.22}$$

where $\mathcal{C}(B) = \frac{1}{12}\left(\frac{315}{19}\right)^2 \cdot (3\,M_1^2(B) + M_2^2(B))$. In the weak-field limit ($B' \ll 1$), which is particularly relevant for the Pierre Auger Observatory, where $B = \mathcal{O}(1\text{ Gs})$, $M_1(B)$ and $M_2(B)$ reduce to (see equation 3.23):

$$B' \ll 1 : \mathcal{M}_1 \approx \frac{26}{315}\,,\ \mathcal{M}_2 \approx \frac{48}{315},\ \text{and}\ \ \mathcal{C}(B) \approx 1 \tag{3.23}$$

Now that all relevant equations have been derived, we can proceed to calculate the probability of photon splitting. I will start with the simplest case, i.e. the non-dispersive low-frequency case, where I will verify the results for the scattering amplitudes from Harding et al. [28] (see equations 3.19, 3.20 and 3.23); with this done, I will compute the attenuation coefficients for the Auger ω-B-phase space within this limit. In the next step, I will attempt to verify the expression for the non-dispersive case, where $\omega \leq 2\,m_\mathrm{e}$ by calculating the scattering amplitudes (see equations 3.13 to 3.17) in the low-frequency case. The further course of action would be to calculate scattering amplitudes for photon energies up to the pair-production threshold, and cross-check the results with those of more general cases; this was, unfortunately, not done in

this thesis, as the more general case could not be verified due to a lack of convergence with literature values.

3.1.2 Calculating the probability of photon splitting

In the following section, I will outline my course of action in computing the probability of photon splitting. As noted in the end of section 3.1.1, I will proceed by going from the simplest (most special) to the most complex (most general) expressions, in order to be able to cross-check the results of the latter with those of the former. It is worth noting that all programs were written in *C++*. This section will also mention obstacles I came across during my analysis and the solutions I found as finding them took up a significant portion of the time spent on the analysis, on the one hand, and as they could prove useful for those who wish to pursue the analysis of photon splitting, on the other.

Non-dispersive, low-frequency case

Equations 3.19 to 3.23 derived in section 3.1.1 provide the mathematical framework for describing the non-dispersive, low-frequency case. As shown in equation 3.23, the scattering amplitude coefficients $M_1(B)$ and $M_2(B)$ tend towards simple numerical values in the weak-field limit. This limit, therefore, serves as good starting point for checking the accuracy of the programs implemented to calculate the photon splitting probability. For this, I computed the scattering amplitude coefficients for weak fields, and compared the results with the limits given in the aforementioned equation. In addition, my goal was to control the precision of the calculation. Given that the equations in 3.20 constitute one-dimensional improper integrals (i.e. the upper integration limit tends towards infinity) which cannot be solved analytically, there are two constraints on the precision given from the start: Firstly, the number of sampling points n in the numerical integration and, secondly, the choice of the cut-off point of the upper integration limit s_{cut}. The latter parameter depends on the functional form of the integrand $\tilde{M}_{\text{i}}$, $i = 1, 2$ as its contribution to the integral for $s > s_{\text{cutoff}}$ should, ideally, be vanishingly small.

However, when plotting the integrand, it did not behave as expected; while it converges for

large values of the integration variable s, for $s \to 0$, the integrand diverges, especially for smaller values of B'. Apparently, the precision of the calculation using *double* floating point types (which ranges from $1.79769313486232 \cdot 10^{308}$ to $2.22507385850720 \cdot 10^{-308}$ and the precision of the mantissa is 15 digits) is insufficient. With the goal to be able to control the precision, I used *MPFR*, a *GNU* library which allows numbers to be expressed and computed with arbitrary precision [60]. With an increased precision, the problem of the divergence for $s \to 0$ could, in fact, be solved. I plotted $\tilde{M}_1$ and $\tilde{M}_2$ for $B' = 0.01$ and set the number of digits in the mantissa to 100 to illustrate this fact (see figure 3.2).

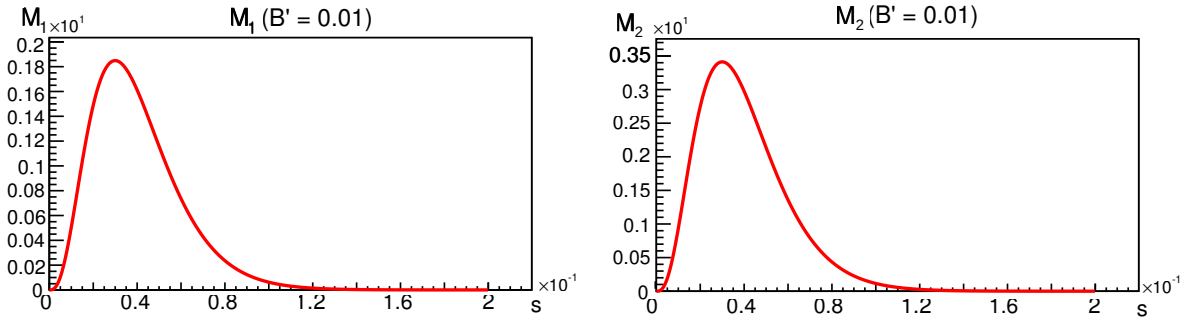

Figure 3.2: The integrand $\tilde{M}_i$ for $B' = 0.01$, calculated with *MPFR* precision with 100 digits (top: $i = 1$; bottom: $i = 2$).

It is also important, however, to identify the functions responsible for the divergent behaviour when calculating with *double* precision. For this, I split up the integrand into two parts, one dominated by the exponential, and one by the hyperbolic functions:

$$\begin{aligned}
&\tilde{M}_1(B) = e_1(s) \cdot h_1(s), \quad \tilde{M}_2(B) = e_2(s) \cdot h_2(s), \\
&e_1(s) = e_2(s) := \frac{1}{B'^4} \cdot \frac{e^{-s/B'}}{s}, \\
&h_1(s) := \left[\left(-\frac{3}{4s} + \frac{s}{6} \right) \coth s + \frac{3 + 2s^2}{12} \operatorname{csch}^2 s - \frac{s}{2} \coth s \operatorname{csch}^2 s \right], \\
&h_2(s) := \left[-\frac{3}{4s} \coth s + \frac{3 + 4s^2}{4} \operatorname{csch}^2 s - \frac{3s^2}{2} \operatorname{csch}^4 s \right].
\end{aligned} \tag{3.24}$$

I plotted both of these functions, $e_1 = e_2$ for $B' = 0.01$ (see figure 3.3), and h_1 and h_2 for different ranges of s (see figure 3.4).

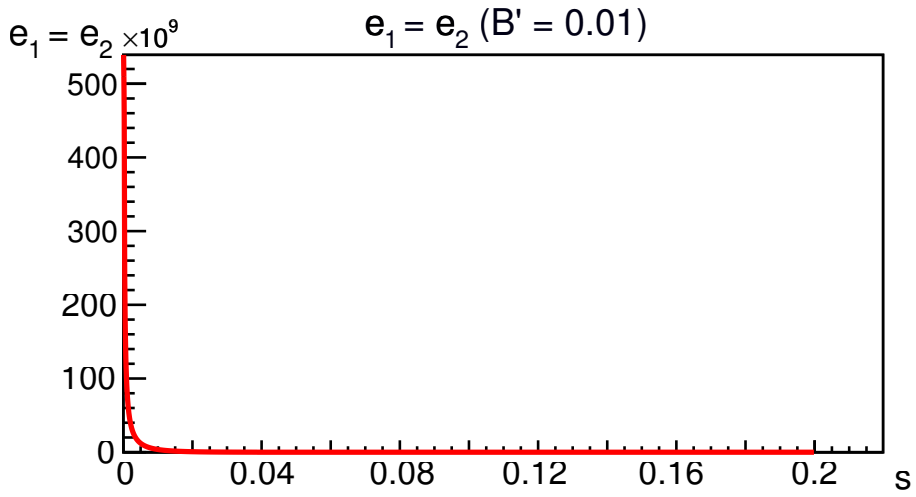

Figure 3.3: The exponential part of $\tilde{M}_{\mathrm{i}}$, e_{i}, for $B' = 0.01$, calculated with *double* precision.

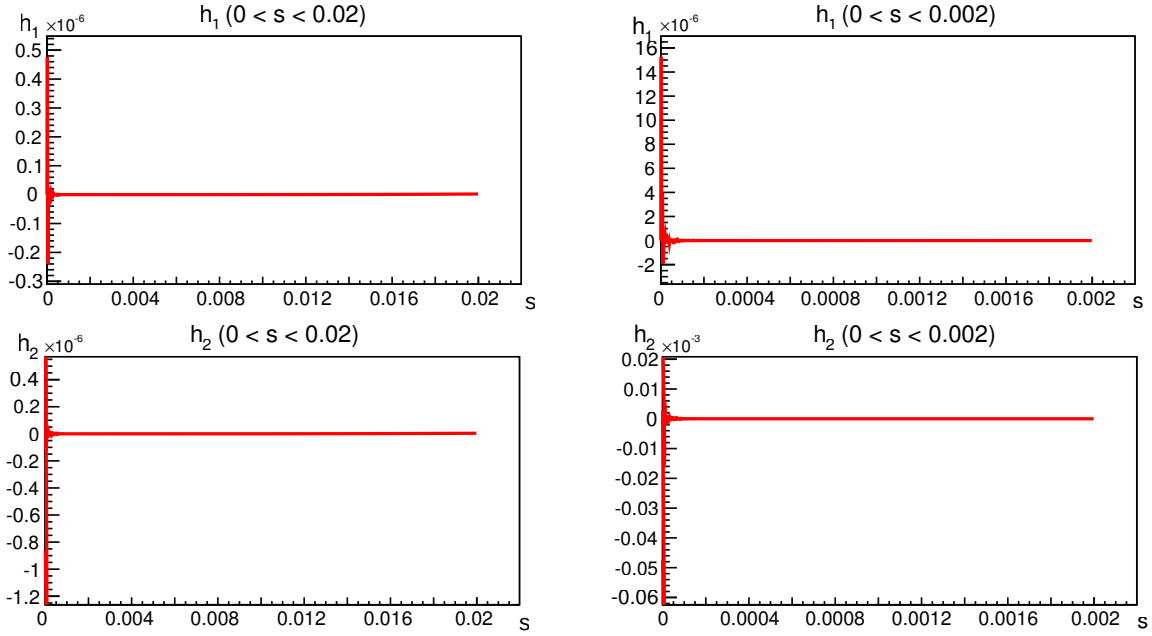

Figure 3.4: The hyperbolic function h_1 of $\tilde{M}_1$ for different ranges of s as indicated above each graph, calculated with *double* precision.

As expected due to the factor $\frac{1}{s}$, the exponential functions e_1 and e_2 diverge for $s \to 0$ (I only used one value of B' to illustrate this trend as all other values of B' showed the same result); the hyperbolic functions h_1 and h_2, however, behave differently: First, they appear

to tend towards zero, as is required for the integrability of $\tilde{M}_{\mathrm{i}}$, but for a decreasing range of s, they start to diverge. Apparently, the double precision fails to adequately calculate the hyperbolic functions for very small values of s. When looking closer at each term in both hyperbolic functions, one sees that none of them individually tends towards zero (in fact, they all diverge; see expansion (Laurent series) of each term in equations 3.25 and 3.26):

$$\begin{aligned}\left(-\frac{3}{4s}+\frac{s}{6}\right)\coth s &\approx -\frac{3}{4s^2}-\frac{1}{12}+\frac{13s^2}{180}+\mathcal{O}(s^4),\\ \frac{3+2s^2}{12}\mathrm{csch}^2 s &\approx \frac{1}{4s^2}+\frac{1}{12}-\frac{7s^2}{180}+\mathcal{O}(s^4),\\ \frac{s}{2}\coth s\,\mathrm{csch}^2 s &\approx \frac{1}{2s^2}-\frac{s^2}{30}+\mathcal{O}(s^4).\end{aligned} \tag{3.25}$$

$$\begin{aligned}\frac{3}{4s}\coth x &\approx \frac{3}{4s^2}+\frac{1}{4}-\frac{s^2}{60}+\mathcal{O}(s^4),\\ \frac{3+4s^2}{4}\mathrm{csch}^2 x &\approx \frac{3}{4s^2}-\frac{5}{4}-\frac{23s^2}{60}+\mathcal{O}(s^4),\\ \frac{3}{2}s^2\mathrm{csch}^4 s &\approx \frac{3}{2s^2}-1+\frac{11s^2}{30}+\mathcal{O}(s^4).\end{aligned} \tag{3.26}$$

Rather, they cancel each other out by subtraction for $s \to 0$. This constitutes the underlying reason for the "chaotic" divergent behaviour of h_1 and h_2 in said limit; each term in the function is only calculated with a certain precision (the number of digits in the mantissa), and, therefore, any rounding errors leading to non-zero values as they are subtracted from one another will be magnified as they diverge. Avoiding rounding errors by calculating with higher precision (i.e. with more digits) is evidently necessary for the hyperbolic function and, ultimately, the integrand to behave as expected.

However, given that the greater precision also comes with longer computation times, it is important to find the optimal (i.e. minimal) number of digits with which the numbers are rounded for acquiring a result in a given precision. For this, I looked at the hyperbolic functions sinh, cosh and tanh, and determined the largest value of $s > 0$ as a function of the number of digits for which the functions are rounded to their expected value for $s = 0$; this gives us direct

insight into the precision with which the program is able to calculate the given functions (see figure 3.5).

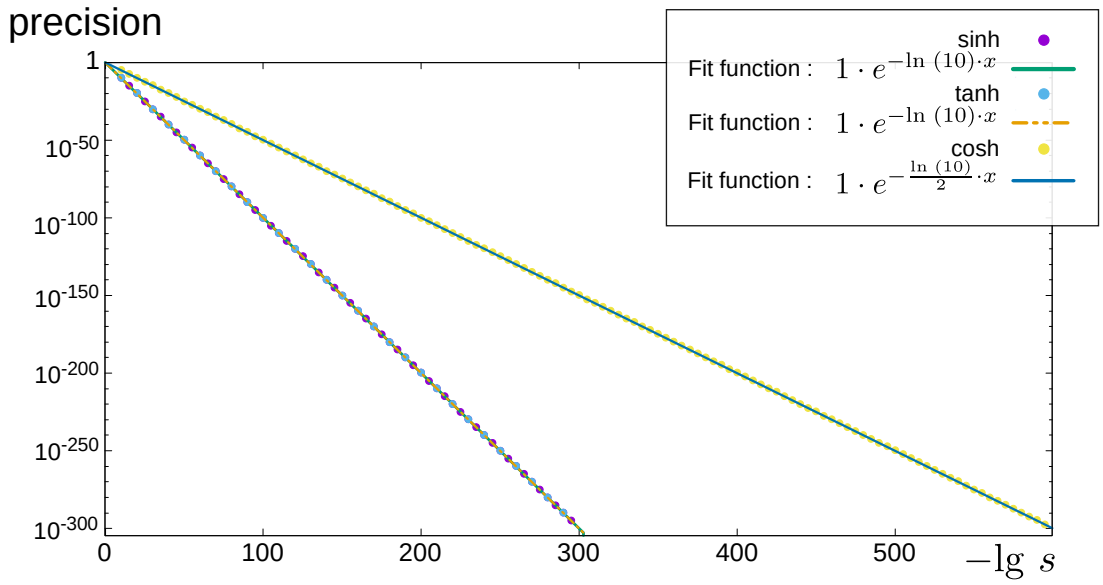

Figure 3.5: Precision with which hyperbolic functions are computed as a function of the number of digits with which they are calculated/rounded.

As can be seen from the exponential fit[1] $f(x) = a \cdot \exp(-b \cdot x)$ to the points, the values of s at which the program numerically rounds sinh and tanh as zero, decreases exponentially, with $a = 1$ and $b = 2.30259 \approx \log 10$; similarly, cosh is rounded to 1 at an exponential rate with $a = 1$ and $b = 1.15129 \approx \frac{\log 10}{2}$. One needs twice as many digits to calculate cosh with the same precision as sinh and tanh for small s. When looking at the Laurent expansion of these functions around $s = 0$:

$$\begin{aligned} \sinh s &\approx s + \mathcal{O}(s^3), \\ \tanh s &\approx s + \mathcal{O}(s^3), \\ \cosh s \ - 1 &\approx s^2 + \mathcal{O}(s^4), \end{aligned} \tag{3.27}$$

the results of the fit are perfectly in line with power of the leading order. With this knowledge,

[1]Although I am speaking of "fits", the uncertainty or the goodness of the fit in not of great interest for the scope of my analysis; rather, the fits seek to illustrate a trend which is discernible.

one can predict the required number of digits for calculating the hyperbolic functions h_1 and h_2; as the numerators of the terms, at most, contain the factor of cosh, this factor should drive the precision of the calculation. To check this, I plotted the value of s at which the function h_2 starts to diverge as a function of the number of digits, and fitted the same exponential to the points as for the previous hyperbolic function (see figure 3.6); h_1 can be assumed to behave just as h_2.

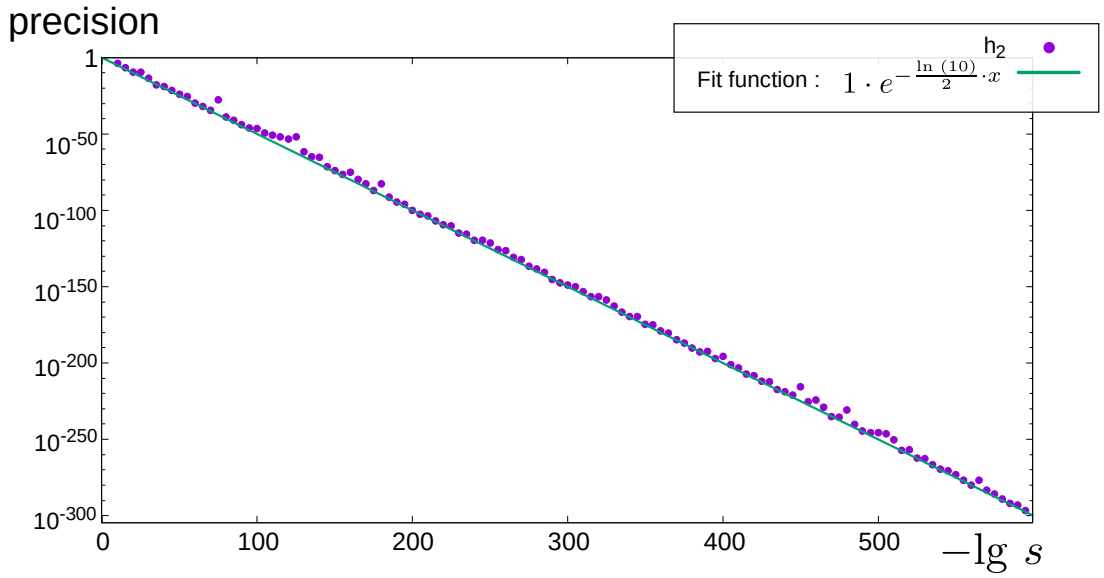

Figure 3.6: Precision with which hyperbolic function h_2 is computed as a function of the number of digits with which it is calculated.

The fit parameters $a = 1$ and $b = 1.15129 \approx \frac{\log 10}{2}$ are the same as for cosh, as predicted.

From figure 3.6, one can derive the optimal number of digits for a certain required precision of calculation. Now it is possible to study the dependence of the calculation time on the precision; for this, I measured the calculation time of 10^5 computations of $h_2(s)$ for different precisions and plotted it as a function of the optimal number of digits, and I fitted a polynomial $f(x) = a \cdot x^b + c$ to the data. I repeated this plot for sinh, tanh and cosh to see which of them contributes most to the computation time for h_1 and h_2 (see figures 3.7 and 3.8).

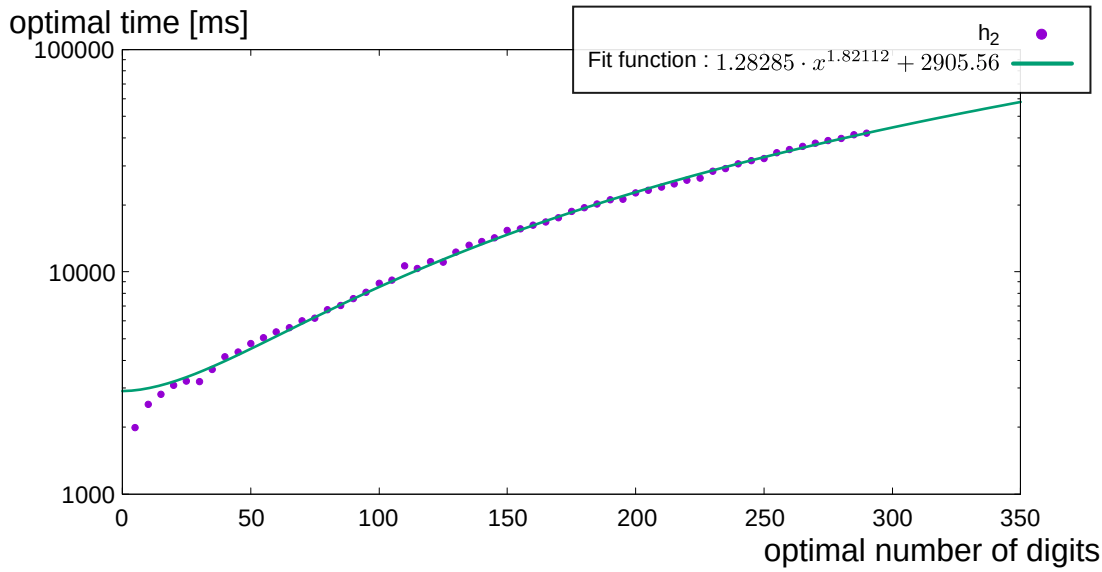

Figure 3.7: Computation time with rising precision for the optimal number of digits for the hyperbolic function h_2 which are indicated in the legend.

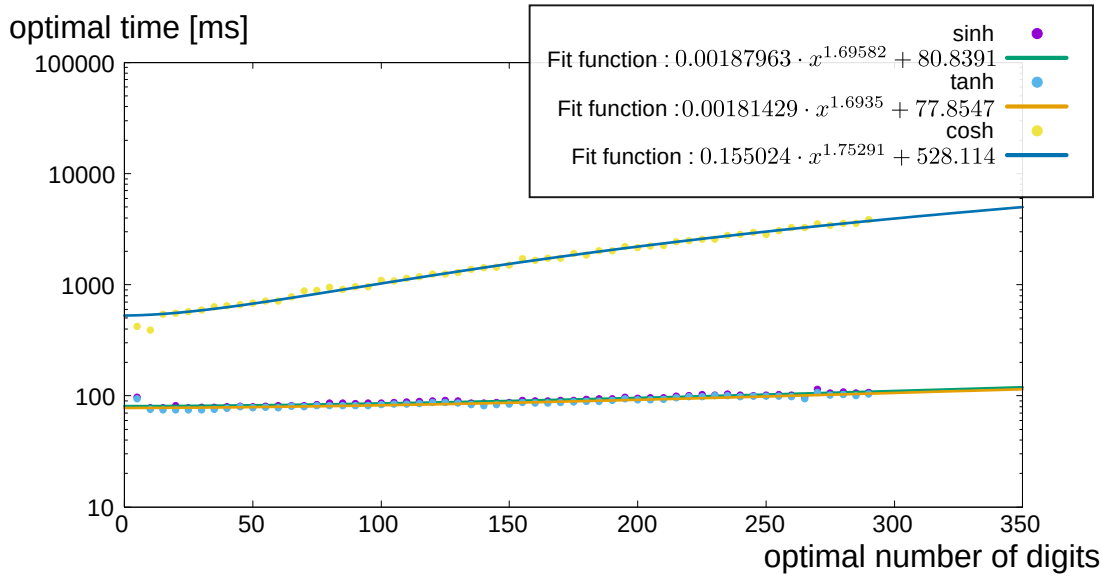

Figure 3.8: Computation time with rising precision for the optimal number of digits for individual hyperbolic functions which are indicated in the legend.

While the minimum computation time is only ~ 6 times higher for cosh ($c = 528.114$) than for sinh ($c = 80.8391$) and tanh ($c = 77.8547$) and the power of s is only slightly larger ($b = 1.75291$ for cosh versus $b = 1.69582$ for sinh and $b = 1.6935$ for tanh), the pre-factor

a is almost 2 orders of magnitude larger ($a = 0.155024$ for cosh versus $a = 0.00187963$ for sinh and $a = 0.00181429$ for tanh), and thereby, the computation of cosh is ~ 1 order of magnitude larger than for the other two functions. The trend of h_2 is even steeper than for the individual hyperbolic functions, with the pre-factor being another order of magnitude larger ($a = 1.28285$); the exponent is not significantly higher ($b = 1.82112$) and the minimum computation time is only about 6 times higher than for cosh ($c = 2905.56$). While cosh does appear to contribute most to the computation time, its computation time is ~ 1 order of magnitude smaller than for h_2 for the same precision; this is to be expected, as h_2 contains several functions which have to computed individually.

Having investigated the effects of the number of digits to which numbers are rounded in the mantissa on the precision of the calculations, and being able to control this precision, one can turn to the evaluation of the integrals. As mentioned before, numerically integrating $\tilde{M}_1$ and $\tilde{M}_2$ requires a cut-off of the upper integration limit s_{cut} and a finite number of sampling points n. As can be seen in figure 3.2, the integrands converge quickly for increasing s, which allows us to set the cut-off rather low and improves the precision for a fixed number of sampling points n. In addition, the figures appear to indicate that the "width" of the integrands (i.e. the distance in s to the point of its maximum) decreases linearly with B', at least for $B' \ll 1$ (the interesting region in the scope of this thesis), which allows us to express a (preliminary) dependence of the cut-off point on B' (see equation 3.28):

$$s_{\text{cut}}(B) = \frac{B'_0}{B} \cdot s_{\text{cut}}(B'_0), \tag{3.28}$$

where B'_0 is some starting value of B' for which a suitable cut-off point $s_{\text{cut}}(B'_0)$ has been determined. To find this suitable cut-off point, I plotted the integrand for different values of $B' \ll 1$ and fitted an exponential $f(x) = a \cdot \exp(-b \cdot x)$ to its tail (the integrand is quickly dominated the exponential function e_{i} for $B' \ll 1$; see figures 3.9 to 3.11).

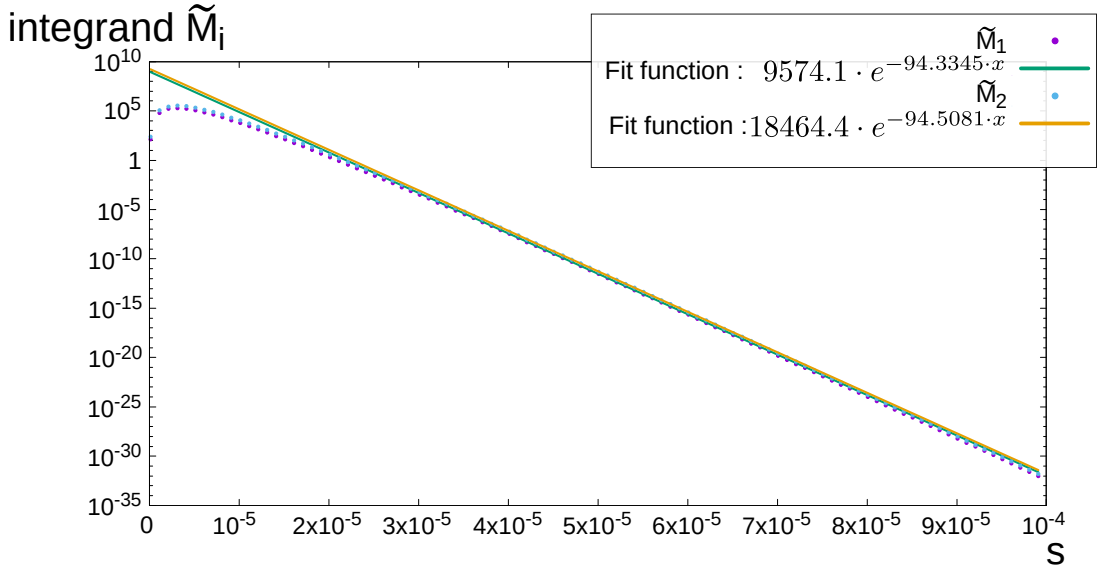

Figure 3.9: Plot of M_1 and M_2 from $s = 0$ to $s = 1$ for $B' = 0.01$ with an exponential fitted to the tail (from $s = 0.5$ to $s = 1$).

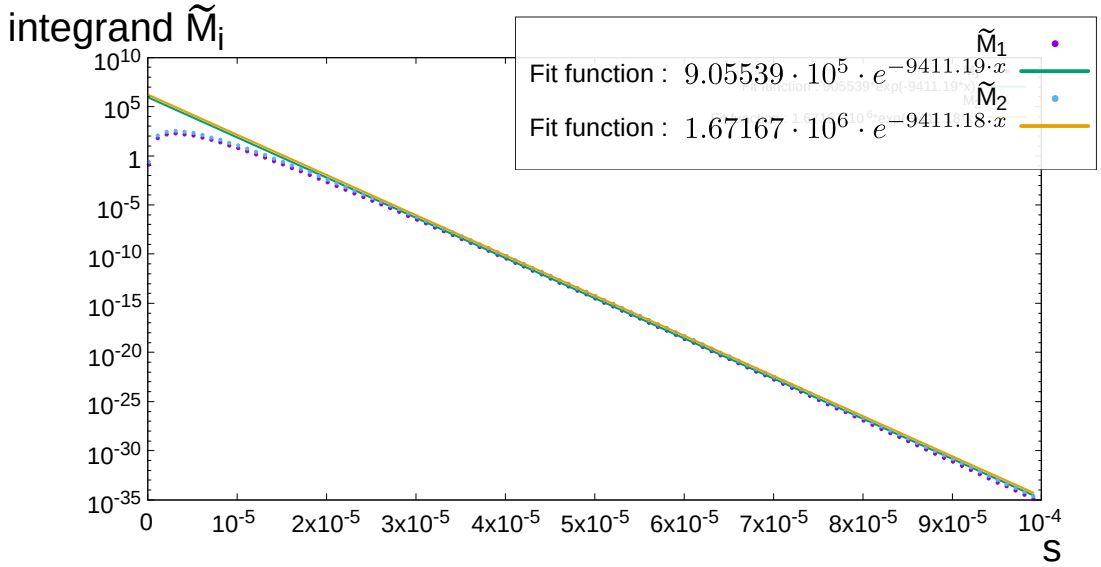

Figure 3.10: Plot of M_1 and M_2 from $s = 0$ to $s = 0.01$ for $B' = 10^{-4}$ with an exponential fitted to the tail (from $s = 0.005$ to $s = 0.01$).

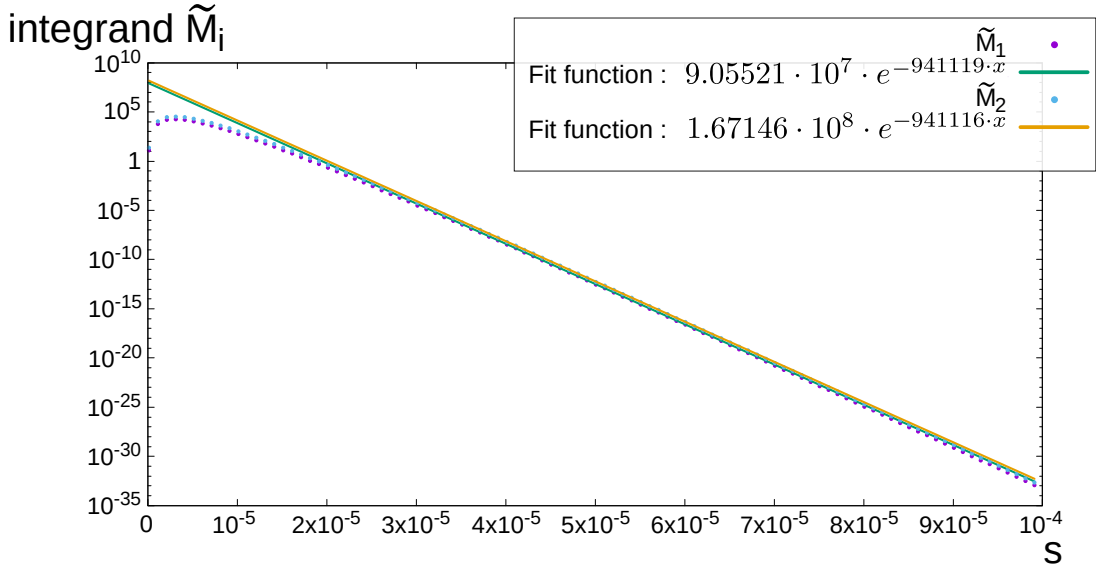

Figure 3.11: Plot of M_1 and M_2 from $s = 0$ to $s = 10^{-4}$ for $B' = 10^{-6}$ with an exponential fitted to the tail (from $s = 5 \cdot 10^{-5}$ to $s = 10^{-4}$).

Using the fitting parameters, one can estimate the error due to the choice of the cut-off $\delta_{\text{abs,cut}}$ with the following equation (see equation 3.29):

$$\begin{aligned} \delta_{\text{abs,cut}} &= \int_{s_{\text{cut}}}^{\infty} \tilde{M}_{\text{i}}(s)\, ds = \int_{0}^{\infty} \tilde{M}_{\text{i}}(s)\, ds \; - \; \int_{0}^{s_{\text{cut}}} \tilde{M}_{\text{i}}(s)\, ds \\ &\approx \int_{s_{\text{cut}}}^{\infty} a \cdot \exp(-b \cdot s)\, ds = \frac{a}{b} \cdot \exp(-b \cdot s_{\text{cut}}). \end{aligned} \tag{3.29}$$

Although the hyperbolic function h_{i} also contains terms that tend towards exponentials and further steepen the slope of the tail for large s, not taking this into account only overestimates the error. Solving equation 3.29 for s_{cut}, one can estimate for which cut-off point the resulting absolute error is at most $\delta_{\text{abs,cut}}$ (see equation 3.30).

$$s_{\text{cut}}(\delta \leq \delta_{\text{abs,cut}}) = -\frac{\log\left(\frac{b \cdot \delta_{\text{cut}}}{a}\right)}{b}. \tag{3.30}$$

The fits reveal the following parameters (see table 3.1):

Table 3.1: Fit parameters of the exponential fits to the tail of M_1 and M_2 for figures 3.9 to 3.11.

h_1	$B' = 10^{-2}$	$B' = 10^{-4}$	$B' = 10^{-6}$
a	9574.1	905539	$9.05521 \cdot 10^7$
b	-94.3345	-9411.19	-941119
h_2	$B' = 10^{-2}$	$B' = 10^{-4}$	$B' = 10^{-6}$
a	18464.4	$1.67167 \cdot 10^6$	$1.67146 \cdot 10^8$
b	-94.5081	-9411.18	-941116

Given these values, we can see that the following relation approximately holds:

$$\frac{a(B')}{a(B'_0)} = \frac{b(B')}{b(B'_0)} = \frac{B'}{B'_0}, \tag{3.31}$$

which verifies equation 3.28 with the use of equation 3.29. For the further analysis, I set the maximal error to 10^{-10}, which yields a cut-off point for the upper integration limit at $s_{\text{cut}}(B' = 10^{-2}) \approx 0.3 = 30 \cdot B'$, with which we can compute the cut-off point for other values of $B' \ll 1$.

To investigate the effects of the number of sampling points on the precision of the integrals, they were evaluated via the *Gauss-Legendre algorithm* [50] for different values of n ranging from 100 to 10000 in steps of 100 up to $n = 1000$ and in steps of 1000 up to $n = 10000$; the relative error of each integral $M_{\text{i}}(n)$ was estimated by calculating the absolute value of the relative difference to the value of the integral obtained for $n = n_{\text{max}} = 10000$ because the lowest deviation from the true value can, naively, be assumed for the largest number of sampling points (see equation 3.32):

$$\delta_{\text{rel,n}_{\text{max}}}(n) \approx \frac{|M_{\text{i}}(n_{\text{max}}) - M_{\text{i}}(n)|}{M_{\text{i}}(n_{\text{max}})}. \tag{3.32}$$

The plot of $\delta_{\text{rel,n}}$ versus n for $B' = 10^{-2}, 10^{-4}, 10^{-6}, 10^{-12}$ can be seen in figure 3.12.

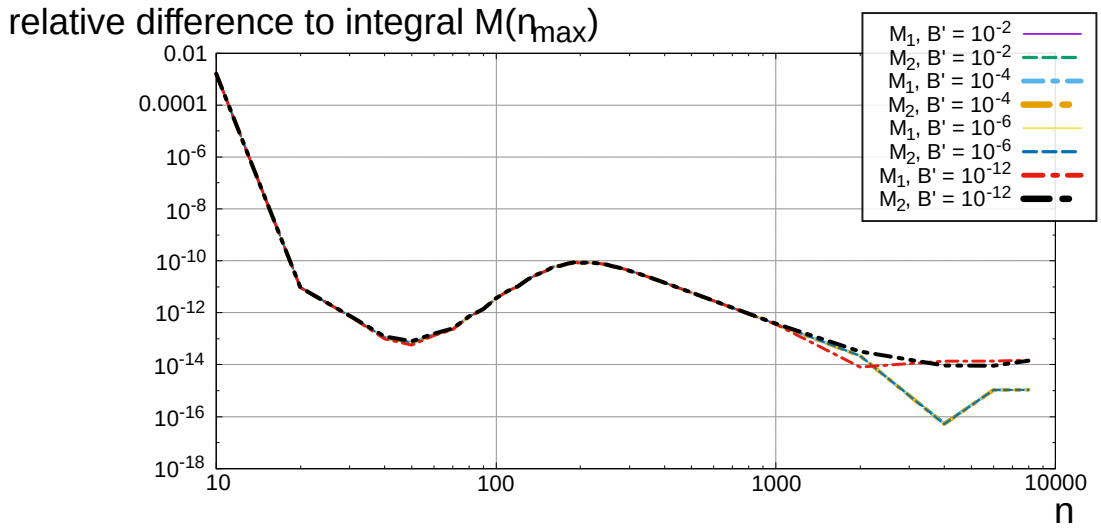

Figure 3.12: Plot of the relative difference of the integral values M_1 and M_2 with respect to the result for the highest number of sampling points $n = 10000$ for $B' = 10^{-2}, 10^{-4}, 10^{-6}, 10^{-12}$ as function of n.

Up to $n = 1000$, the dependence on n seems to be very similar for both integrals and all magnetic fields; the relative error quickly decreases below 10^{-10} (for $n \geq 20$) but seems to fluctuate between 10^{-13} and 10^{-10}. Beyond $n = 1000$, the relative errors for $B' = 10^{-12}$ deviate from those for larger magnetic fields, which, in turn, remain very similar to one another. This pair tends towards a relative error of 10^{-14}, while the rest tend towards 10^{-15}. On the one hand, these results show that only $n > 20$ sampling points are needed to assure that the relative error is less than 10^{-10}, but, on the other hand, a further reduction of the error is not easily achieved and cannot be predicted. Moreover, given the trend of the relative difference for $n > 1000$, the assumption that $M_{\mathrm{i}}(n = 10000)$ is the most precise value for the integral is not necessarily justified, but the error probably only lies within the 14th and 15th decimal places, as the relative differences only appear to fluctuate within this range.

Lastly, I verified the weak-field limits of M_1 and M_2, that can be ascertained from equation 3.23, by computing the integrals for $n = 50,\ 100,\ 500,\ 1000$ as function of B' (varying from 10^{-2} to 10^{-12}, the order of magnitude of the (geo-)magnetic field at Auger) and calculating the relative difference to these limits (see figure 3.13).

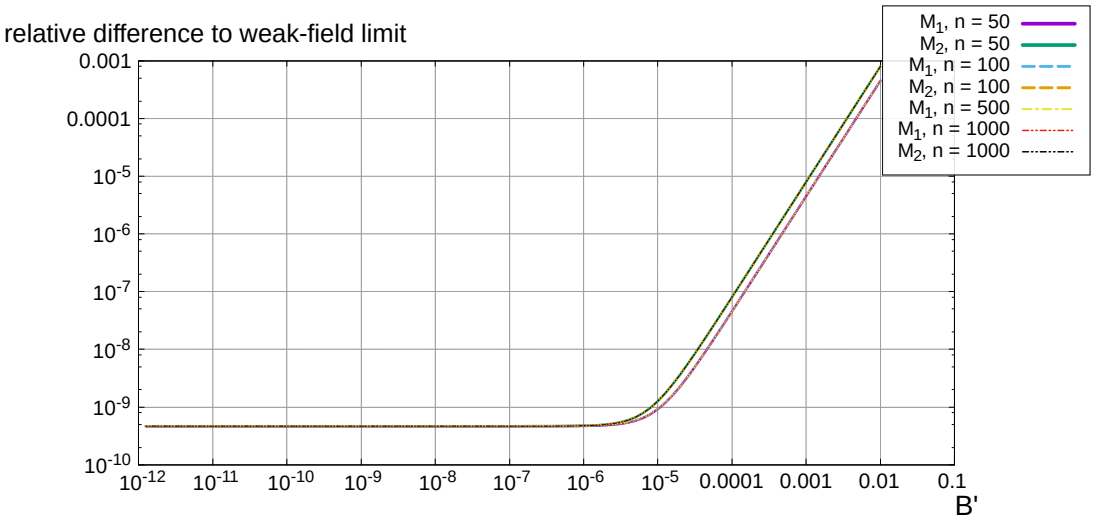

Figure 3.13: Plot of relative difference of the integral values M_1 and M_2 with respect to the weak field limits as given in equation 3.23 as a function of B' for different numbers of sampling points n.

One can see that the integrals quickly converge towards the weak-field limits, reaching a relative deviance of around $5 \cdot 10^{-10}$ at $B' = 10^{-6}$; below this, the relative difference stays constant, which can be explained by the choice of the cut-off point at $30 \cdot B'$ (leading to $\delta_{\text{abs,cut}} \approx 10^{-10}$ or $\delta_{\text{rel,cut}} \approx 10^{-9}$) and of the number of sampling points (leading to $\delta_{\text{rel,n}} \lesssim 10^{-10}$). Again, the number of sampling points n does not appear to have a strong effect on the precision as the deviation is the same for all n. The weak-field limit is, thereby, verified and can be assumed for magnetic fields of around $B' = 10^{-12}$ (order of magnitude of the maximum strength of geomagnetic field) to an (relative) accuracy of at least 10^{-10}. Using this fact, equation 3.23 applies, and the attenuation coefficient given in equation 3.22 can be simplified:

$$T_{\text{sp}}(\omega) \approx \frac{\alpha^3}{10\pi^2} \frac{1}{\lambda} \left(\frac{19}{315}\right)^2 \cdot (B' \sin\theta)^6 \cdot \left(\frac{\omega}{m}\right)^5, \tag{3.33}$$

where, as mentioned before, $\theta = 180°$ for the scope this analysis. This equation is said to be valid for the low-frequency non-dispersive limit, which was characterised by Harding et al. [28] via equation 3.18. Part of the $B-\omega$ phase space relevant for the Pierre Auger Observatory falls into this limit. This part of the phase space is plotted in figure 3.14; the line for $\frac{\omega}{m_e} \cdot B' = 1$ signifies the upper boundary of the low-frequency non-dispersive limit and is also drawn into

the plot.

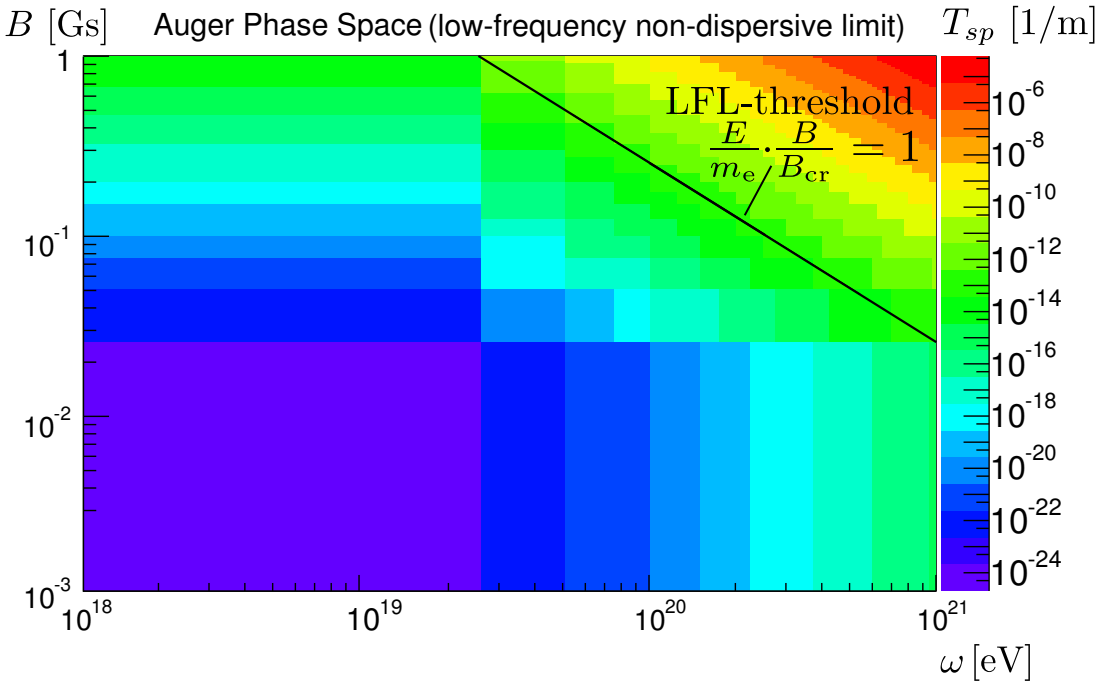

Figure 3.14: Auger phase space of the attenuation coefficient T_{sp}, including the line for $\frac{\omega}{m_e} \cdot B' = 1$.

The attenuation coefficient varies by more than 18 orders of magnitude from $\sim 10^{-24}$ m^{-1} to $\sim 10^{-6}$ m^{-1}, though the applicable region, i.e. the region for which $\frac{\omega}{m_e} \cdot B' \lesssim 1$ (see equation 3.18) ends at s$\sim 10^{-12}$ m^{-1}. These very short attenuation coefficients, corresponding to absorption lengths of $\sim 10^{12}$ m, indicate that photon splitting does not seem to play a large role in the low-frequency non-dispersive, weak-field limit. Given that the energies are in the order of $10^{15} \cdot m_e \gg m_e$, referring to this limit as the low-frequency limit does not seem suitable for weak magnetic fields and, in fact, it might not be applicable for Auger conditions, at all; however, as only the inequality in equation 3.18 seems to have to be satisfied and as Harding et al. [28] have used the equation of the attenuation coefficient for photon energies beyond the electron rest mass, this objection to the applicability of this limit can very well be unfounded. Lastly, the only way to settle whether the equations for the low-frequency limit are applicable for higher photon energies is by analysing the more general forms of the photon splitting probability. However, before the probabilities for arbitrary photon energies and magnetic fields can be analysed, one must investigate the "intermediate" case where $\omega \leq 2\, m_e$ and cross-check its results with those of the low-frequency limit, in order to have values with which to

compare the results of the more general forms. This case should also give us information on the applicability of the low-frequency non-dispersive limit for Auger conditions.

Non-dispersive case, below pair-production threshold

The probability for a photon to split in the non-dispersive case where $\omega \leq 2m_{\mathrm{e}}$ was derived in section 3.1.1 and is given in equations 3.12 to 3.17. Still, it is sensible to check for possible typos or other errors before attempting to calculating the probability, i.a. because the corresponding scattering amplitude is a triple integral which is significantly more complex and laborious to evaluate compared to the one-dimensional integral in the low-frequency case. As a first step, it makes sense to write equation 3.14 as a one-dimensional integral by defining the integrand $M(s)$ (see equation 3.34):

$$M(s) := \frac{ie^4B}{\pi^{1/2}} \int_0^s dt \int_0^t du\ \tilde{M}(s, t(s), u(t(s))). \tag{3.34}$$

This integrand should have a similar form as $M_{\mathrm{i}}(s)$, $i = 1, 2$, i.e. it should converge for $s \to 0$ and tend towards zero for $s \to \infty$. The limit for $s \to 0$ is also most likely zero; this is the case if $\tilde{M} < s^{-2}$ for a small enough s, as is shown in equation 3.35:

$$\begin{aligned} M(s) &= \frac{ie^4B}{\pi^{1/2}} \int_0^s dt \int_0^t du\ \tilde{M}(s, t(s), u(t(s))) \\ &= \lim_{n_{\mathrm{t}}, n_{\mathrm{u}} \to \infty} \frac{ie^4B}{\pi^{1/2}} \sum_{j=0}^{n_t} \sum_{k=0}^{n_u} \Delta t_{\mathrm{j}} \Delta u_{\mathrm{k}} \cdot \tilde{M}(s_{\mathrm{i}}, t_{\mathrm{j}}, u_{\mathrm{k}}) \\ &< \lim_{n_{\mathrm{t}}, n_{\mathrm{u}} \to \infty} \sum_{j=0}^{n_t} \sum_{k=0}^{n_u} \Delta t_{\mathrm{j}} \Delta u_{\mathrm{k}} \cdot s^{-k} \\ &\leq s^{2-k}, \end{aligned} \tag{3.35}$$

where $k < 2$ and $\tilde{M} < s^{-k}$; the fourth line holds because $\sum_{j=0}^{n_t} \Delta t_{\mathrm{j}} \leq s$ and $\sum_{k=0}^{n_u} \Delta u_{\mathrm{k}} \leq t_{\mathrm{j}}$ have to be satisfied. Figure 3.15 shows the maximal value of $\tilde{M}$ for $s \in [10^{-100}, 1]$, for all possible photon modes (see equation 3.15), and for different magnetic field strengths $B' =$

$10^{-12}, 10^{-6}, 10^{-1}$ and photon energies $\frac{\omega}{m_e} = 10^{-12}, 10^{-6}, 10^{-1}$; for each case, $\tilde{M}_{\max} < s^{-2}$ is fulfilled for s approaching zero, as is visualised by the fact that each line runs below the s^{-2} line (thick yellow line). We, therefore, expect $M(s) \to 0$ for $s \to 0$ should apply.

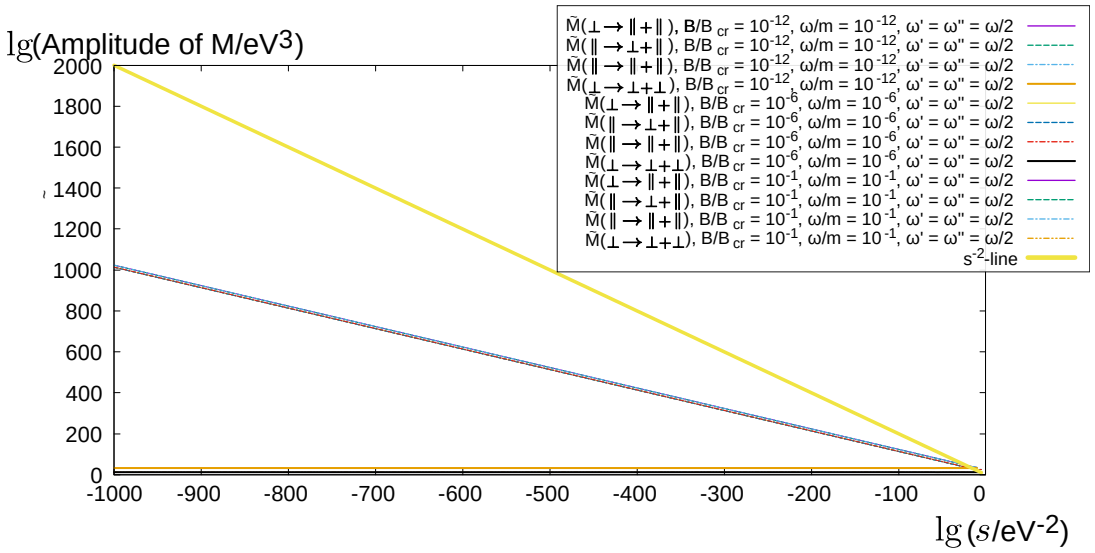

Figure 3.15: The maximal value of $\tilde{M}$ for $s \in [10^{-100}, 1]$, for all possible photon modes (see equation 3.15), and for different magnetic field strengths $B' = 10^{-12}, 10^{-6}, 10^{-1}$ and photon energies $\frac{\omega}{m_e} = 10^{-12}, 10^{-6}, 10^{-1}$; due to the lack of visibility, it needs to be stated explicitly that all lines overlap, apart from those indicating the interaction $\perp\to\perp + \perp$; in addition, the orange lines among these separately overlap.

To check whether $M(s) \to 0$ for $s \to \infty$, as is required for integrability, it is helpful to look at the approximations of the hyperbolic functions for large input variables (see equation 3.36):

$$\sinh(s) = \frac{e^s - e^{-s}}{2} \approx \frac{e^s}{2}, \text{ and } \cosh(s) = \frac{e^s + e^{-s}}{2} \approx \frac{e^s}{2}, \text{ for large } s. \tag{3.36}$$

With this, we can modify $f(s)$ (from equation 3.14) accordingly (see 3.37):

$$f(s) = \frac{e^{-m^2 s}}{s^3 \sinh^4(eBs)} \approx \frac{e^{-m^2 s}}{s^3 \left(\frac{\exp(eBs)}{2}\right)^4} = \frac{16}{s^3} \exp\left[-(m^2 + 4eB)s\right]. \tag{3.37}$$

For $g(s,t,u)$, the behaviour for large input variables depends on how s, t and u behave with respect to each other because this has a large impact on the difference of any of the variables. As a first step, the maximum of $\tilde{M}(s,t,u)$, which is at $t = u = \frac{s}{2}$, is evaluated, and I distinguish the following three cases:

- $u = (1-\epsilon)\cdot t, t = \frac{s}{2}$
  $\Rightarrow u = (1-\epsilon)\cdot\frac{s}{2}, \epsilon = \text{const.}, t-u = \epsilon\cdot\frac{s}{2}, s-u = (1+\epsilon)\cdot\frac{s}{2},$
- $u = t - \frac{\epsilon}{eB}, \epsilon = \text{const.}, t = \frac{s}{2}$
  $\Rightarrow u = \frac{s}{2} - \frac{\epsilon}{eB}, t-u = \frac{\epsilon}{eB}, s-u = \frac{s}{2} + \frac{\epsilon}{eB},$
- $u = t - \frac{\epsilon}{eB}, \epsilon = \epsilon(s), \epsilon \ll eBs, \lim_{s\to\infty}\epsilon = \infty, t = \frac{s}{2}$
  $\Rightarrow u = \frac{s}{2} - \frac{\epsilon}{eB}, t-u = \frac{\epsilon}{eB}, s-u = \frac{s}{2} + \frac{\epsilon}{eB}.$

Note, that I divide ϵ by $e\,B$ in the second and third case, because the term that is subtracted from u has to have the same dimension. The modification of $g(s,t,u)$ for each case is (see equations 3.38 to 3.40):

- $u = (1-\epsilon)\cdot t$

$$
\begin{aligned}
g(s,t,u) = &\left(\frac{u(s\text{-}t)}{s} - \frac{\sinh(eBu)\sinh(eB(s\text{-}t))\cosh(eB(t\text{-}u))}{eB\sinh(eBs)}\right)\omega^2 \\
&+ \left(\frac{u(t\text{-}u)}{s} - \frac{\sinh(eBu)\sinh(eB(t\text{-}u))\cosh(eB(s\text{-}t))}{eB\sinh(eBs)}\right)\omega'^2 \\
&+ \left(\frac{(t\text{-}u)(s\text{-}t)}{s} - \frac{\sinh(eB(t\text{-}u))\sinh(eB(s\text{-}t))\cosh(eBu)}{eB\sinh(eBs)}\right)\omega''^2 \\
\approx &\left(\frac{s(1\text{-}\epsilon)}{4} - \frac{1}{4eB}\right)\omega^2 + \left(\frac{s(1\text{-}\epsilon)\epsilon}{4} - \frac{1}{4eB}\right)\omega'^2 + \left(\frac{s\cdot\epsilon}{4} - \frac{1}{4eB}\right)\omega''^2 \\
\approx &\frac{s}{4}\omega^2 - \frac{1}{4eB}(\omega^2 + \omega'^2 + \omega''^2) \\
\Longrightarrow &\exp(g(s,t,u)) \sim \exp\left(\frac{s}{4}\omega^2\right)
\end{aligned}
\tag{3.38}
$$

- $u = t - \frac{\epsilon}{eB}$

$$
\begin{aligned}
g(s,t,u) &= \left(\frac{u(s\text{-}t)}{s} - \frac{\sinh(eBu)\sinh(eB(s\text{-}t))\cosh(eB(t\text{-}u))}{eB\sinh(eBs)}\right)\omega^2 \\
&\quad + \left(\frac{u(t\text{-}u)}{s} - \frac{\sinh(eBu)\sinh(eB(t\text{-}u))\cosh(eB(s\text{-}t))}{eB\sinh(eBs)}\right)\omega'^2 \\
&\quad + \left(\frac{(t\text{-}u)(s\text{-}t)}{s} - \frac{\sinh(eB(t\text{-}u))\sinh(eB(s\text{-}t))\cosh(eBu)}{eB\sinh(eBs)}\right)\omega''^2 \\
&\approx \left(\frac{s}{4} - \frac{\epsilon}{2eB} - \frac{\cosh(\epsilon)\exp(-\epsilon)}{2eB}\right)\omega^2 + \left(\frac{(\frac{s}{2}\text{-}\frac{\epsilon}{eB})\epsilon}{eBs} - \frac{\sinh(\epsilon)\exp(-\epsilon)}{2eB}\right)\omega'^2 \\
&\quad + \left(\frac{\epsilon}{2eB} - \frac{\sinh(\epsilon)\exp(-\epsilon)}{2eB}\right)\omega''^2 \\
&\approx \left(\frac{s}{4} - \frac{1}{2eB}\right)\omega^2 \\
&\Longrightarrow \exp(g(s,t,u)) \sim \exp\left(\frac{s}{4}\omega^2\right)
\end{aligned}
\tag{3.39}
$$

- $u = t - \frac{\epsilon}{eB}$, $\epsilon = \epsilon(s)$

$$
\begin{aligned}
g(s,t,u) &= \left(\frac{u(s\text{-}t)}{s} - \frac{\sinh(eBu)\sinh(eB(s\text{-}t))\cosh(eB(t\text{-}u))}{eB\sinh(eBs)}\right)\omega^2 \\
&\quad + \left(\frac{u(t\text{-}u)}{s} - \frac{\sinh(eBu)\sinh(eB(t\text{-}u))\cosh(eB(s\text{-}t))}{eB\sinh(eBs)}\right)\omega'^2 \\
&\quad + \left(\frac{(t\text{-}u)(s\text{-}t)}{s} - \frac{\sinh(eB(t\text{-}u))\sinh(eB(s\text{-}t))\cosh(eBu)}{eB\sinh(eBs)}\right)\omega''^2 \\
&\approx \left(\frac{s}{4} - \frac{\epsilon}{2eB} - \frac{\cosh(\epsilon)\exp(-\epsilon)}{2eB}\right)\omega^2 + \left(\frac{(\frac{s}{2}\text{-}\frac{\epsilon}{eB})\epsilon}{eBs} - \frac{\sinh(\epsilon)\exp(-\epsilon)}{2eB}\right)\omega'^2 \\
&\quad + \left(\frac{\epsilon}{2eB} - \frac{\sinh(\epsilon)\exp(-\epsilon)}{2eB}\right)\omega''^2 \\
&\approx \frac{s}{4}\omega^2 - \frac{1}{4eB}(\omega^2 + \omega'^2 + \omega''^2) \\
&\Longrightarrow \exp(g(s,t,u)) \sim \exp\left(\frac{s}{4}\omega^2\right)
\end{aligned}
\tag{3.40}
$$

The last line in each equation shows the dominating factor for $s \to \infty$, which is of main interest for investigating the behaviour of $\tilde{M}$ in this limit. In all three cases, this factor is the same.

For $D_1^\dagger$, the considerations indicated above need not be made as the term $t - u$ does not occur in the argument; again, the case $t = u = \frac{s}{2}$ is considered.

$$
\begin{aligned}
&D_1^\dagger\left(\omega,\omega',\omega'';s,t=u=\frac{s}{2}\right)\\
&\quad\approx\frac{\exp(3eBs)}{4}(\omega+\omega')\cdot\{([m^2-(\omega'\text{-}\omega'')^2+\omega'\omega'']s^2-s)\\
&\qquad\qquad+\exp(-eBs)[4eB+(\omega'+\omega'')^2]s^2\}\\
&\quad\sim\exp(3eBs)
\end{aligned}
\tag{3.41}
$$

Similarly, it follows for $D_2^\dagger$ (see equation 3.42; in the equation, $t-u$ does turn up once, but only in one term where the hyperbolic functions does not occur in the highest order and, thus, cannot be the dominating factor for $s\to\infty$):

$$
D_2^\dagger\left(\omega,\omega',\omega'';t=\frac{s}{2},u=\frac{s}{2}\right)\sim\exp(3eBs). \tag{3.42}
$$

In total, for $s\to\infty$, $\tilde{M}$ behaves according to the following exponential (see equation 3.43); the condition for integrability is also shown.

$$
\begin{aligned}
\tilde{M}(s,t,u)\sim\exp\left[\left(-m^2-4eB+3eB+\frac{\omega^2}{4}\right)s\right]&\overset{!}{\longrightarrow}0\text{ for }s\to\infty\\
\Longrightarrow-m^2-eB+\frac{\omega^2}{4}\overset{!}{\leq}0\Leftrightarrow\omega^2&\overset{!}{\leq}4m^2+4eB
\end{aligned}
\tag{3.43}
$$

We find that, at least for weak magnetic fields, as are present at the Pierre Auger Observatory, integrability is indeed ensured for photon energies below the pair production threshold, as is claimed in Stoneham [58]; the representation of the scattering amplitude in Stoneham [58] does not seem to contain any major typos. Knowing this, one can attempt to evaluate the double integral that is $M(s)$. In doing so, I ran into the problem that the program was unable to calculate the integral for large s (the output was "nan", i.e. not a number), as one part of the function was rounded to ∞, whereas another factor was rounded to 0. This problem was tackled by enabling, additionally to a controllable number of digits in the mantissa, a controllable range of the exponent; I tested the program for the range of the exponent of

± 10000, and found that the "nan"-problem was, indeed, successfully resolved. However, the convergence that is expected for $s \to \infty$ could not be numerically reproduced, even with more digits in the mantissa as well as in the exponent. Later, I found that the result of $\tilde{M}$ is strongly dependent on the way it is calculated, i.e. whether the parts of the functions $f(s)$, $D^{\dagger}(s,t,u)$ and $\exp[g(s,t,u)]$, into which I split $\tilde{M}$ (see equation 3.14), are computed separately or not, or whether the hyperbolic functions are expressed in their exponential forms. It is worth adding that I took the exponential factor from $f(s)$ and included it in $\exp[g(s,t,u)]$, so all exponential factors are within one part of the function; I named the resulting functions $\tilde{f}(s) = f(s)\cdot\exp(m^2\, s)$ and $\tilde{g}(s,t,u) = g(s,t,u)\cdot\exp(-m^2\, s)$. Figure 3.16 shows $M(s)$ calculated with 100 sampling points per variable via Gauss-Legendre quadrature for both t and u for different simultaneous calculations of different combinations of $D^{\dagger}$, $\tilde{f}(s) and \exp[\tilde{g}(s,t,u)]$ with $\omega = 10^{-12}\cdot 2\, m_{\mathrm{e}}$ and $B = 10^{-12}\, B_{\mathrm{cr}}$.

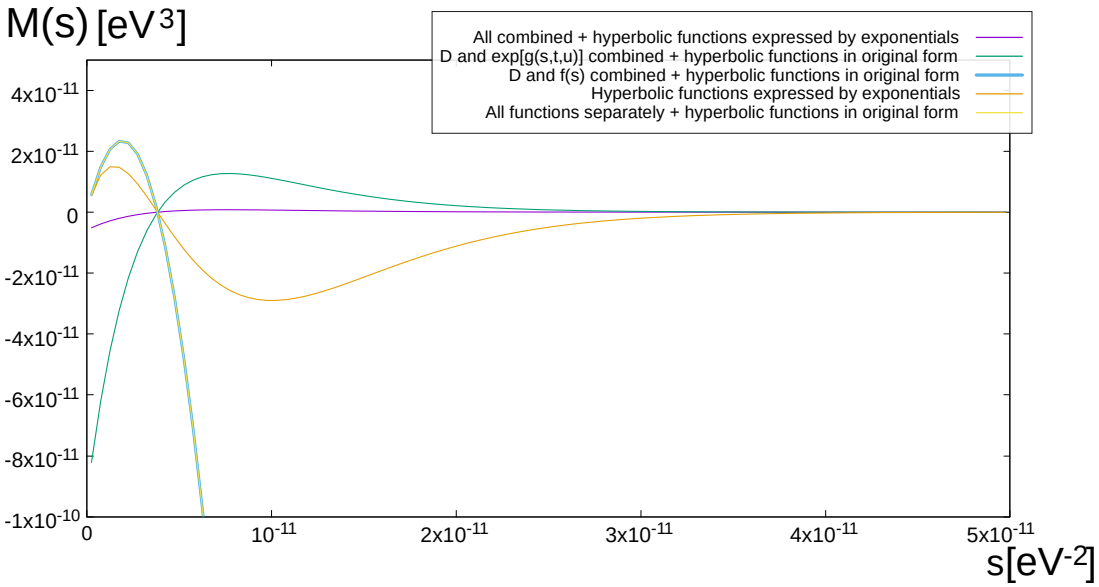

Figure 3.16: Calculations of $M(s)$ with different combinations of simultaneous computations of $D^{\dagger}$, $\tilde{f}(s)$ and $\exp[\tilde{g}(s,t,u)]$ with $\omega = 10^{-12}\cdot 2\, m_{\mathrm{e}}$ and $B = 10^{-12}\, B_{\mathrm{cr}}$; the double integral was evaluated via Gauss-Legendre quadrature with 30 sampling points.

Clearly, expressing the hyperbolic functions as exponentials and calculating all exponentials simultaneously has a strong impact on the results of the calculation of $\tilde{M}$. The reason for this could not be discerned, but it is clearly not due to a lack of precision as altering the range of the exponent and the number of digits in the mantissa had with no effect. In addition, only one method of calculating $M(s)$, namely calculating all parts of the $\tilde{M}$ in separate functions

but expressing the hyperbolic functions in their exponential form, fulfils the conditions that $M(s) \to 0$ for $s \to 0$ and $s \to \infty$ (see orange line); while both combining all parts into one function and writing the hyperbolic functions as exponentials (see purple line), on the one hand, and combining $D^\dagger$ and the exponentials into one function but leaving the hyperbolic functions in their original form (see green line), on the other, lead to finite values for $s \to 0$, as well $-$, albeit different values for each method $-$ it was expected that $M(s)$ would tend towards zero in this limit (see equation 3.35 and figure 3.15). The best way to discern which method of calculation is indeed correct is to compare the scattering amplitudes calculated via each method with the results from the low-frequency limit from equation 3.19, which were verified in section 3.1.2. For this, I evaluated the triple integral from equation 3.14 via Gauss-Legendre quadrature with 100 sampling points in each variable for $\omega = 10^{-12} \cdot 2\,m_\mathrm{e}$ and $B = 10^{-12}\,B_\mathrm{cr}$; I set the cut-off of the upper integration limit to $5 \cdot 10^{-11}$, as all calculation methods appear to be sufficiently flat at this value (except the two calculation methods that diverge for $s \to \infty$). I plotted the absolute value of the integrals, together with the integrals from the low-frequency case in section 3.1.2 multiplied by the necessary pre-factor shown in equation 3.19 (see figure 3.17).

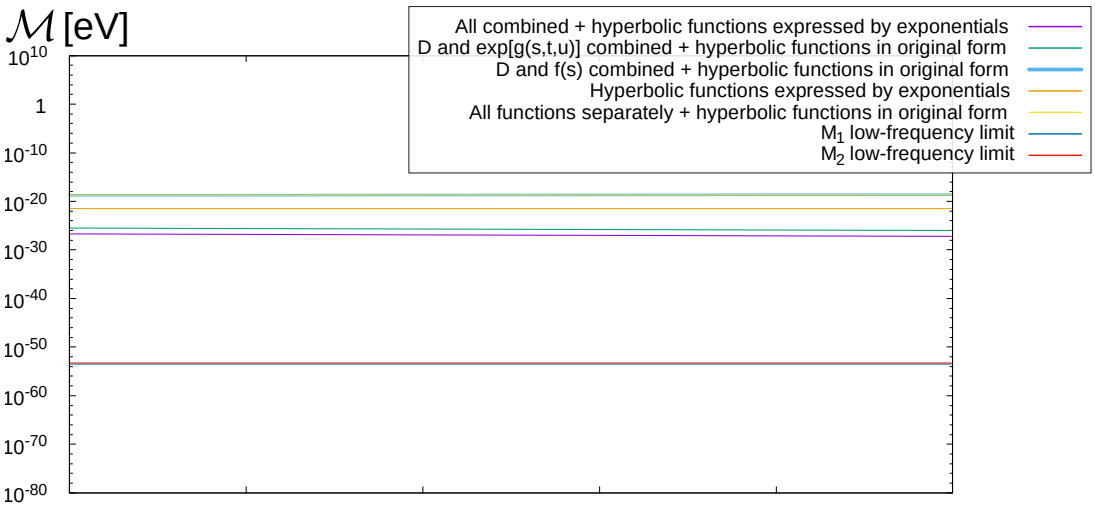

Figure 3.17: Calculations of the scattering amplitude for the different calculation methods as elucidated in figure 3.16, as well as the low-frequency integrals with $\omega = 10^{-12} \cdot 2\,m_\mathrm{e}$ and $B = 10^{-12}\,B_\mathrm{cr}$; the integrals were evaluated via Gauss-Legendre quadrature with 100 sampling points in each variable.

The plot shows that there is a large discrepancy between scattering amplitudes of the $\omega \leq$

$2m_e$-case and of the low-frequency limit; they differ by at least 26 orders of magnitude. I checked whether this discrepancy could be due to an insufficient number of sampling points by investigating the effect of using more sampling points, namely $n = 1000$; to save computation time, I only increased the number of sampling points for one variable and used 10 sampling points for the other two variables, but tested this for all three. Increasing the number of sampling points for one variable cannot compensate for the 26 order-of-magnitude difference between the $\omega \leq 2m_e$ case and the low-frequency limit, however, as they hardly change the integral values at all.

When comparing the pre-factors for both scattering amplitudes, one can see that the factor m^{-8} suppresses the magnitude of the scattering amplitude in the low-frequency limit significantly (in the order of 10^{-45}), and it cannot be counteracted by the factor $B^3 \cdot \omega\,\omega'\,\omega''$ in the numerator because this factor never exceeds $\sim \frac{1}{4}\,(m_e \cdot B_{cr})^3 \approx 10^{-10}\,m_e^8$ eV in the low-frequency limit (i.e. where $\omega' = \omega'' = \frac{\omega}{2}$ and $\frac{\omega}{m_e} \cdot B' = 1$). The origins of this discrepancy is not clear. One possibility is a faulty evaluation of the triple integral for which the following underlying reasons come to mind:

- The implementation of the integration method is faulty; this is, however, very unlikely as I checked the program for several analytically soluble functions, which worked with high precision.
- I made a mistake in writing down the integrand; I also doubt this because I re-typed it several times, always with the same results.
- The integrand is not calculated correctly; this could be the case because re-writing the function, i.e. writing the hyperbolic functions in the exponential form and calculating with different combinations of $\tilde{f}(s)$, $D^\dagger$ and $\exp[g(s,t,u)]$ in one function, had significant effects on the functional form of the integrand.
- There is a typo in the original function in Stoneham's paper; this cannot be ruled out, but it would constitute a general problem for the analysis of photon splitting as there is no other known solution that can be used for Auger conditions.

Unfortunately, the lack of convergence between my results and literature cuts the project of calculating the photon splitting probability short within the scope of this thesis; further

analyses must find a way of settling the origin of this discrepancy. Special focus should be put on assuring whether the triple integral in equation 3.14 was correctly evaluated. For now, we have to conclude that we cannot make a definite statement on photon splitting as a super-preshower process, neither can we safely apply the low-frequency limit to Auger conditions.

In trying to estimate the likelihood that photon splitting is dominant outside the low-frequency non-dispersive limit compared to pair production, it is worth reiterating that photon splitting as a third order quantum electrodynamical process is, naively, expected to be suppressed with respect to pair production, which is a first order process. While photon splitting appears to be of a comparable order of magnitude to pair production in the low-frequency limit and is even dominant for very strong magnetic fields and for low photon energies (see the right plot in figure 3.18), pair production seems to become dominant for larger energies, as well as for weaker fields (see left plot in figure 3.18) [28].

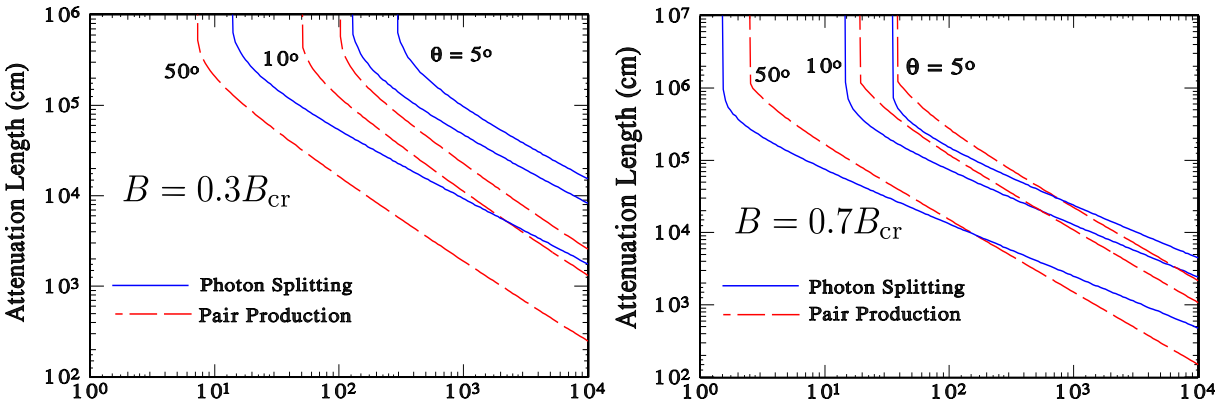

Figure 3.18: Attenuation length for photon splitting using the inverse of equation 3.22, and for single photon pair production as a function of energy, for photons originating from the surface of a neutron star at different angles with respect to its magnetic dipole field θ; left: surface field of $B = 0.3\,B_{\mathrm{cr}}$, right: $B = 0.7\,B_{\mathrm{cr}}$ [28].

A dominance of photon splitting in very strong fields is expected: The additional photon vertex in the Feynman diagram of photon splitting (see figure 3.1) can be thought of as an emission of a photon via bremsstrahlung by an electron in the electron propagator due to a disturbance, which is amplified for strong fields; since no such disturbance exists in the first order process of pair production as no electron emits a photon, stronger magnetic fields should not affect the probability of pair production to such an extent as they affect that of photon splitting. Conversely, pair production is expected to be dominant for weak magnetic fields where

no additional amplification of the photon splitting probability is expected. Unless there is a high-energy process which we have not considered so far, it seems unlikely that photon splitting could become dominant also outside the low-frequency non-dispersive limit, in particular for UHE photons and weak magnetic fields. While this estimation does not rule out photon splitting in the geomagnetic field for Auger conditions, which can only settled with detailed calculations of the relevant formulae, further pursuing it as a possible super-preshower process does not appear to be of highest priority. Photon splitting can still be investigated, for example in different magnetic fields at further distances from Earth, though the nature of these magnetic fields is not known. In addition, it might be worth exploring photon splitting in a plasma as there is evidence for a warm plasma around the Earth [20].

3.2 Pair production via solar and cosmic ray photons

The process of pair production via solar and cosmic ray photons has not been studied as a possible super-preshower process so far; however, particularly when the Pierre Auger Observatory is facing the Sun, it is possible that the flux of solar photons is high enough for this process to play a significant role and it is, thus, worth studying. In addition, if it has a non-negligible probability of occurring, there should be correlations with the time of day or the position of the Sun in the sky that could serve as a "fingerprint" of the process in the data.

In the following chapter, I will derive the probability of pair production via solar and cosmic ray photons; I will start by introducing the relevant theory and proceed by calculating the probability using the theoretical framework.

3.2.1 The theory of pair production via two photons

Pair production via two photons is a quantum electrodynamical process in which two photons interact to create an electron-positron pair; the probability W of a cosmic ray photon to interact with a target of solar photons is related to its cross section σ as represented in the following equation (see equation 3.44 [59]):

$$dW = dx\, n\, \sigma, \tag{3.44}$$

where dx is the thickness of a thin section of a material, i.e. the solar photons, and n is the number (volume) density of solar photons. In Greiner and Reinhardt [25], the cross section for photon-photon pair production is derived and can be seen in equation 3.45.

$$\sigma = \frac{\pi}{2} r_{\mathrm{e}}^2 \left(1 - v^2\right) \left[\left(3 - v^4\right) \log\left(\frac{1+v}{1-v}\right) - 2v(2 - v^2) \right], \tag{3.45}$$

where $r_{\mathrm{e}} = 2.818 \cdot 10^{-15}$ is the classical electron radius, $v = \sqrt{\frac{E_{\gamma 1} E_{\gamma 2} - m_{\mathrm{e}}^2}{E_{\gamma 1} E_{\gamma 2}}}$ with $E_{\gamma \mathrm{i}}$, $i = 1, 2$ being the energy of the interacting photons, and m_{e} is the rest mass of the produced particle,

i.e. the electron or positron, respectively.

The number density of solar photons can be derived from the Sun's flux, which can be approximated well as that of a black body with a temperature of $T_{\odot} = 5777$ K; the spectral radiance (as a function of photon frequency θ) is given by Planck's law (see equation 3.46 [54]):

$$B_{\nu} = \frac{2h\nu^3}{c^2}\left[\exp\left(\frac{h\nu}{k_{\mathrm{B}}T}\right) - 1\right]^{-1}, \tag{3.46}$$

where h is Planck's constant, c is the speed of light, and k_{B} is the Stefan-Boltzmann constant. The spectral radiance is defined as

$$B_{\nu} = \frac{\partial^3\Phi}{\partial\Omega\partial A\cos\theta\partial\nu}, \tag{3.47}$$

where $\Phi = \frac{\partial Q}{\partial t}$ is the radiant flux, or radiant energy per unit time, emitted by the Sun, Ω is the solid angle into which the light is emitted and $A\cos\theta$ is the projected surface area of the emitting body. Given that the Sun is spherical, every photon is emitted perpendicularly to the Sun's surface and, therefore, $\theta = 0$. To obtain the number of photons of energy $h\,\nu$ emitted per unit time, one must divide B_{ν} by said energy; through division by c, one determines the number of photons within a distance $ds = c\,dt$, and by integrating over the area and the solid angle, one obtains the number density n (see equation 3.48):

$$n_{\nu} = \frac{dn}{d\nu} = \int d\Omega \int \frac{B_{\nu}}{h\,\nu\cdot c} = \frac{8\pi^2\nu^2}{c^3}\left[\exp\left(\frac{h\nu}{k_{\mathrm{B}}T}\right) - 1\right]^{-1}. \tag{3.48}$$

With the transformation (see equation 3.49):

$$E = h\nu \Rightarrow dE = h d\nu, \tag{3.49}$$

one can derive an expression for the probability of a cosmic ray photon of energy $E_{\mathrm{cr}} := E_{\gamma 1}$ to create an electron-positron pair via interaction with solar photons of all possible energies $E_{\mathrm{sol}} := E_{\gamma 2} \geq \frac{m_{\mathrm{e}}^2 c^4}{E_{\mathrm{cr}}}$ (see equation 3.50):

$$
\begin{aligned}
W &= \int_{x_0}^{x_1} dx \int_{\frac{m^2\,c^4}{E_{\text{cr}}}}^{\infty} dE_{\text{sol}}\, n_{E_{\text{sol}}} \cdot \sigma(E_{\text{sol}}) \\
&= \frac{4\pi^3 r_{\text{e}}^2\, R_{\odot}^2}{h^3\, c^3} \cdot \int_{x_0}^{x_1} dx \int_{\frac{m^2\,c^4}{E_{\text{cr}}}}^{\infty} dE_{\text{sol}}\, (1\text{-}v^2) \left[(3\text{-}v^4) \log\left(\frac{1+v}{1-v}\right) \text{-}2v(2\text{-}v^2) \right] \cdot \frac{E_{\text{sol}}^2}{\exp\left(\frac{E_{\text{sol}}}{k_{\text{B}}T}\right) \text{-}1}.
\end{aligned}
\tag{3.50}
$$

The integration over x is somewhat problematic as the relation between the distance s of the photons from the Sun and the thickness x of the layer depend on the arrival direction of the cosmic ray photon, on the one hand, and the density of solar photons is not constant along the path of the cosmic ray photon, on the other. As we are, first, only interested in an estimate of the probability, it is sensible to look at the case where the cosmic ray photon approaches Earth along the path of the direction vector between the Sun and the Earth, meaning that $x = s$; this constitutes the path where the probability of the interaction is highest.

The number (area) density of photons $\tilde{n}$ falls quadratically with the distance s from the Sun as the surface area of a sphere with its centre at the Sun increases exactly by this rate but the total number of photons N_{tot} across the entire surface stays the same (see equation 3.51):

$$
\begin{aligned}
N_{\text{tot}} &= 4\pi s^2 \tilde{n}(s) = 4\pi R_{\odot}^2 \tilde{n}(R_{\odot}) \\
\Rightarrow \tilde{n}(s) &= \tilde{n}(R_{\odot}) \cdot \frac{R_{\odot}^2}{s^2} \\
&= \frac{N_{\text{tot}}}{4\pi s^2}.
\end{aligned}
\tag{3.51}
$$

The same also applies for the volume density n; as a result, the probability can be expressed as (see equation 3.52):

$$
\begin{aligned}
W &= \int_{s_0}^{s_1} ds \int_{\frac{m^2}{E_{\text{cr}}}}^{\infty} dE_{\text{sol}}\, \frac{n_{E_{\text{sol}}}}{4\pi s^2} \cdot \sigma(E_{\text{sol}}) \\
&= \frac{\pi^2 r_{\text{e}}^2\, R_{\odot}^2}{h^3\, c^3} \cdot \int_{s_0}^{s_1} \frac{ds}{s^2} \int_{\frac{m^2}{E_{\text{cr}}}}^{\infty} dE_{\text{sol}}\, (1\text{-}v^2) \left[(3\text{-}v^4) \log\left(\frac{1+v}{1-v} \right) \text{-} 2v(2\text{-}v^2) \right] \cdot \frac{E_{\text{sol}}^2}{\exp\left(\frac{E_{\text{sol}}}{k_{\text{B}} T} \right) \text{-} 1} \\
&= \frac{\pi^2 r_{\text{e}}^2\, R_{\odot}^2}{h^3\, c^3} \left(\frac{1}{s_0} \text{-} \frac{1}{s_1} \right) \cdot \int_{\frac{m^2}{E_{\text{cr}}}}^{\infty} dE_{\text{sol}}\, (1\text{-}v^2) \left[(3\text{-}v^4) \log\left(\frac{1+v}{1-v} \right) \text{-} 2v(2\text{-}v^2) \right] \cdot \frac{E_{\text{sol}}^2}{\exp\left(\frac{E_{\text{sol}}}{k_{\text{B}} T} \right) \text{-} 1},
\end{aligned}
\tag{3.52}
$$

where s_0 and s_1 constitute the starting and end point of the cosmic ray photon with the respect to the Sun.

3.2.2 Calculating the probability of pair production via cosmic ray and solar photons for Auger conditions

The probability of photon-photon pair production via cosmic ray and solar photons was derived in section 3.2.1 and is shown in equation 3.52 for the case of the cosmic ray photon approaching Earth along the direction vector between the Sun and the Earth. The photon is assumed to originate at a distance $s_0 \to \infty$ and to travel past the Sun to Earth at $s_1 = -1$ AU. To calculate the probability, one only needs to evaluate the integral over E_{sol}, which has to be done numerically. I evaluated said integral for several cosmic ray photon energies ranging from 10^{16} eV to 10^{20} eV via Gauss-Legendre quadrature for $n = 10000$ sampling points; I also set a cut-off on the maximum solar photon energy to 10 eV (see figure 3.19 of the spectral radiance as a function of the photon energy B_{E}).

The probability of pair-production via photon-photon interaction of cosmic ray and solar photons is shown in figure 3.20. It is in the order of 10^{-8} at most. With this result, we can safely rule out pair production via solar and cosmic ray photons as a possible super-preshower process.

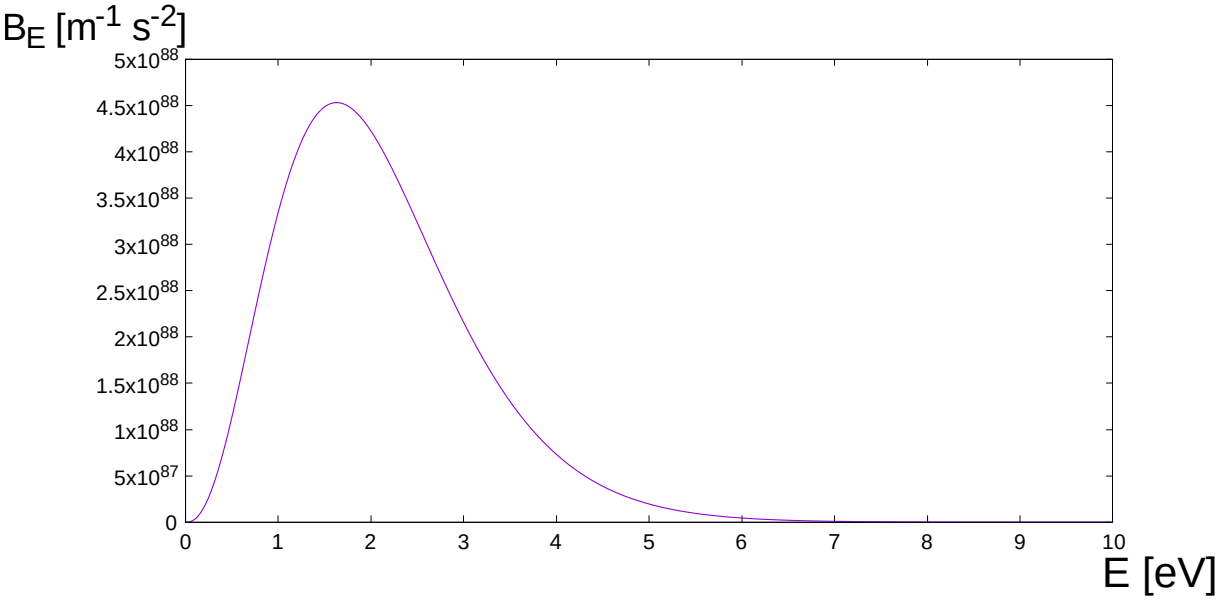

Figure 3.19: Spectral radiance as a function of the photon energy B_{E}.

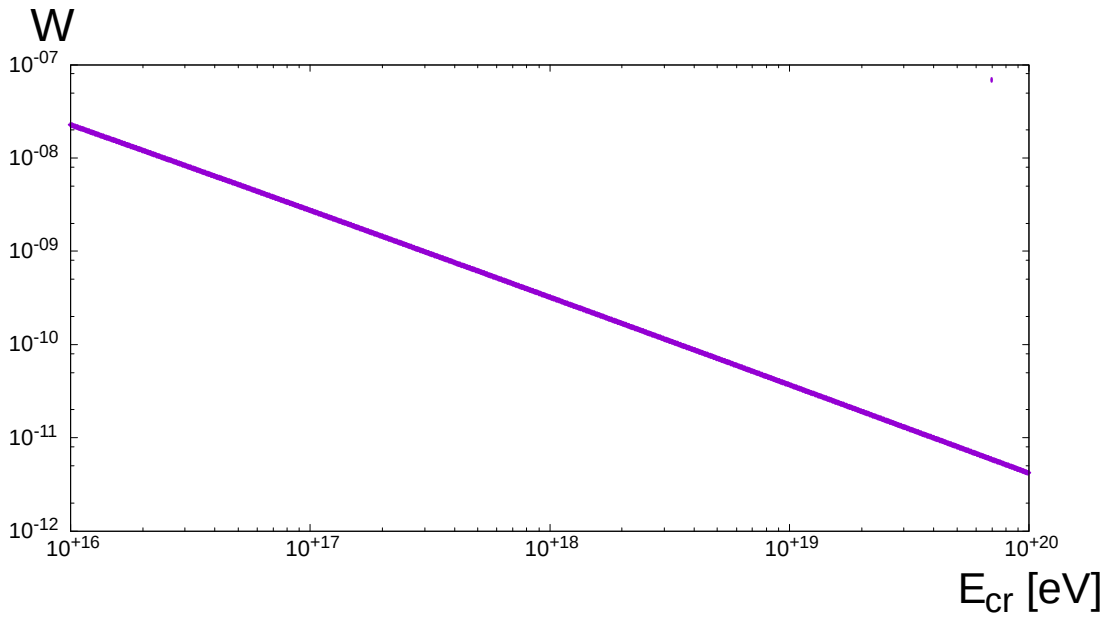

Figure 3.20: Probability of a cosmic ray photon to interact with a solar photon to create an electron-positron pair as traverses along the direction vector of the path from the Sun to the Earth.

Chapter 4

Super-preshowers in simulations

Irrespective of whether any of the processes mentioned in chapter 3 are, indeed, candidates for super-preshowers, it is of interest to see how super-preshowers would influence Auger observables, in order to know what to search for in the data. Moreover, the data discussed in section 2.3 set very specific requirements on the properties of photon initiated showers that had undergone super-preshowering, especially pertaining to the energy deposit and the number of muons; the fact that the data suggests a predominantly hadronic compostion at highest energies gives special significance to the question under which circumstances photon-induced showers, in particular those with super-preshowering, can "mimic" hadronic ones. This question will be addressed via air shower simulations with *Conex*, in which showers initiated by photons with super-preshowering will be compared to proton- and iron-induced showers.

4.1 Simulations of super-preshowers using CONEX— the effects on Auger parameters

Conex, according to Bergmann et al. [15], is "an efficient scheme for one-dimensional extensive air shower simulation". It takes into account both the high-energy part of hadronic and electromagnetic cascades in the atmosphere, as well as smaller energy sub-showers using explicit Monte Carlo simulations for the former, combined with numerical solutions of cascade

equations for the latter, with which accurate air showers simulations are possible that are consistent with the conventionally used *Corsika* [29], a more detailed, but slower program for the same purpose. It is, therefore, as suitable tool to correctly interpret the data for experiments such as the PAO.

One goal of the simulations is to verify the preliminary results by Homola [31] mentioned in section 2.4; they will, therefore, include the comparison between photon initiated and hadronic showers for two main parameters, namely the energy deposit $\frac{dE}{dX}$, where X is the shower depth in g cm^{-2}, and the production of muons, which, for the scope of the analysis, entails the number of muons N_μ and its production rate dN_μ per shower depth bin ($= 10$ g cm^{-2}), respectively. The simulations will include longitudinal profiles of both main parameters as these facilitate a direct comparison between photon initiated and hadronic showers. As already mentioned in section 2.3.2, an important observable for mass composition measurements at the Pierre Auger Observatory related to the energy deposit is the depth of maximal energy deposit X_{max}; this quantity will serve as a starting point to investigate the energy range and altitude for which super-preshowers lead to consistent results with Auger data.

4.1.1 Implementing super-preshowers in CONEX

As a first step, the implementation of a super-preshower in *Conex* was done by manually forcing the first conversion of a primary photon at high altitudes in the file *preshw.c* with which preshowers are simulated. Through further manipulation of the program, I was able to include the altitude of the first conversion, or starting altitude, as an input parameter, which significantly simplified the analysis of super-preshowers, in particular for simulations of multiple showers. It is worth noting that, since only the conversion of the primary photon is forced, the secondary photons rarely convert; however, for sufficiently energetic primaries, the secondary particles would contain high-energy photons that could undergo further pair production interactions. Such a scenario will be discussed later.

The variable with which one manually sets the starting amplitude does not equate with the actual starting altitude, but I determined the functional relation between the two by plotting the starting altitude versus the corresponding variable, henceforth called *starting altitude parameter*, and then fitting a polynomial in combination with two exponentials to the points (see

figure 4.1); although the relation between the starting altitude parameter and the actual starting amplitude appears to be linear, in particular for larger altitudes, a more complex fitting function was necessary to accurately describe the points corresponding to lower altitudes (see bottom plot).

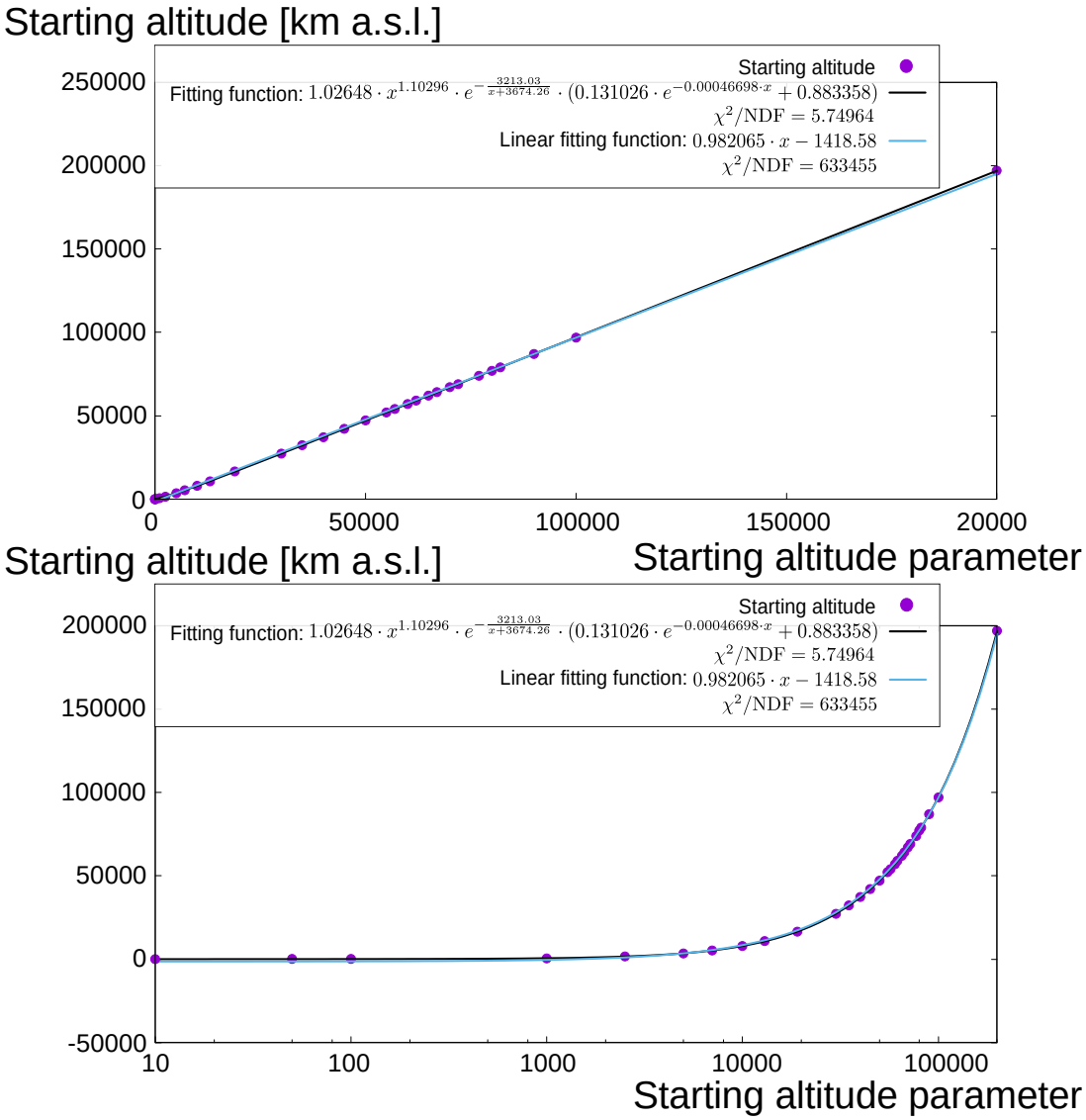

Figure 4.1: Starting altitude in km a.s.l. versus starting altitude parameter, including two fitting functions to approximate their functional relation (the blue line pertaining to a linear fit was included to show that such a function fails to approximate the points for small altitudes); the top plot shows a linear scaling of the x-axis and the bottom plot a logarithmic scaling.

For all simulations, the interaction model *QGSJet01* was used [38]. The other interaction models that are used in the analysis of Auger data, i.e. Sibyll2.1, Epos-LHC and QGSJet-II-04 (see section 2.3.2), are also included in *Conex*, of which I was not aware as I started working on the simulations. However, as QGSJet01 predictions do not differ drastically from those of the other models, re-simulations are not necessary.

4.1.2 Analysis of the energy deposit

One important objective of these simulations is to find the altitude of super-preshowers for which X_{max} values correspond to current Auger data (see figure 2.14 in section 2.3.2), i.e. lie in the range of approximately $700 - 800$ g cm^{-2}. First, I looked at the dependence of X_{max} on the starting altitude by simulating 100 photon-induced showers with the primary energy of $10^{19.6}$ eV $\approx 4 \cdot 10^{19}$ eV (the choice of this energy will be explained later) entering the atmosphere at a zenith angle of 60° and an azimuth angle of 180° (this arrival direction is also known as the *strong B direction* as the transverse component of the magnetic field B_{T} is comparably large [33]) for starting altitudes ranging from 554 km a.s.l. to $196,889$ km a.s.l. (i.e. starting altitude parameters from 1000 to $2 \cdot 10^5$). The X_{max} values were plotted as a function of the starting altitude and an exponential was fitted to the data (see figure 4.2). It is important that the conversion starts above the top of the atmosphere ~ 100 km a.s.l. as preshowers are only initiated there, and, otherwise, the calculations would yield too high X_{max} values.

There appears to be an exponential "decay" of the starting altitude, i.e. the decrease of X_{max} converges exponentially towards a limit, $X_{\text{max,lim}} = 780.4$ g cm^{-2}, with increasing altitude; this limit lies within the required range for X_{max} mentioned above. The convergence is very strong, and the X_{max} value at an altitude of about 30000 km a.s.l. corresponds to the limit $X_{\text{max,lim}}$, especially within the margin of error.

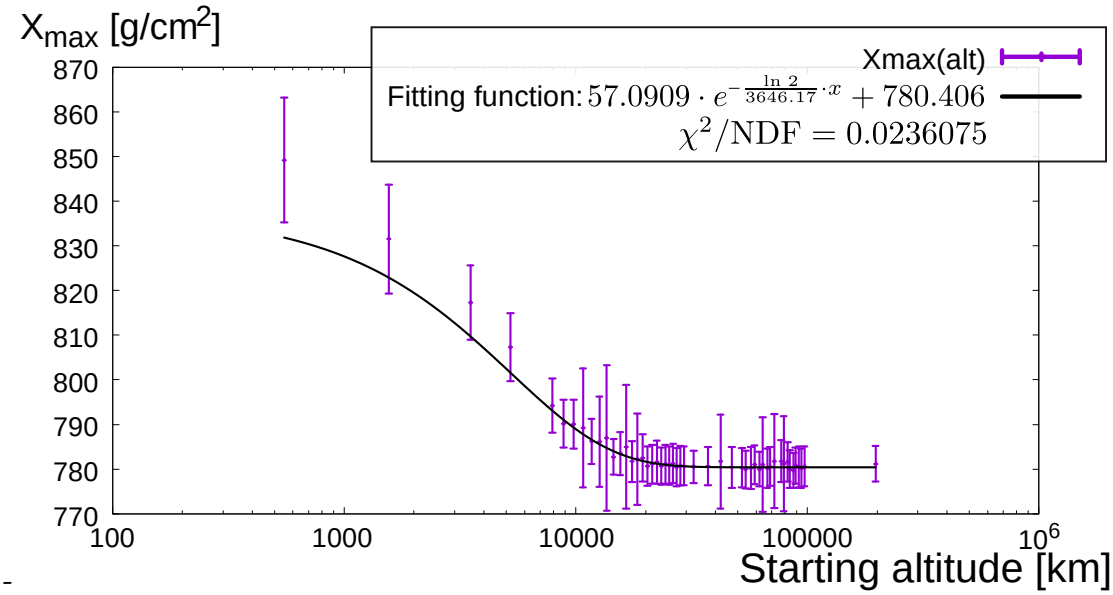

Figure 4.2: $X_{\max}$ of photon initated showers with an energy of $10^{19.6}$ eV arriving from the strong B direction as a function of the starting altitude, including an exponential fit to the data.

It is also important to look at the energy dependence of $X_{\max}$ for super-preshowers, in order to find the energy range for which photons can be expected to play a significant role in the cosmic ray composition. Due to the rapid convergence of $X_{\max}$ with the altitude, I set the starting altitude to 27270 km a.s.l. (corresponding to a starting amplitude parameter of 30000) and the photon primary energy to range from 10^{18} eV to 10^{21} eV. Figure 4.3 shows $X_{\max}$ plotted versus the primary energy with 100 showers per energy. I included the (extrapolated) proton and iron lines from Aab et al. [2] (see also figure 2.14 in section 2.3.2) to visualise the approximate range the values of $X_{\max}$ are allowed to occupy for super-preshowers to be consistent with Auger data; the solid lines indicate the predictions from Epos-LHC and the dashed lines those from QGSJetII-04. At this point, it is worth noting that the Auger data actually indicates a mass composition dominated by intermediate mass nuclei, which alternative compositions including photons that underwent super-preshowering, ultimately, would have to reproduce. As we are not expecting a pure photon composition, or even a clearly dominant photon fraction because photons should already have been observed at the Pierre Auger Observatory for such scenarios, detailed simulations of showers for several different composition scenarios are needed, which is not feasible for the scope of this thesis. Moreover, certain composition scenarios that contain a significant photon fraction could be consistent with the $X_{\max}$ data,

even for those $X_{\max}$ values of super-preshowers that do not fall within the hadronic range. Therefore, the analysis of the energy dependence of $X_{\max}$ for super-preshowers only serves to examine if there are any significant outliers that would be difficult to compensate.

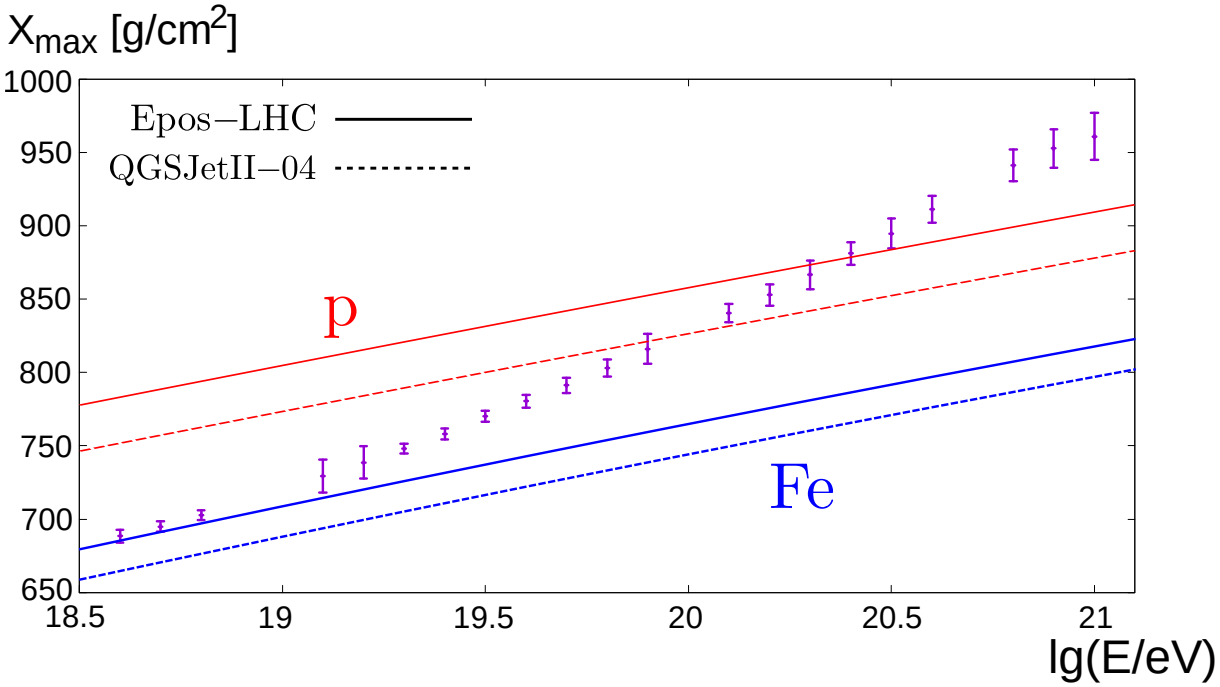

Figure 4.3: $X_{\max}$ as a function of the energy of the photon primary (100 showers per energy, each photon arriving from the strong B direction converting at an altitude of 27270 km a.s.l.); the red and blue lines indicate the proton and iron lines, respectively, from Aab et al. [2] (the lines are extrapolated to higher energies assuming the same slope; the solid line is EPOS-LHC simulation, dashed line is QGSJetII-04).

$X_{\max}$ increases steadily with the energy. Until about $10^{20-20.5}$ eV, the $X_{\max}$ values lie between the proton and iron lines, depending on which model prediction is used. Moreover, the energy of $10^{19.6}$ eV, chosen for the analysis of the altitude dependence of $X_{\max}$, lies within the range set by proton and iron. This energy was used for first test simulations as it is the largest energy used in the Auger $X_{\max}$ data (see figure 2.14), and most clearly represents the transition in the mass composition to heavier nuclei, which constitutes an important motivation for the analysis of super-preshowers. Whether super-preshowers do, in fact, develop deeper into the atmosphere than protons for energies above $10^{20-20.5}$ eV, as the plot suggests, is not clear because, as mentioned before, the interactions of secondary photons are not being considered in the current simulation. Similarly to the regular preshower effect, the elongation rate (defin-

ition in section 2.3.2) might be negative for higher photon energies, which could extend the range for which the X_{max} values lie between the proton and iron lines. Even if the candidate super-preshower processes do not merit such a scenario, it is worthy of further study at least for the sake of consistency. The inclusion of conversions of secondary photons is actualised by introducing an energy threshold to the *preshw.c* program above which all photons are forced into conversion. With this modification, I replotted the dependence of X_{max} on the primary energy for an energy threshold of $E_{\text{thresh}} = 10^{18}$ eV and $E_{\text{thresh}} = 10^{19}$ eV for 100 showers per energy bin (see figure 4.4); again, I added the proton and iron lines from model predictions.

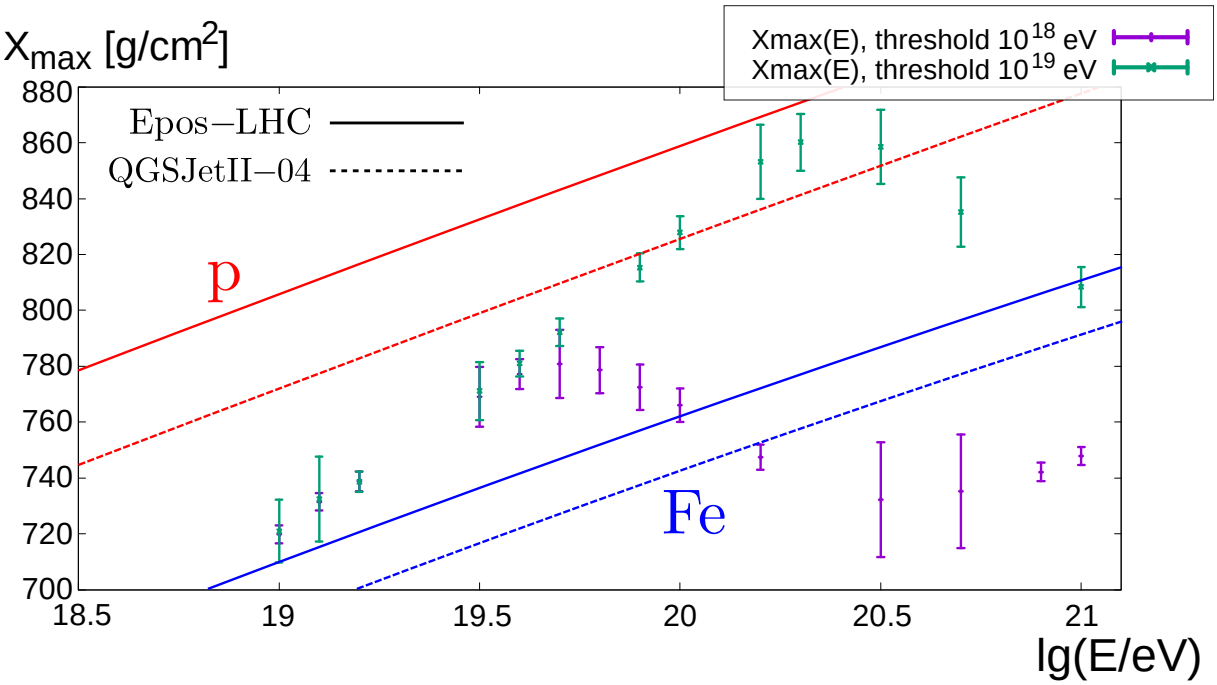

Figure 4.4: Depth of the shower maximum X_{max} as a function of energy of a photon primary with an energy threshold of $E_{\text{thresh}} = 10^{18}$ eV (purple points with errorbars), and of $E_{\text{thresh}} = 10^{19}$ eV (green points with errorbars), respectively, above which all (secondary) photons will be forced into conversion (100 showers per energy bin, each photon arriving from the strong B direction and converting at an altitude of 27270 km a.s.l.); the red and blue lines indicate the proton and iron lines, respectively, from Aab et al. [2] (the lines are extrapolated to higher energies assuming the same slope; solid line is EPOS-LHC simulation, dashed line is QGSJetII-04).

Indeed, the increase of X_{max} with the energy stops with the introduction of an energy threshold, where the maximum is at $10^{19.6}$ eV for $E_{\text{thresh}} = 10^{18}$ eV and $10^{20.5}$ eV for $E_{\text{thresh}} = 10^{19}$ eV. For $E_{\text{thresh}} = 10^{19}$ eV, we see a negative elongation rate and X_{max} eventually falls back into

the range set by the proton- and iron-induced showers for both model predictions. The trend for $E_{\text{thresh}} = 10^{18}$ eV also shows a negative elongation rate after the maximum and the X_{max} values quickly drop below the iron line; there also appears to be a minimum at $10^{20.5}$ eV, after which the X_{max} do not increase significantly, though. Although both trends yield X_{max} value outside the range set by the proton and iron lines, which is not necessarily problematic, as explained before, they also show that an introduction of secondary conversions can lead to a flatter, or even negative, elongation rate that can extend the range for which super-preshowers could play a role in the composition of the cosmic ray flux. The value of X_{max} for $E = 10^{19.6}$ eV is not affected by the introduction of the secondary conversions for all energies above $E_{\text{thresh}} = 10^{18}$ eV and $E_{\text{thresh}} = 10^{19}$ eV, respectively. We can, thus, continue using this energy for further comparison between photon initiated and hadronic showers.

As the values of observables are model-dependent, the exact numerical values for both proton- and iron-induced air-showers for the simulation with *Conex* using the QGSJet01 interaction model are of interest for reliably comparing hadronic showers and super-preshowers. They were determined via simulation of 500 showers at $10^{19.6}$ eV arriving from the strong B direction; the distribution of the X_{max} for the 500 showers was plotted in a histogram with which the mean and root mean square of X_{max} can be calculated (see in figures 4.5 and 4.6). In addition, to also obtain the numerical value of X_{max} with higher statistics for super-preshowers, I plotted the same histogram for the simulation of the same number of photon-induced showers at $10^{19.6}$ eV with the altitude varying according to a uniform distribution between 7922 km a.s.l. to 57055 km a.s.l. (corresponding to the starting altitude parameters from 10^4 to $6 \cdot 10^4$), also arriving from the strong B direction (see figure 4.7); this choice of parameters will be referred to as the *prototypical super-preshower* henceforth.

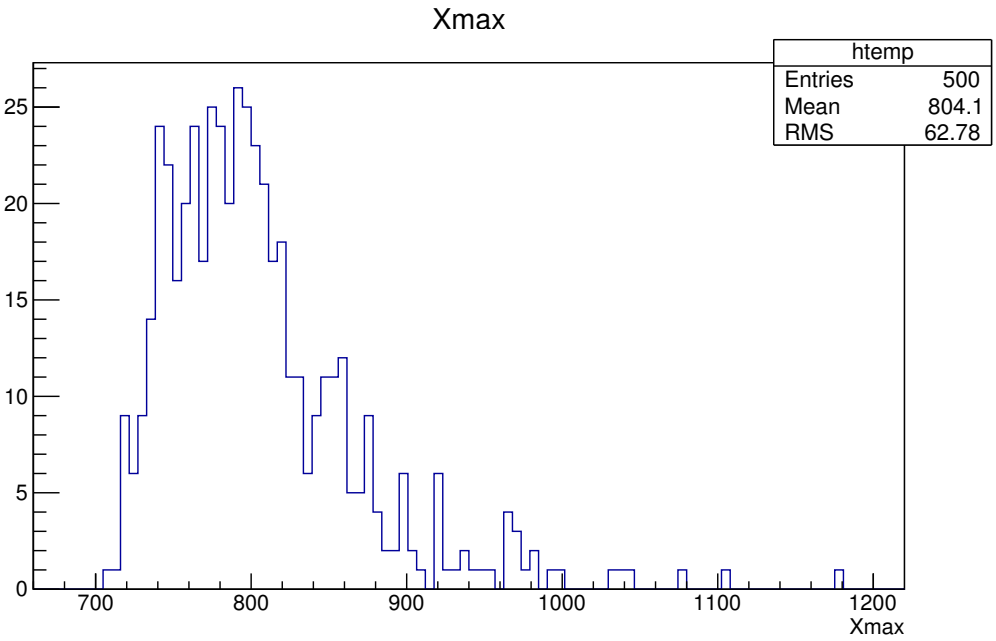

Figure 4.5: Depth of the shower maximum $X_{\max}$ for a proton-induced air-shower (500 showers, energy of $10^{19.6}$ eV, arriving from the strong B direction).

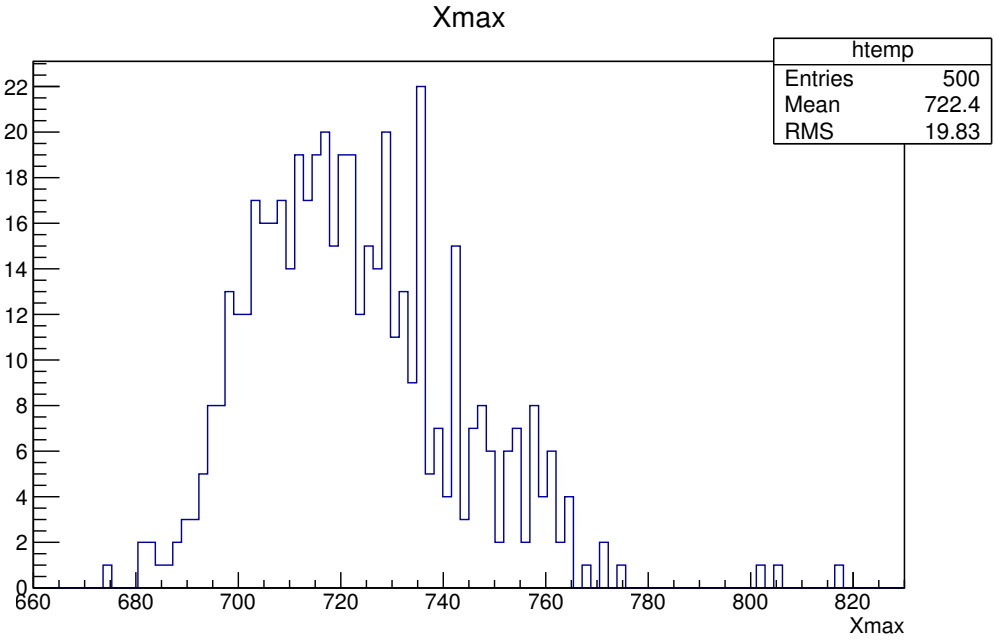

Figure 4.6: Depth of the shower maximum $X_{\max}$ for an iron-induced air-shower (500 showers, energy of $10^{19.6}$ eV, arriving from the strong B direction).

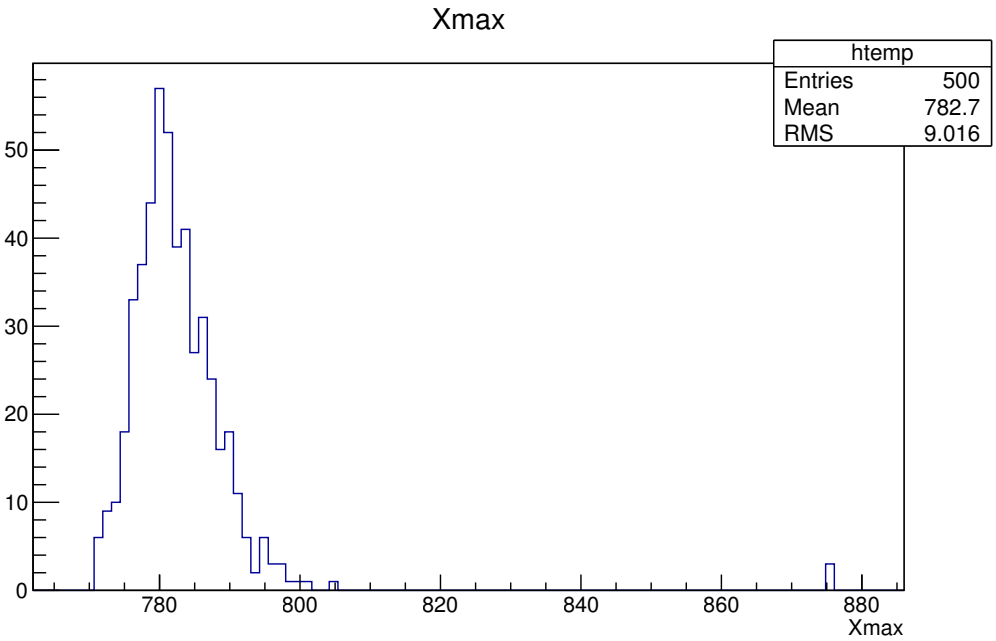

Figure 4.7: Depth of the shower maximum X_{max} for the prototypical super-preshower.

For the proton- and iron-induced showers, we have $X_{\text{max}} = 804.1 \pm 62.78$ and $X_{\text{max}} = 722.4 \pm 19.83$, respectively. For the prototypical super-preshower, $X_{\text{max}} = 782.7 \pm 9.0$ corresponds well with $X_{\text{max,lim}} = 780.4$ from figure 4.2 and lies within the values for the hadronic showers, confirming previous findings. A more interesting quantity in this comparison is the root mean square of X_{max}, $\sigma\left(X_{\text{max}}\right)$, which is comparably large for proton-induced showers ($\approx$ 8 % of mean value), whereas iron-induced showers scatter significantly less ($\approx$ 3 % of mean); the photon-induced shower is a lot more compact than hadronic showers (see 2.2) with an $\sigma\left(X_{\text{max}}\right) \approx 1$ %. To further illustrate this fact, I plotted the energy dependence of $\sigma\left(X_{\text{max}}\right)$ (see figure 4.8), where I included the iron lines for the EPOS-LHC and the QGSJetII-04 models from figure 2.14, as I did for figure 4.3 and 4.4.

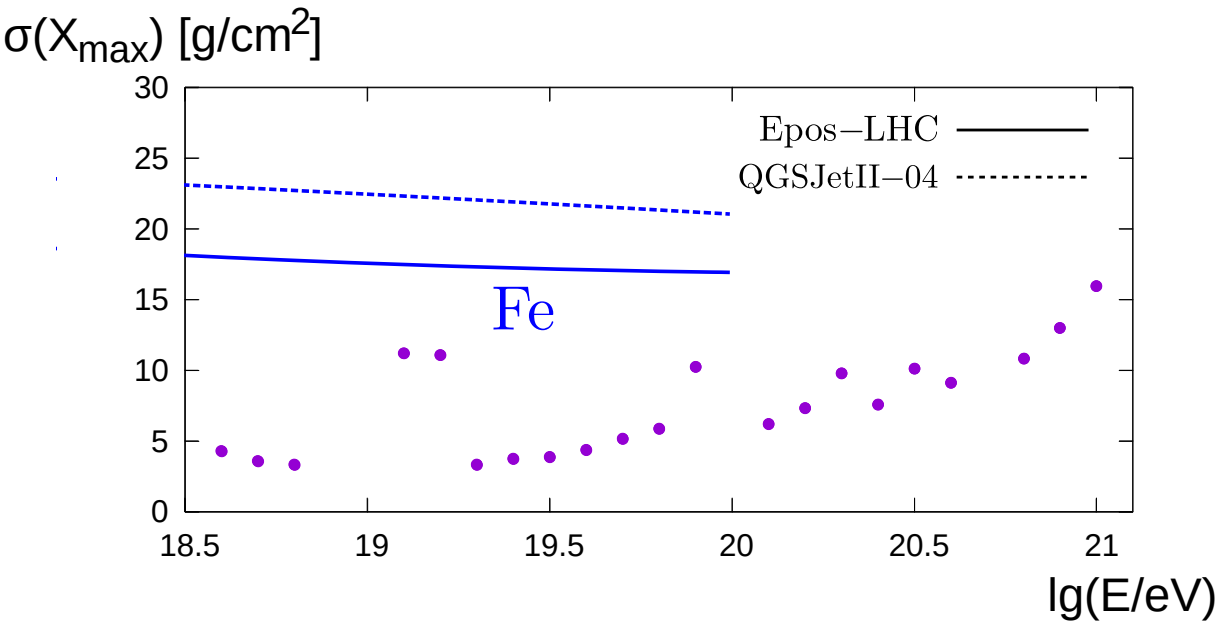

Figure 4.8: $\sigma\left(X_{\max}\right)$ as a function of the energy of the photon primary (100 showers per energy, each photon arriving from the strong B direction converting at an altitude of 27270 km a.s.l.); the blue line indicates the iron from Aab et al. [2] (there is no extrapolation to higher energies, as was done for figures 4.3 and 4.4; the solid line is EPOS-LHC simulation, dashed line is QGSJetII-04).

That photons have significantly lower $\sigma\left(X_{\max}\right)$ than hadronic showers could explain the fact that $\sigma\left(X_{\max}\right)$ suggests a heavier composition than $X_{\max}$ in Auger data (see figure 2.14 in section 2.3.2); a composition consisting of light nuclei and a significant fraction of photons (that initiate super-preshowers) is consistent with such a measurement.

Having found the altitude and energy range for which photon initiated showers that include super-preshowers are consistent with Auger data, we can compare the longitudinal profiles of the energy deposit among photon-induced and hadronic showers. For each profile, I simulated 100 showers, and set the primary energy to $10^{19.6}$ eV and the arrival direction to the strong B direction (see figure 4.9).

The deposited energy of hadronic and super-preshowers is sufficiently similar, in particular in terms of height and position of the maximum energy deposit (the latter of which is fulfilled by construction). The differences in shower-to-shower fluctuations between the three different types of primary particle alluded to in the discussion of the histograms (see figures 4.5 to 4.7) are also visible. In terms of energy deposit, we see that photon initiated air showers that have

undergone a super-preshower can mimic hadronic showers rather well.

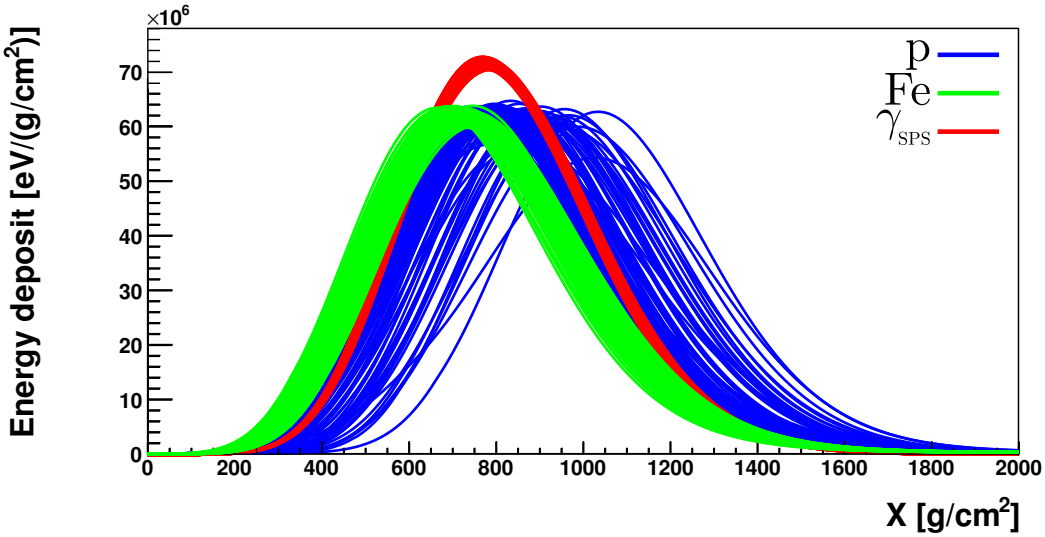

Figure 4.9: $\frac{dE}{dX}$ versus shower depth X for the prototypical super-preshower (red), and proton (blue), iron (green) initiated air-shower (100 showers each with primary energy of $10^{19.6}$ eV and arriving from the strong B direction).

4.1.3 Analysis of muon numbers

For the comparison of the number of muons N_μ, and the muon production rate dN_μ between photon initiated and hadronic showers, I will begin by analysing the longitudinal profiles as differences can be visualised best this way. As for the longitudinal profiles of the energy deposit, I simulated 100 showers of protons, iron and the prototypical super-preshower, and set the primary energy to $10^{19.6}$ eV and the arrival direction to the strong B direction (see figures 4.10 and 4.11).

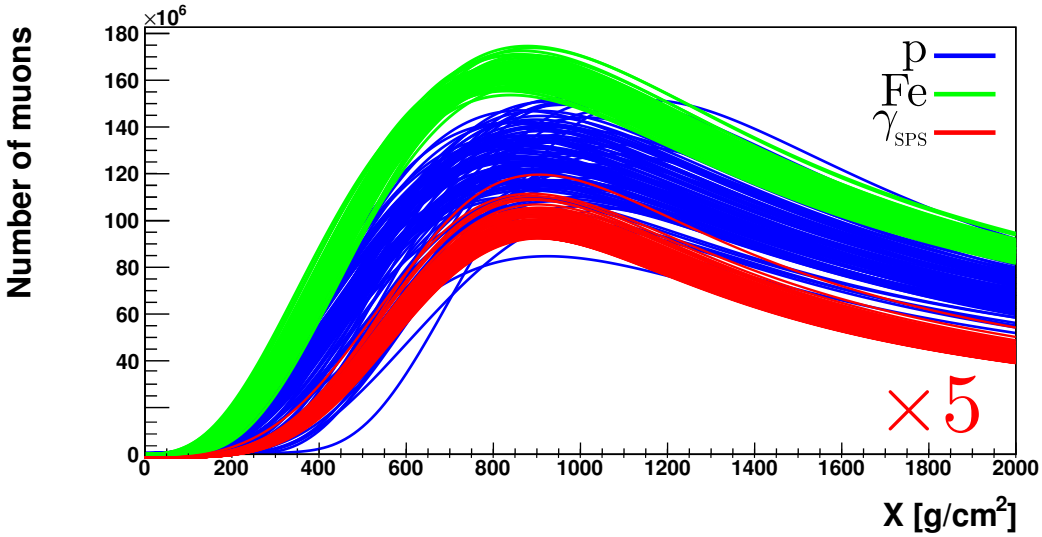

Figure 4.10: N_μ versus shower depth X for the prototypical super-preshower (red), and proton (blue), iron (green) initiated air-shower (100 showers each with primary energy of $10^{19.6}$ eV and arriving from the strong B direction); the longitudinal profile of the super-preshower is multiplied by a factor of 5 for purposes of visibility.

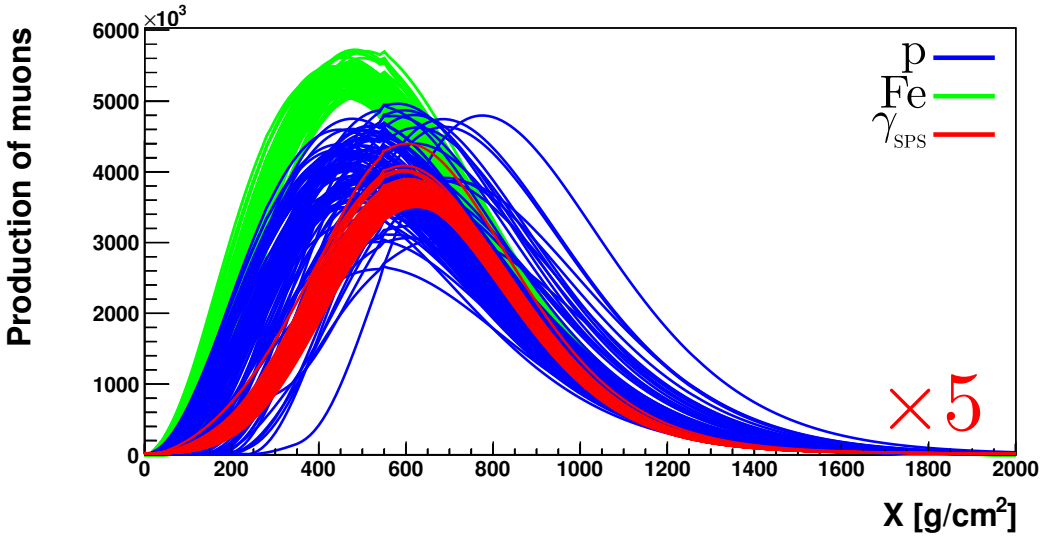

Figure 4.11: dN_μ versus shower depth X for the prototypical super-preshower (red), and proton (blue), iron (green) initiated air-shower (100 showers each with primary energy of $10^{19.6}$ eV and arriving from the strong B direction); the longitudinal profile of the super-preshower is multiplied by a factor of 5 for purposes of visibility.

The muon number and production rate, N_μ and dN_μ, are smaller by a factor of $6-8$ or $5-7$, respectively, for the prototypical super-preshower than for hadronic showers, which is consistent with the fact that photon-induced showers, generally, have a low muon content (see 2.2). As we observe a muon excess in the Auger data (see section 2.3.2), it is of interest to find the circumstances, under which photon-induced showers have higher muon numbers, in particular in the order of proton- and iron-induced showers ($\sim 10^8$ muons per atmospheric depth). I will only focus on N_μ for the following analysis as the muon production rate should increase by about the same amount. I will investigate the effects of three quantities on the muon number, namely the primary energy, the starting altitude and the number of particles initiated in the super-preshower before reaching the top of the atmosphere N_{part}.

Increasing the energy or the conversion starting altitude of the photon primary seems to be the most natural way to try achieving higher muon numbers as these are parameters that we previously manipulated; this would imply, though, that energies of super-preshowers are generally underestimated in reconstruction. I simulated 100 prototypical super-preshowers for the energies $10^{19.6}$ eV, 10^{20} eV, $10^{20.3}$ eV, and $10^{20.6}$ eV and plotted N_μ at X_{max} versus the starting conversion altitude for each of these energies (see figure 4.12).

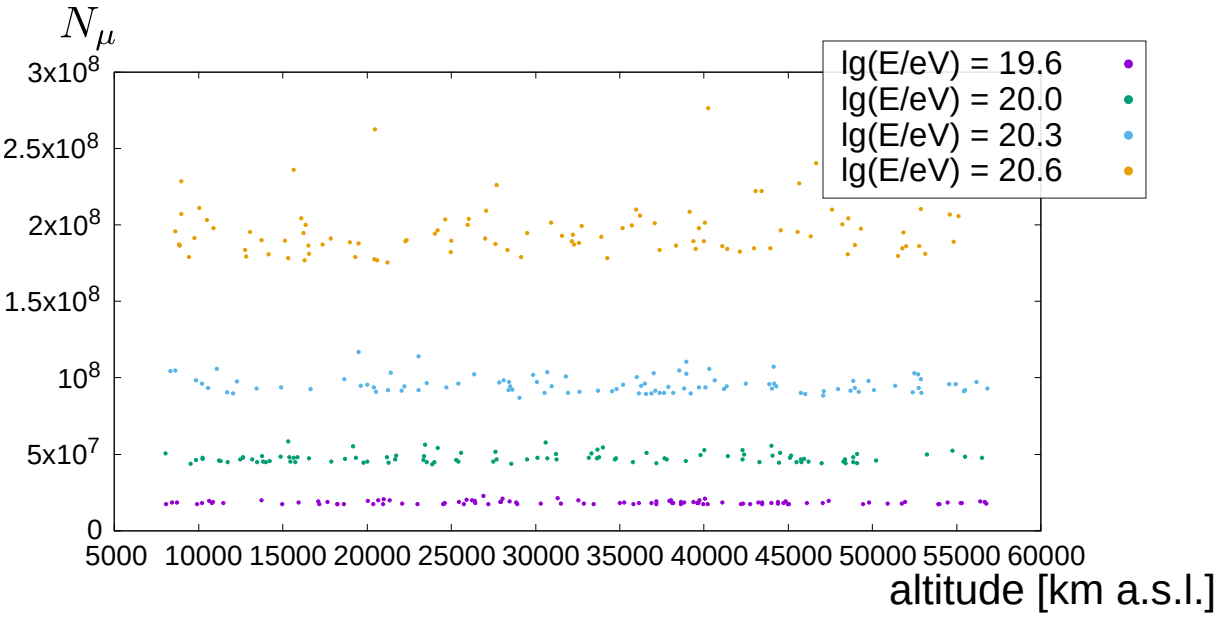

Figure 4.12: N_μ at X_{max} versus altitude for different photon primary energies (given in the legend; arrival direction is the strong B direction).

First, we see that the muon number does not depend on the altitude of the first conversion. It does increase with the energy, though, but the necessary increase in N_μ requires an energy increase of about one order of magnitude, for which X_{max} would fall outside the region set by proton and iron if no secondary conversions are taken into account (see figure 4.3, as well as 4.5 and 4.6); however, with the inclusion of secondary conversions for energies above $E_{\text{thresh}} = 10^{18}$ eV, this would not be a problem, nor for $E_{\text{thresh}} = 10^{19}$ eV, depending on the interaction model.

The potential dependence of the number of muons on the number of particles initiated by the super-preshower above the top of the atmosphere N_{part} requires some explanation. Generally, we see from the longitudinal profiles of the muon number and muon production rate for the prototypical super-preshower (see figures 4.10 and 4.11) that photon-induced air showers with super-preshowering contain a substantially larger number of muons compared to regular photon initiated showers (which is only about 1 %; see section 2.2 and [26], in particular). We also saw in chapter 2 that super-preshowers contain significantly more particles before entering into the atmosphere than regular preshowers (1500 particles (see section 2.4) versus 500 particles (see section 2.2.1)). Therefore, it stands to reason that the number of particles produced in the (super-)preshower could affect the number of muons created in the air shower N_μ.

As further rationale, I draw attention to figure 4.13 [48] where the total number of muons at ground level divided by the primary energy N_μ/E is plotted as a function of E for proton and iron initiated showers. The ratio N_μ/E disentangles the obvious increase of muon numbers with the primary energy and, plotted against the primary energy, it can be used as a measure to show any variation in muon production with the energy; the plot shows a decrease of the interaction cross sections leading to muon production with primary energy for hadronic showers.

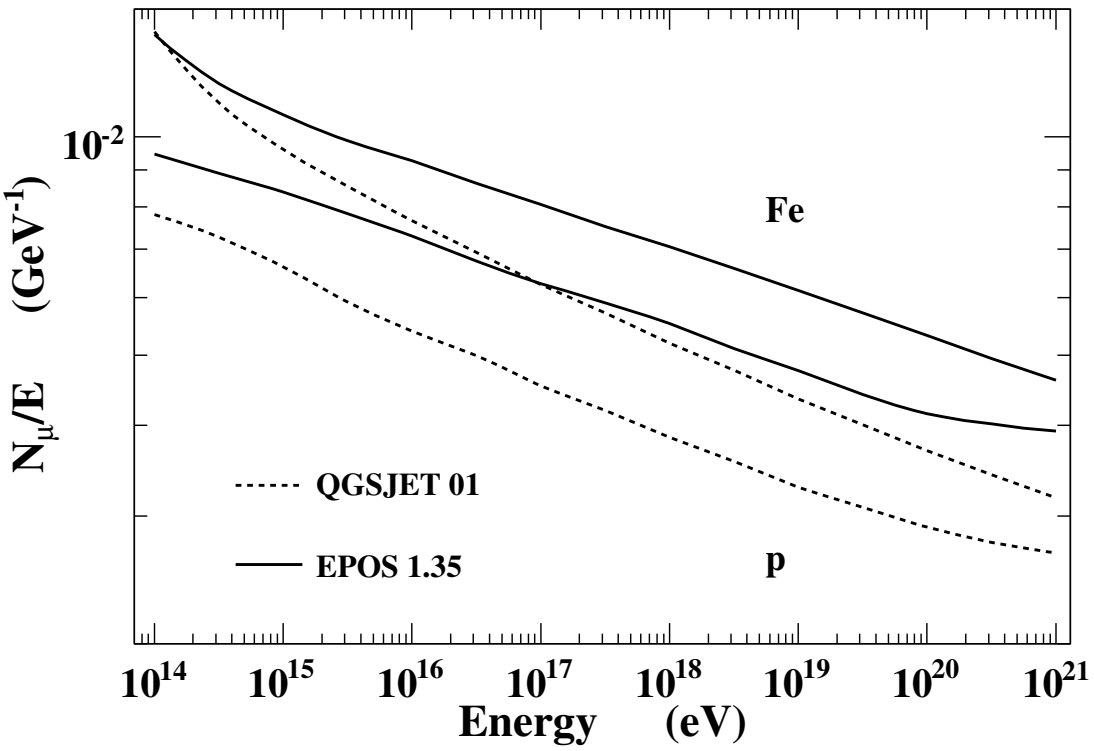

Figure 4.13: Total number of muons at ground level divided by the primary energy N_μ/E as a function of E for hadronic showers for energies E from 10^{14} eV to 10^{21} eV [48].

It is possible that a similar effect arises for photon initiated showers that undergo super-preshowering because they had split into a multitude of particles before reaching the top of the atmosphere with lower energies per particle than the primary photon and with a comparably wide energy range, including many significantly less energetic photons. If there is a similar trend in muon production with primary energy as for hadronic showers, we should expect the number of muons to increase with the number of particles created in the (super-)preshower. In fact, for super-preshowers to mimic hadronic showers, a similar trend is expected. I investigated this by plotting the number of muons at X_{max} (the trend should also be visible at this depth) as a function of the primary energy from $E = 10^{12}$ eV to $E = 10^{19}$ eV; to ensure that the plot corresponds to figure 4.13, I included proton and iron initiated showers as well (see figure 4.14).

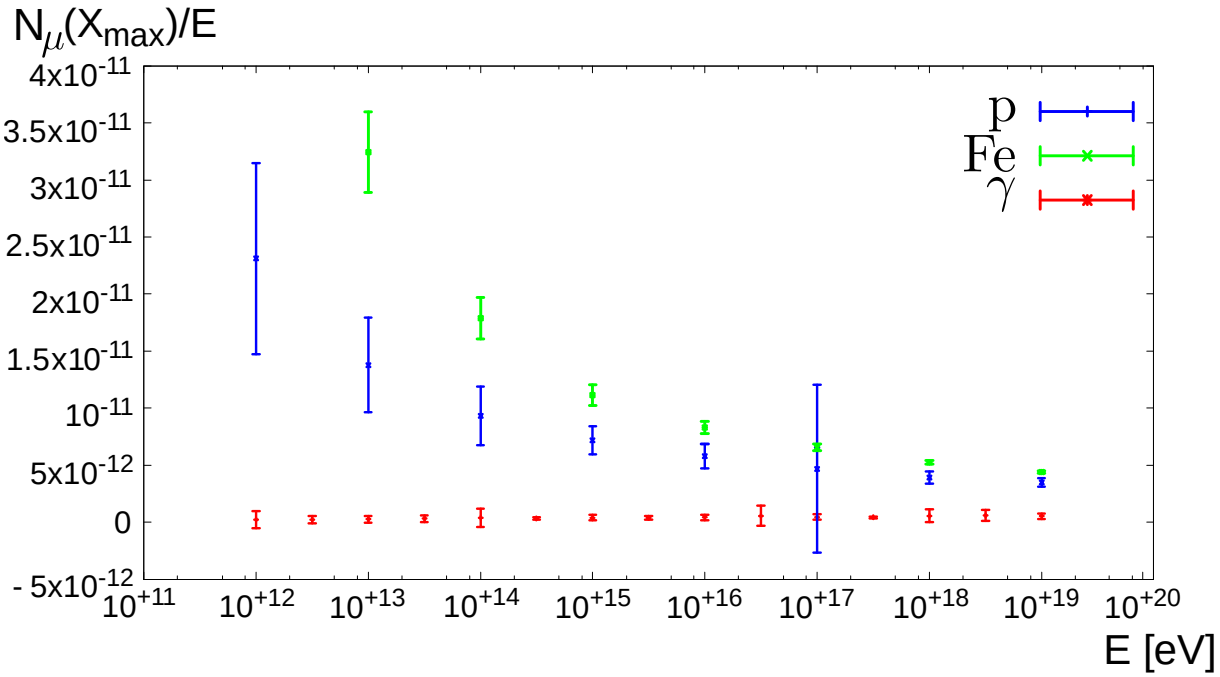

Figure 4.14: Number of muons at $X_{\max}$ divided by the primary energy N_μ/E as a function of E from $E = 10^{12}$ eV to $E = 10^{19}$ eV for super-preshowers, as well as for hadronic showers (hadronic showers are included to verify figure 4.13; for every shower, the arrival direction is the strong B direction).

The trend of the hadronic showers is consistent with that of figure 4.13, showing a decrease of N_μ/E with the energy. For super-preshowers, however, the trend appears to be constant suggesting that there is no dependence of N_μ on N_{part}. It is possible that the primary photons in the investigated energy range (i.e. without pre-showering) do not produce a sufficient amount of low-energy secondary photons to bring out a potential effect on the muon production at low energies. To test the possibility, I constructed a scatter plot of N_{mu} at $X_{\max}$ of the photon initiated shower for the parameters of the prototypical super-preshower versus the number of particles at the top of the atmosphere (see figure 4.15).

There seems to be no discernible dependence of N_μ on N_{part}, confirming the results from figure 4.14. On the one hand, this means that a larger number of particles at the top of the atmosphere does not increase the number of muons, and, on the other hand, it suggests that photon initiated showers that have undergone super-preshowers are not consistent with hadronic ones in terms of the quantity N_μ/E. This result should re-analysed with more sophisticated simulations using *Corsika*. Generally, the effects of altering the photonuclear cross section on the

muon production must be taken into account.

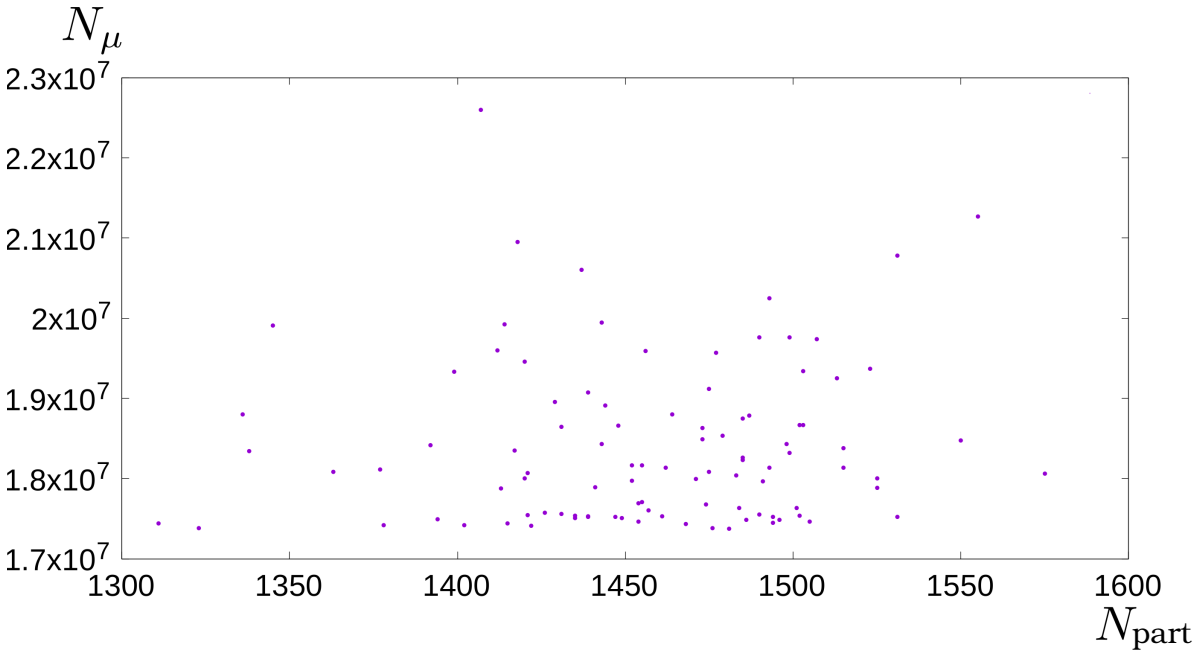

Figure 4.15: Scatter plot of N_μ versus N_{part} for the prototypical super-preshower.

All in all, the simulation results give no reason to dismiss super-preshowers; in fact, the good agreement in terms of energy deposit shows the potential explanatory power of super-preshowers. However, it is worth reiterating that they can only be considered if a candidate mechanism is found which produces such showers.

Chapter 5

Conclusion

This thesis sought to explore an alternative cosmic ray composition scenario with a significant fraction of photons that initiate *super-preshowers* before entering into Earth's atmosphere. Possible super-preshowers processes, i.e. photon splitting and pair production via solar photons, were examined, and specifically the effects of super-preshowers initiated near Earth on observables important for mass composition studies, namely the depth of maximal energy deposit X_{max} and muon production, were investigated.

No candidate process for super-preshowers can clearly be identified in this thesis. Pair production with solar photons was shown to be too rare to significantly contribute with a probability of occuring after a traversed distance of 1 AU along the path from the Sun the Earth of $\lesssim 10^{-8}$. The analysis of photon splitting gave no definite results as the probability of this process for Auger conditions could not be calculated due to a lack of convergence with available literature; several aspects of the calculation could be established, however, such as the integrability of the expressions and the correct choice of units. In addition, due to the discrepancy between the calculations and the literature, it is not certain whether the low-frequency non-dispersive limit can be applied for energies in the vicinity of UHECRs despite the fulfilment of the corresponding inequalities.

Simulations show that photon initiated air showers undergoing super-preshowers can mimic hadronic showers in terms of X_{max} and the longitudinal profile of the energy deposit, and that the apparent transition from light to intermediate mass nuclei in the cosmic ray composition

could be explained with a significant fraction of photons, confirming previous results from Homola [31]. With respect to muon production, super-preshowers show distinct differences from hadronic showers: On the one hand, super-preshowers produce less muons than proton- or iron-induced showers, on the other hand, the production of muons of photon initiated showers does not show a similar energy dependence as hadronic showers (as shown in [48]); I demonstrated that the former fact can be compensated by an energy increase of the primary photon, which would imply a miscalibration of super-preshowers.

As pioneering work on the topic of super-preshowers, this thesis does by no means provide an exhaustive discussion of this phenomenon. I hope to have shown, however, its significance for mass composition studies, and to have motivated further investigations within this topic. Future research should include the search for candidate mechanisms that could initiate a super-preshower. For photon splitting, properly calculating the probability for Auger conditions is essential for assessing its viability; this entails identifying the source of the lack of convergence with literature. Interactions with the radiation belts are of special interest as a candidate mechanism as these are situated at altitudes in the order of 10000 km [19], which appears to be the minimal altitude for producing X_{max} values consistent with hadronic showers. If a convincing example of a super-preshower mechanism is found, then all current photon limits have to be revised as none of them has so far taken super-preshowers into account. This would be the case, even if the photon fraction at ultra-high energies was not significant.

In addition, it is important to search for characteristic properties of the candidate mechanisms, which can and should be used as fingerprints in data analysis. Further simulations with other programs, such as *Corsika*, and the use of different hadronic interaction models should be employed to cross-check the results from this thesis. Other steps, in particular in terms of increasing the number of muons, e.g. altering the photonuclear cross-section, are natural next steps. Moreover, further observables, such as the rise time profile of super-preshowers in comparison with hadronic showers, should be investigated to gain a better understanding of super-preshowers in general, and to find potential fingerprints to distinguish them from hadronic showers. As super-preshowers are indicatory of exotic production models, it is important to compare predictions from such models with data, once a good understanding of super-preshowers has been developed. Finally, it is worth noting that, if super-preshowers cannot be distinguished from hadronic showers for the available observables at the PAO, and if new observables can be found that do allow a discrimination between the two, requirements

on the future upgrades of the experiment can be set.

Bibliography

[1] Aab, A. et al., *A Search for Point Sources of EeV Photons*, The Astrophysical Journal **789**, 160 (2014).

[2] Aab, A. et al., *Depth of maximum of air-shower profiles at the Pierre Auger Observatory. I. Measurements at energies above* $10^{17.8}$ eV, Phys. Rev. D **90**, 122005 (2014).

[3] Aab, A. et al., *Depth of maximum of air-shower profiles at the Pierre Auger Observatory. II. Composition implications*, Phys. Rev. D **90**, 122006 (2014).

[4] Aab, A. et al., *Muons in air showers at the Pierre Auger Observatory: Mean number in highly inclined events*, Phys. Rev. D **91**, 032003 (2015).

[5] Aab, A. et al., *Muons in air showers at the Pierre Auger Observatory: Measurement of atmospheric production depth*, Phys. Rev. D **90**, 012012 (2014).

[6] Abbasi, R. et al., *Report of the Working Group on the Composition of Ultra High Energy Cosmic Rays*, in 2014 Conference on Ultrahigh Energy Cosmic Rays (UHECR2014) Springdale, USA, October 12-15, 2014 (2015).

[7] Abbasi, R. et al., *Study of Ultra-High Energy Cosmic Ray composition using Telescope Array's Middle Drum detector and surface array in hybrid mode*, Astroparticle Physics **64**, 49–62 (2015).

[8] Abreu, P. et al., *Antennas for the Detection of Radio Emission Pulses from Cosmic-Ray*, JINST **7**, P10011 (2012).

[9] Abreu, P., Aglietta, M. et al., *Interpretation of the Depths of Maximum of Extensive Air Showers Measured by the Pierre Auger Observatory*, JCAP **1302**, 026 (2013).

[10] Abu-Zayyad, T. et al., *The energy spectrum of ultra-high-energy cosmic rays measured by the Telescope Array FADC fluorescence detectors in monocular mode*, Astroparticle Physics **48**, 16–24 (2013).

[11] Ahn, E.-J. et al., *Cosmic ray interaction event generator SIBYLL 2.1*, Phys. Rev. D **80**, 094003 (2009).

[12] Bahcall, J. N. and Waxman, E., *Has the GZK cutoff been discovered?*, Phys. Lett. **B556**, 1–6 (2003).

[13] Beresteckii, V. B. et al., *Quantum Electrodynamics*, 2nd ed., Vol. 4 (Elsevier Ltd., Oxford, 1982).

[14] Berezinsky, V. et al., *Ultrahigh Energy Cosmic Rays without Greisen-Zatsepin-Kuzmin Cutoff*, Phys. Rev. Lett. **79**, 4302–4305 (1997).

[15] Bergmann, T. et al., *One-dimensional hybrid approach to extensive air shower simulation*, Astroparticle Physics **26**, 420–432 (2007).

[16] *The Pierre Auger Observatory: Contributions to the 34th International Cosmic Ray Conference (ICRC 2015), contribution 3.4* (2015).

[17] Blümer, J. et al., *Cosmic rays from the knee to the highest energies*, Progress in Particle and Nuclear Physics **63**, 293–338 (2009).

[18] Bueno, A. et al., *Risetime Studies using MonteCarlo Simulations*, GAP note: GAP-2014-119, Dec. 2014.

[19] Butler, L., *The Van Allen Probes — Exploring Earth's Radiation Belts and the Extremes of Space Weather*, `http://www.space.com/6221-cloak-plasma-earth.html`.

[20] Chappell, C. R. et al., *Observations of the warm plasma cloak and an explanation of its formation in the magnetosphere*, Journal of Geophysical Research: Space Physics **113**, A09206 (2008) `10.1029/2007JA012945`.

[21] Deligny, O. et al., *An Empirical Estimate of the Shift Between the Auger and Telescope Array Energy Scales*, GAP note: GAP 2015-091, Nov. 2015.

[22] Ellis, J. et al., *Ultrahigh-energy cosmic rays particle spectra from crypton decays*, Phys. Rev. D **74**, 115003 (2006).

[23] Géhéniau, J., *Les Fonctions Singulières De L'équation De Klein-gordon [sic], Tenant Compte D'un Champ Magnétique Extérieur*, Physica **16**, 822–830 (1950).

[24] Géhéniau, J. and Demeur, M., *Solutions singulières des équations de dirac [sic], tenant compte d'un champ magnétique extérieur*, Physica **17**, 71–75 (1951).

[25] Greiner, W. and Reinhardt, J., *Quantum Electrodynamics*, 4th ed., Vol. 1 (Springer, Berlin Heidelberg, 2010).

[26] Grieder, P. K., *Extensive Air Showers*, 2nd ed. (Springer, Berlin Heidelberg, 2009).

[27] Grupen, C., *Astroparticle Physics*, 1st ed. (Springer, Berlin Heidelberg, 2005).

[28] Harding, A. K. et al., *Photon-Splitting Cascades in Gamma-Ray Pulsars and the Spectrum of PSR 1509-58*, The Astrophysical Journal **476**, 246–260 (1997).

[29] Heck, D. et al., *CORSIKA: a Monte Carlo code to simulate extensive air showers.* (Feb. 1998).

[30] Hill, C. T., *Monopolonium*, Nuclear Physics B **224**, 469–490 (1983).

[31] Homola, P., *Super preshowers — can photons induce iron-like showers?*, Presentation for the Auger Collaboration Meeting, Nov. 2015.

[32] Homola, P. and Risse, M., *Method to Calibrate the Absolute Energy Scale of Air Showers with Ultrahigh Energy Photons*, Phys. Rev. Lett. **112**, 151104 (2014).

[33] Homola, P. et al., *Simulation of ultra-high energy photon propagation in the geomagnetic field*, Computer Physics Communications **173**, 71–90 (2005).

[34] Homola, P. et al., *Simulation of ultra-high energy photon propagation with PRESHOWER 2.0*, Computer Physics Communications **184**, 1468–1475 (2013).

[35] Homola, P. et al., *Simulation of ultra-high energy photon showers with PRESHOWER*, Nuclear Physics B - Proceedings Supplements **151**, Proceedings of the XIII International Symposium on Very High Energy Cosmic Ray Interactions, 119–120 (2006).

[36] Institute for Cosmic Ray Research, University of Tokyo, JAPAN, *High Resolution Fly's Eye (HiRes) - Physics @ the U*, (2009) `http://www.cosmic-ray.org/`.

[37] Instituto de Tecnologías en Detección y Astropartículas (ITeDA), *Pierre Auger Observatory*, `http://www.iteda.cnea.gov.ar/en/?q=node/14`.

[38] Kalmykov, N. et al., *Quark-gluon-string model and EAS simulation problems at ultra-high energies*, Nuclear Physics B - Proceedings Supplements **52**, 17–28 (1997).

[39] Kampert, K.-H., *Cosmic Rays from the Knee to the Ankle – Status and Prospects*, Nuclear Physics B - Proceedings Supplements **165**, Proceedings of the Cosmic Ray International Seminars, 294–306 (2007).

[40] Kampert, K.-H. and Unger, M., *Measurements of the cosmic ray composition with air shower experiments*, Astroparticle Physics **35**, 660–678 (2012).

[41] Melrose, D. B., *A relativistic quantum theory for processes in collisionless plasmas*, Plasma Physics **16**, 845 (1974).

[42] Molina Bueno, L. and Pierre Auger Collaboration, *Mass composition measurements at the Pierre Auger Observatory*, Astronomische Nachrichten **336**, 785–789 (2015).

[43] Novotny, V. et al., *Accuracy of shower parameters in stereo reconstruction — Summary of Master thesis*, GAP note: GAP-2013-110, Dec. 2013.

[44] Ostapchenko, S., *On the model-dependence of the relation between minimum-bias and inelastic proton–proton cross sections*, Physics Letters B **703**, 588–592 (2011).

[45] Peters, B., *Primary cosmic radiation and extensive air showers*, Il Nuovo Cimento (1955-1965) **22**, 800–819 (2009).

[46] phys.org, *A century of discoveries - Physicists celebrate centenary of the discovery of cosmic rays*, `http://phys.org/news/2012-07-century-discoveries-physicists-celebrate.html`.

[47] Pierog, T. et al., *First Results of Fast One-dimensional Hybrid Simulation of EAS Using CONEX*, Nucl. Phys. Proc. Suppl. **151**, 159–162 (2006).

[48] Pierog, T. and Werner, K., *Muon Production in Extended Air Shower Simulations*, Phys. Rev. Lett. **101**, 171101 (2008).

[49] Porcelli, A., *Measurement of the Depth of Shower Maximum in the Transition Region between Galactic and Extragalactic Cosmic Rays with the Pierre Auger Observatory*, PhD thesis (KIT, Karlsruhe, 2014).

[50] Press, W. H. et al., *Numerical Recipes: The Art of Scientific Computing*, 3rd ed. (Cambridge University Press, New York, NY, USA, 2007).

[51] Risse, M. and Homola, P., *Prospects of searches for ultra-high energy photons*, in Proceedings, 30th International Cosmic Ray Conference (ICRC 2007), Vol. 4 (2007), pp. 499–502.

[52] Risse, M. and Homola, P., *Search for ultra-high energy photons using air showers*, Modern Physics Letters A **22**, 749–766 (2007).

[53] Risse, M. et al., *Photon air showers at ultra-high energy and the photonuclear cross-section*, Czechoslovak Journal of Physics **56**, A327–A336.

[54] Rybicki, G. B. and Lightman, A. P., *Radiative Processes in Astrophysics* (Wiley-VCH Verlag GmbH, 2007), pp. 1–50.

[55] Schauer, M., *Analysis of the discrepancies observed in the stereo and hybrid data in the Pierre Auger Observatory*, MA thesis (Bergische Universität Wuppertal, 2015).

[56] Schmidt, F., *CORSIKA – an Air Shower Simulation Program*, `https://www.ikp.kit.edu/corsika/`.

[57] Smith, B. et al., *The risetime as an indicator of the mass composition of UHECRs*, GAP note: GAP-2007-110, Sept. 2007.

[58] Stoneham, R. J., *Phonon [sic] splitting in the magnetised vacuum*, Journal of Physics A: Mathematical and General **12**, 2187 (1979).

[59] Tavernier, S., *Experimental Techniques in Nuclear and Particle Physics*, 1st ed. (Springer, Berlin Heidelberg, 2010).

[60] *The GNU MPFR Library*, `http://www.mpfr.org/`.

[61] The Pierre Auger Collaboration, *Pierre Auger Observatory*, `https://www.auger.org/`.

[62] The Pierre Auger Collaboration, *The Pierre Auger Cosmic Ray Observatory*, Nuclear Instruments and Methods in Physics Research Section A: Accelerators, Spectrometers, Detectors and Associated Equipment **798**, 172–213 (2015).

[63] University of Utah, *AGASA (Akeno Giant Air Shower Array)*, `http://www-akeno.icrr.u-tokyo.ac.jp/`AGASA`/`.

[64] Weiler, T., *Resonant absorption of cosmic-ray neutrinos by the relic-neutrino background*, Phys. Rev. Lett. **49**, 234–237 (1982).

[65] *Yakutsk EAS Array*, (2016) `http://eas.ysn.ru/`.

Erklärung

Ich versiche hiermit, dass ich meine Masterarbeit mit dem Titel *Analysis of Super-Preshowers at the Pierre Auger Observatory* selbständig und ohne Benutzung anderer als der angegebenen Hilfsmittel angefertigt habe und dass ich alle Stellen, die ich wörtlich oder sinngemäß aus Veröffentlichungen entnommen habe, als solche kenntlich gemacht habe. Die Arbeit hat bisher in gleicher oder ähnlicher Form oder auszugsweise noch keiner Prüfungsbehörde vorgelegen.

Ich versichere, dass die eingereichte schriftliche Fassung der auf dem beigefügten Medium gespeicherten Fassung entspricht.

Wuppertal, den 26.02.2016

(Alex Kääpä)